Summer 8-21-2020

Understanding the Magnetic Properties of II-VI Semiconductor Nanocrystals

Alex Khammang
University of Maine, alex.khammang@maine.edu

UNDERSTANDING THE MAGNETIC PROPERTIES OF II-VI SEMICONDUCTOR NANOCRYSTALS

By

Alex Khammang

M.S., Virginia Commonwealth University, 2014

B.S., Virginia Commonwealth University 2012

A DISSERTATION

Submitted in Partial Fulfillment of the

Requirements for the Degree of

Doctor of Philosophy

(in Physics)

The Graduate School

The University of Maine

August 2020

Advisory Committee:

Dr. Robert W. Meulenberg, Associate Professor of Physics, Advisor

Dr. Robert J. Lad, Professor of Physics

Dr. James P. McClymer, Associate Professor of Physics

Dr. Carl P. Tripp, Professor of Chemistry

Dr. Liping Yu, Assistant Professor of Physics

UNDERSTANDING THE MAGNETIC PROPERTIES OF II-VI SEMICONDUCTOR NANOCRYSTALS

By Alex Khammang

Dissertation Advisor: Dr. Robert W. Meulenberg

An Abstract of the Dissertation Presented
in Partial Fulfillment of the Requirements for the
Degree of Doctor of Philosophy
(in Physics)
August 2020

Semiconductor nanocrystals (NC) are well known for their unique size tunable optical properties making them suitable candidates for devices such as light emitting diodes (LEDs), solar cells, and cellular labels. II-VI semiconductors in the bulk form behave diamagnetically, but can inherit paramagnetic (PM) or ferromagnetic (FM) properties at the nanoscale. Reports suggest that the emergence of weak PM or FM behavior in undoped NCs are attributed to the increased surface to volume ratio compared for NCs. Traditionally, these NCs only obtain magnetic properties after doping with certain transition metals, such as Co, Mn, or Fe. Many mechanisms have been proposed to determine the source of magnetism in undoped NCs, ranging from dangling bonds, surface vacancies, and ligand exchange interactions. This thesis focuses on the role of dangling bonds and atomic vacancies on the surface of colloidal CdSe and ZnO NCs via controlled ligand removal along with CdS and CdS/ZnS core/shell nanoplatelets doped with Mn. Through magnetic measurements we show that for CdSe and ZnO NCs, the surface ligand density can drastically affect the magnetization results through a liquid phase post processing technique. For CdSe NCs the exact source of magnetism is complex and can arise from the uncoordinated surface atoms as seen with varying total angular momentum, J, values. In general, modification of magnetism in ZnO NCs can be attributed to the

formation of oxygen vacancies as seen from consistent J values. Lastly, CdS and CdS/ZnS NPLs inherently possess surface defects, such as Cd or Zn vacancies, which coupled with Mn dopants can promote strong spin coupling between the core and NC surface.

PREFACE

This thesis began by studying the emergence of weakly magnetic CdSe nanocrytals, which have been traditionally studied for their optical properties. It is my hope to better understand why these nominally nonmagnetic materials exhibit magnetism beyond the catchall phrase of "surface defects". The hope is that the physics presented in this thesis can be applied to other systems to enhanced those magnetic properties and to develop multiplication nanoparticle systems that can exhibit both native magnetic and optical properties. The experiments presented in this work proved difficult to attain and the results were perplexing as with most thesis. In the end, however, experiments don't lie, but our interpretation of the results may change.

"In the mist of chaos there is also opportunity"

-Sun Tzu, *The Art of War*

DEDICATION

To my wife, my family, my friends, and all who have supported me through my academic studies. I could not have made it through any of it without your continued support.

ACKNOWLEDGEMENTS

These past few years have had multiple, unexpected hurdles, but through it all my family and friends have supported me through it all. I like to especially thank my lovely wife, Megan Khammang, because without her I would not have made it through this program remotely sane. She encouraged me to strive for my best, even when I'm at my worst. Special thanks go to my advisor Dr. Robert Meulenberg, because he never gave up on me and provided this unique opportunity in scientific research. I want to also thank the National Science Foundation, funding source: DMR-1708617, for funds towards performing the work presented in this thesis. Lastly, I want to thank the Frontier Institute for Research in Sensors and Technology, the department of Physics at the University of Maine, and my committee members Dr. Lad, Dr. Tripp, Dr. McClymer, and Dr. Yu guiding me through my scientific endeavors.

TABLE OF CONTENTS

LIST OF TABLES

LIST OF FIGURES

CHAPTER 1

INTRODUCTION

1.1 Introduction

For the last two decades, the optical and magnetic properties of semiconducting nanocrystals (NCs) have been investigated for potential applications in spintronics, optoelectronics, and biomedicine [1–3]. Semiconductor NCs, such as cadmium selenide (CdSe) and zinc oxide (ZnO), are ideal candidates for optoelectronic and biomedical applications due to their size tunable optical properties at the nanoscale [1–5]. As the semiconducting NCs shrink to a size comparable to the excitonic Bohr radius, a blue shift in the optical absorption and photoluminescence (PL) is observed. For this reason, NCs also referred to as quantum dots (QDs) can exhibit optical tunability throughout the visible spectrum (Figure 1.1). Much of the recent research on NCs have been devoted towards the optimization of the PL quantum yields and lifetimes via a wide range of strategies including controlling size, shape, and surface chemistry [6–11]. Thus, the use of these optical NCs in biomedical applications are highly desirable since they are small enough to attach to biological components such as cells (10-100 μm), viruses (20-450 nm), and even protein molecules (5-50 nm) [12] while possessing inherent optical properties.

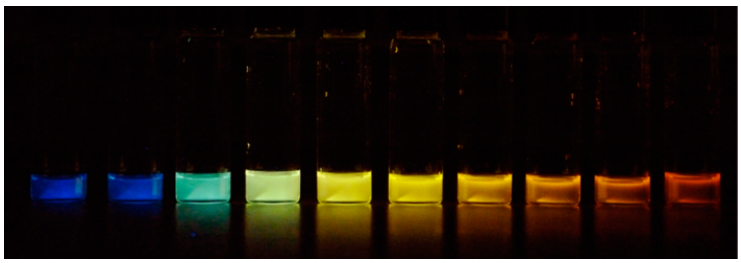

Figure 1.1: CdSe NCs grown to various sizes (1.6 - 2.3 nm) illumined using UV-light showing showing varying emission. The largest of NCs begin on the right and decreases in size to the left, showing a blueshift in optical emission. The size tunablity allows for CdSe NCs spans the visible spectrum[13].

When the study of the size dependent optical properties became well understood, researchers turned their efforts towards fabrication of new magnetic NCs. These pure or undoped semiconductor materials are considered diamagnetic in the bulk form [14], but interestingly, at the nanoscale, it has been shown that both CdSe and ZnO exhibit magnetic responses in the presence of an applied field [7]. As the NCs shrinks in size, the surface area to volume ratio (or aspect ratio) increases, suggesting the magnetic mechanism related the surface of these nanomaterials. Traditionally, magnetism of these materials occurs via the introduction of magnetic impurities or dopants like Co, Ni, Fe, or Mn [4, 15–20]. For instance, it has been shown that both CdSe and ZnO nanomaterials become paramagnetic or ferromagnetic after doping [15–19]. The emergence of magnetic properties, that arise from chemical doping, allow for the potential applications in biomedicine such as drug delivery, magnetic resonance imaging (MRI) contrast, and hyperthermia treatments [21]. Understanding how and why nanoscopic variants of these semiconductors exhibit drastically different and unexpected physical behavior is extremely important to further develop these types of materials. In this thesis I discuss why undoped semiconducting materials become magnetic at the nanoscale without the use of dopants. I hypothesize that by controlling the surface composition of these NCs, we can alter the weakly paramagnetic or ferromagnetic properties via the manipulation of surface electron spins.

When considering nanoscale materials, there are many possible mechanisms behind the observation of paramagnetic or ferromagnetic ordering at the nanoscale [20]. One explanation is that at the nanoscale there are more undercoordinated atoms on the surface than in the bulk due to the larger surface area to volume ratio. These undercoordinated atoms have an excess of electrons (i.e. dangling bonds) and can be a source of magnetic spin. A second mechanism involves altering the surface of the NC by the introduction of atomic vacancies via the removal of atoms, such as oxygen [4, 14, 22–24]. A third mechanism involves the chemical modification of the surface of NCs by attaching (or removing) different organic molecules (commonly referred to as ligands) to the surface

[25–29]. Recently, it has been suggested that upon the removal of surface ligands the under coordinated atoms surface can reconstruct and form new bonds which are associated with trap states[30].

Organic ligands, also commonly referred to has surfactants, serve multiple purposes for NCs. During the chemical synthesis of nanoparticles, ligands can control the growth rate, particle shape of the NCs, prevent aggregation, and affect the final size distribution [25, 25, 31–34]. There are a host of suitable ligands that have been employed over the years (Figure 1.2). As an added benefit, the ligand surface layer saturates dangling bonds and screens the particle from the environment, thus prolonging the shelf life of these particles. For instance, ligands can stabilize materials against oxidative corrosion by forming a layer that makes oxygen diffusion difficult [35]. The organic ligand chain lengths have been shown to affect the shape of CdSe NCs [2] and it has been shown that the longer (shorter) chain lengths lead to increases (decreases) in NC reaction rates, which dictates size distribution and crystal defects [35].

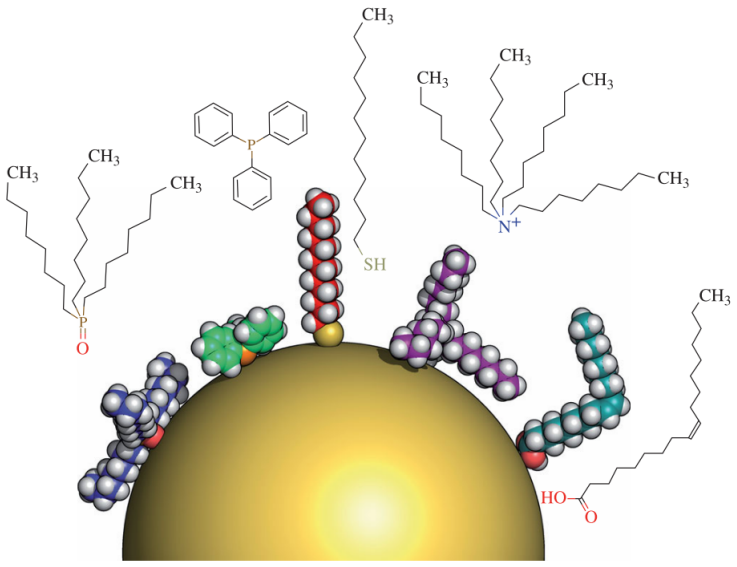

Figure 1.2: An idealy smooth, spherical 5 nm nanoparticle drawn to scale with different hydrophobic ligand molecules all drawn to scale. The diagram depicts, from left to right, trioctylphosphine oxide, triphenylphosphine, dodecanethiol, tetraoctylammonium nitrate, and oleic acid [36].

This thesis probes various mechanisms by investigating how magnetic properties are altered after the removal of NC surface ligands. It has been shown that the surface ligands do not fully passivate the NC surface, as the typical ligand coverage is about 60% of all surface atoms which is approximately 3 ligands/nm^2 [37]. This undercoordinated surface results in dangling bonds and recent work by Biadala and coworkers have shown that the dangling bonds can couple to excitons and form magnetic spin polarons [38]. This thesis primarily describes how surface ligands alters the magnetic properties of CdSe, ZnO, and CdS/ZnS core/shell nanoplatelets (NPLs), where for CdSe and ZnO NCs we perform surface modifications by reducing the surface coordination and for CdS/ZnS NPLs we examine the interaction of Mn dopants with surface layer.

1.1.1 Prior Work in Magnetic Nanomaterials

Though much work has been devoted on studying the optical properties of chalcogenide semiconductor materials, very few magnetic measurements have been performed on undoped II-VI NCs leading to an incomplete understanding of II-VI NCs. The majority of common magnetic materials, such as Fe_2O_3, have partially filled d shells and leaves unpaired electrons which leads to magnetic ordering[39]. For II-VI semiconductors, however, the d shells are fully occupied and should not exhibit paramagnetic or ferromagnetic responses. Recently, oxide materials such as ZnO nanoparticles [40, 41] and CdO nanorods [42] how been reported to exhibit room-temperature ferromagnetism. When fully occupied d orbitals systems (d^{10}) like a Cd^{2+} or a Zn^{2+} compounds exhibit magnetic propertiesm they are commonly referred to as exhibiting d^0 magnetism [43–46]. The magnetic properties from these d^0 systems are attributed to vacancies, interstitial ions [41], or dangling bonds [22, 47].

1.1.1.1 Methods of imparting magnetism in d^{10} materials

Historically, the magnetic properties of semiconducting nanocrystals arise from impurities or dopants like Co, Fe, Mn, and Ni [4, 15–20]. Doping with chemical impurities

like Co or Ni in a traditionally nonmagnetic system can introduce unpaired spin states which lead to the new magnetic behavior [20, 48] and the level of doping has an impact on the magnetic behavior by altering the type of magnetic ordering. Kumar et. al [47] found that increases in magnetic saturation, M_s, in Ni doped CdSe are suggested be attributed to stronger Ni-Ni interactions and charge transfer between surface atoms while the decrease is explained as a super-exchange between Ni and core atoms. Inamdar et. al. [48] found similar results for Co doped ZnO NCs where increasing the [Co] from 0.6 % to 1.9 % leads to a magnetic phase transition from a paramagnet to ferromagnet, with the emergence of magnetic hysteresis.

It has been suggested that nonmagnetic impurities (i.e. unpaired p electrons of O atoms) can produce a magnetic moment leading to magnetism [22]. Jayalakshmi *et.al.* [49] suggest that the low electronegativity (3.44 eV) of O atoms allows for spin polarization of neighboring atoms at the surface as the electrons are less tightly bound and less likely to form bonding pairs. This leads to "free" electrons that can become spin polarized and promote long range magnetic ordering. Lu *et.al.* [22] have also showed theoretically that carbon on the surface of SnO_2 nanoparticles can promote ferromagnetic ordering. In contrast, Sundaresan et. al. [14] have theoretically shown that C substituted inside of SnO_2 nanoparticles would be nonmagnetic like the bulk. Therefore the location of the dopant material may have a direct effect on the magnetic properties of some nanoparticles [22].

Going beyond the effect of dopants, as the surface to volume ratio increases, effects of the surface begin to dictate the magnetic properties of the nanosystem and nominally diamagnetic materials can become paramagnetic or ferromagnetic [50]. Recently, oxide materials such as CeO_2, Al_2O_3, ZnO, In_2O_3, and SnO_2 have shown ferromagnetic behavior (i.e. magnetic hysteresis) at room temperature [4, 14, 22–24]. The underlying mechanism, proposed by Sundaresan et. al. [14], is that the ferromagnetic properties are inherent to metallic oxide NCs due to oxygen vacancies. An exchange interaction emerges between localized, trapped electrons from oxygen vacancies on the surfaces of NCs [14, 51]. One

such example is seen in CdO nanoflowers, where these materials were annealed in various mixtures of argon and oxygen gases ($Ar:O_2$) and exhibited decreased M_s as the ratio of oxygen increased [40]. A similar observation has been reported for ZnO NCs [52] and ZnO nanorods (NRs) [24], where post annealing in oxygen rich conditions reduces the magnetic saturation, M_s. Annealing ZnO in vacuum, however, has been suggested to produce more oxygen vacancies and promotes larger magnetization values [41]. Long range ferromagnetic ordering may also arise from conduction electrons becoming spin polarized as a result of oxygen vacancies[41]. To make things more complex, oxygen vacancies can allow electrons to couple with dopants, like Cu atoms, thus producing long range magnetic ordering [53].

Oxygen vacancies are not the only surface features of NCs that affect the magnetic properties in thin films, nanowires, nanoplatelets, and nanoparticles. Due to an inherently larger aspect ratios (or surface to volume ratio) than the bulk allows, surface ligands emerge to affect the magnetic properties of nanomaterials [26, 54, 55] . Experiments show ferromagnetism in ZnO NCs are governed by donor or acceptor molecules on the NC surface [26]. Garcia et. al. [54] showed that ZnO capped with dodecanethiol, dodecylamine, and tryoctylphosphine oxide (TOPO) ligands change the magnetic response of the NCs, where ZnO capped with TOPO exhibited the strongest magnetic response. Reports on CdSe nanorods from Verma *et.al.* [43, 47] capped with amines and thiols exhibit room temperature ferromagnetism while Meulenberg et. al [55] have shown that CdSe NCs passivated with TOPO and amines exhibit weak paramagnetic properties. All of this work suggests that magnetism in these systems is complex and not well understood.

Recently, reports suggest that dangling bonds on the surface of NCs may lead to magnetism in nominally nonmagnetic materials [18, 49, 56]. Biadala *et.al.* [38] have optically probed the dangling bonds on the surface of CdSe NCs. There are a number of ways dangling bonds may exist, including an under coordinated surface or surface vacancies [18, 56]. Infante's group has shown ligand removal from CdSe NC surface can result in surface reconstruction leading to the formation Se-Se bonds [50] and I believe that

the new Se-Se bonds are potentially a source of magnetic spin states. The majority of this thesis investigates how to control the number of dangling bonds and examine how that affects the magnetic properties of II-VI NCs.

1.1.2 A brief refresher on magnetism

There are many classifications of magnetic materials, but most materials can be divided into three main categories: diamagnetic, paramagnetic, or ferromagnetic materials. Firstly, materials that generate a linearly negative magnetization, which is considered to oppose an applied magnetic field, H, are classified as diamagnets [39]. Second, materials with a linearly positive induced magnetization to an external magnetic field are considered paramagnets [39]. Lastly, materials that retain spontaneous magnetization, or remnant magnetization, once the external field is removed are considered ferromagnets [39]. The distinguishing characteristic of ferromagnets is an irreversible nonlinear response of magnetization, or hysteresis (Figure 1.3), to an externally applied magnetic field (Figure 1.3). The remnant magnetization or remanence, M_r, is the magnetization when H is equal to zero. The magnetization saturation, M_s, is the magnetization value the M(H) curve approaches asymptotically, usually occurring at large fields. The coercive field or coercivity, H_c, is the field required to reduce M to zero. Generally, the coercivity defines how "soft" or "hard" ferromagnets are, where the larger the H_c the harder the ferromagnet becomes and the smaller the H_c the "softer" the ferromagnet. The hysteresis loop is essential to understanding ferromagnetic materials, because it combines information on an intrinsic magnetic property M_s and two extrinsic properties M_r and H_c which are affected by physical properties like shape, size, and surface roughness along and defects.

For ferromagnets, the spontaneous magnetization or atomic alignment of magnetic moments depends on temperature and becomes zero at a specific temperature often referred to as a Curie temperature, T_c. No material is known to have a higher Curie temperature than Co (T_c = 1388 K). Above T_c, M_s(T) is zero and ferromagnets can

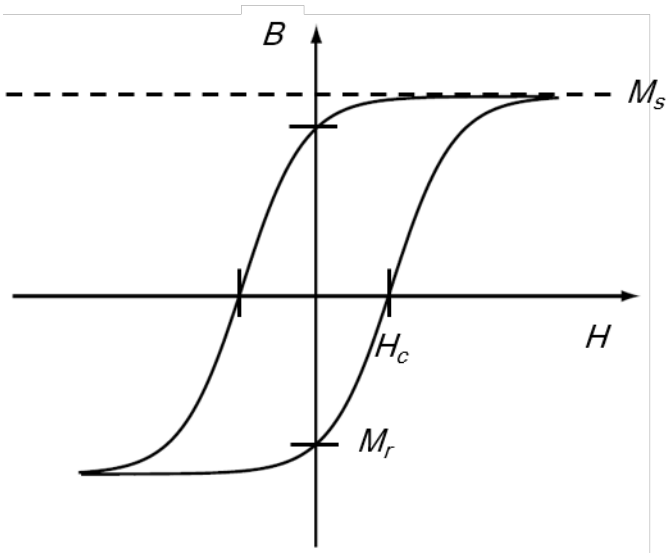

Figure 1.3: Generic Magnetization curves for ferromagnetic materials that exhibits magnetic hysteresis. Where H_c is the coercivity or field required to reduce the magnetization (M) to zero, M_r is the remnant magnetization or remaining magnetization when $H = 0$, and M_s is the magnetic saturation or the maximum value of magnetization.

become paramagnetic. Although M_s is zero at or above T_c, an applied field can induce alignment of some of the atomic moments producing a small magnetization, M, which varies linearly with H except at very large fields. The temperature dependence or the magnetic susceptibility, χ is defined as follows [39]:

$$\chi = \frac{M}{H} \tag{1.1}$$

where M is the magnetization and H is the applied magnetic field. For paramagnets, the temperature susceptibility follows the Curie Law [39] (Figure 1.4a):

$$\chi = \frac{C}{T} \tag{1.2}$$

where C is the Curie constant [39] defined as,

$$C = N\mu_0\mu_B^2/k_B \tag{1.3}$$

where N is the number of magnetic "ions", μ_0 is the permittivity of free space, μ_B is the Bohr magneton, and k_B is the Boltzmann constant. At high enough temperaturers,

ferromagnetic materials lose the ability to spontaneously align at the Curie temperature, T_C, and the susceptibility follows a Curie-Weiss law [39],

$$\chi = \frac{C}{T - T_c} \tag{1.4}$$

We also consider a modified Curie law [39] which takes into account temperature-independent contributions to the susceptibility,

$$\chi = \chi_0 + \frac{C}{T - T_c} \tag{1.5}$$

where χ_0 is the temperature-independent component. The temperature independent contributions can be described by both the Pauli and Landau susceptibility (Figure 1.4 b and c). The positive Pauli susceptibility usually refers to paramagnets and the negative Landau susceptibility usually describes diamagnetic materials (i.e. a perfect diamagnet has a χ = -1) [39].

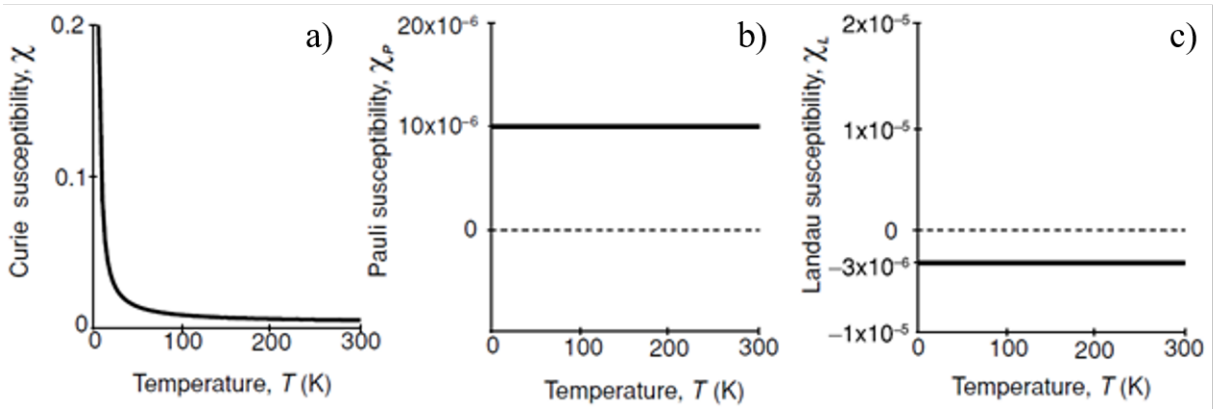

Figure 1.4: Different types of magnetic, temperature susceptibility [39] including Curie susceptibility (a), Pauli susceptibility (b), and Landau susceptibility (c). Generally, most paramagnets follow the temperature dependent susceptibility. Pauli susceptibility stems from free or delocalized electrons that align paramagnetically independent of temperature. Landau susceptibility refers to diamagnetic materials, which exhibit a negative susceptibility [39]

From Brillouin theory, the magnetic susceptibility is written in terms of an effective moment μ_{eff} or in effective Bohr magnetons, μ_{eff}, as follows [39]:

$$\mu_{eff} = g\mu_B\sqrt{J(J+1)} \tag{1.6}$$

where g is the g-factor (usually assumed to be 2), μ_B is the Bohr magneton, and J is the total angular momentum quantum number. For paramagnetic materials, the induced magnetization M is positively proportional to H, where in diamagnets that relation is negative. The magnetization curve can be described as follows [39]:

$$M = m_s \underbrace{\left[\frac{2J+1}{2J}\coth\left(\frac{2J+1}{2J}x\right) - \frac{1}{2J}\coth(\frac{x}{2J})\right]}_{B(x)} \tag{1.7}$$

where $B(x)$ is a Brillouin function and m_s is the maximum magnitude of the magnetic moment or magnetic saturation [39] that can be defined as,

$$m_s = Ng\mu_b J \tag{1.8}$$

The variable x is the dimensionless ratio of Zeeman energy to the thermal energy [39] and defined as follows,

$$x = \frac{g\mu_b JB}{k_b T} \tag{1.9}$$

where T is the temperature. In the case of $J \to \infty$, the Brillouin function reduces to the Langevin function as shown in Figure 1.5. Physically, as the number of spin mechanisms increases, J will also take on larger values. As J $\to \infty$ the brillouin function reduces to the Langevin function [39],

$$\mathcal{L} = (\coth(x) - 1/x) \tag{1.10}$$

Note in the Brillouin function, J determines the curvature of the M(H) curves (Figure 1.5), the lower the J value, the "sharper" the M(H) curve and as J increase in value the M(H) curve broadens.

For the purposes of this thesis, J is used to help identify possible sources of magnetism. By examining the valence electronic configuration the J values of select elements can be determined following Hund's rules [39],

1. Maximize the spin, S, for the configuration

2. Maximize the angular momentum, L, consistent with S

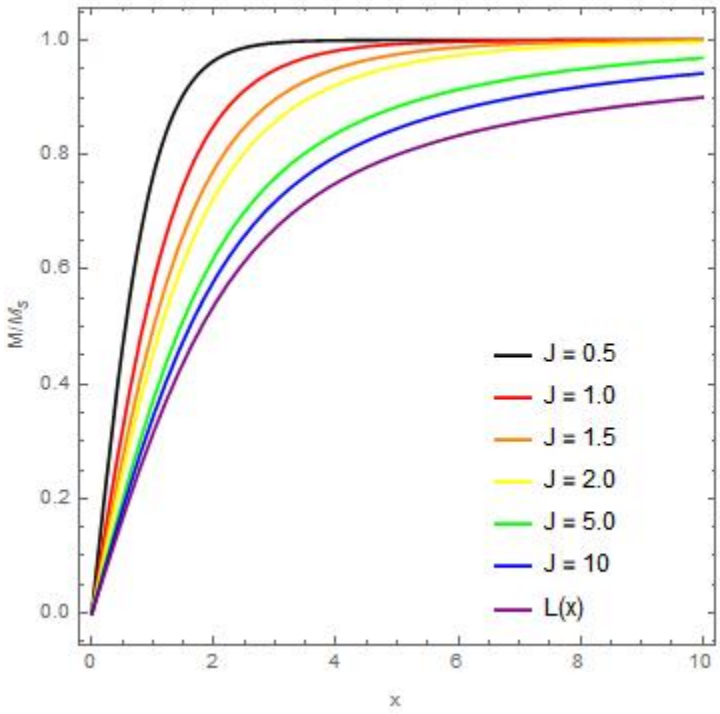

Figure 1.5: Brillouin function increasing total angular momentum quantum number, J, to $\rightarrow \infty$ which is considered the classical limit and the Brillouin fucntion simplifies to the Langevin fucntion (Equation 1.10)

3. Couple L and S to form the total angular momentum, J, as follows,

   (a) $J = L$ - S if the shell is less than half full

   (b) $J = L + S$ if the shell is more than half full

   (c) $J = S$, $L = 0$ if the shell is exactly half full

To put these rules into context, an example for the Mn^2+ state is given as follows. The valence electronic structure for Mn^2+ is a $3d^5$ state, where there are 5 valence electrons and in the d shell 5 possible L values (-2, -1, 0, 1, 2). The total $L = 0$ and thus $J = 5/2$. To organize this information a table is drawn (Figure 1.6). Similarly for neutral O $J = 2$, Cd^{1+} $J = 0.5$, and Se^{1-} $J = 1.5$.

Further reading can be found in most solid state physics or magnetism textbooks, I recommend "Magnetism and Magnetic Materials" by Coey [39].

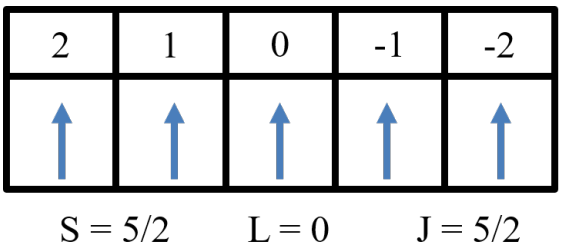

Figure 1.6: Organizational table for determining the total angular momentum quantum number, J, for a Mn^{2+} state. The columns are to represent the possible angular momentum, L, values the electrons (arrows) can assume. The electrons are filled to maximize the total spin, $S = 5/2$, and from this the total L value is optimized $L = 0$. Through Hund's 3^{rd} rule $J = 5/2$

CHAPTER 2

METHODS

2.1 Nanocrystal Synthesis

2.1.1 Materials

Cadmium carbonate ($CdCO_3$) (98%, Aldrich), selenium powder (Se) (100 mesh, 99.5% trace metals basis, ACROS), tri-n-octylphosphine oxide (TOPO) (99%, Aldrich), tri-n-octylphosphine (TOP) (90%, Aldrich), 1-octadecene (ODE) (90%, Aldrich), stearic acid (SA) (95%), toluene (99.5%, VWR), methanol (Fisher, 99.9%), ethanol (Alfa Aesar, 94-96%), zinc acetate dihydrate ($Zn(OAc)_2{\cdot}2H_2O$), tetramethylammonium hydroxide pentahydrate (TMAH), dimethyl sulfoxide (DMSO), and ethyl acetate. All chemicals were purchased and used without further purification.

2.1.2 Synthesis of CdSe

CdSe nanocrystals (NCs) were synthesized via a modified hot injection method from Shakeri and Meulenberg [57] and Webber and company [58]. There are various modifications in the literature that can be used to synthesize CdSe nanocrystals (NCs) [2, 57–60], most probably the most well known approach by Peng's group [9]. For the purpose of this thesis, the modified hot injection method was ideal, because it yielded the largest amount of NCs and could be scaled down to produce fewer NCs if needed. The following text describes in detail, how to perform the above hot injection reaction used in this thesis. To begin, prepare the Cd precursor by combining 590 mg (3.4 mmol) of $CdCO_3$ with 5.0 g (12.9 mmol) of TOPO and 5.0 g (17.6 mmol) of SA in a three-neck, round bottom flask along with a magnetic stir-bar. After combining the precursor materials, attach the thermocouple (TC), a condenser line, and gas inlet line as shown in Figure 2.1.

Once all of the Cd precursors are combined, the reaction vessel is purged for 5 min with flowing N_2 before heating. After the N_2 purge, the Cd precursor is heated to 120 °C; note

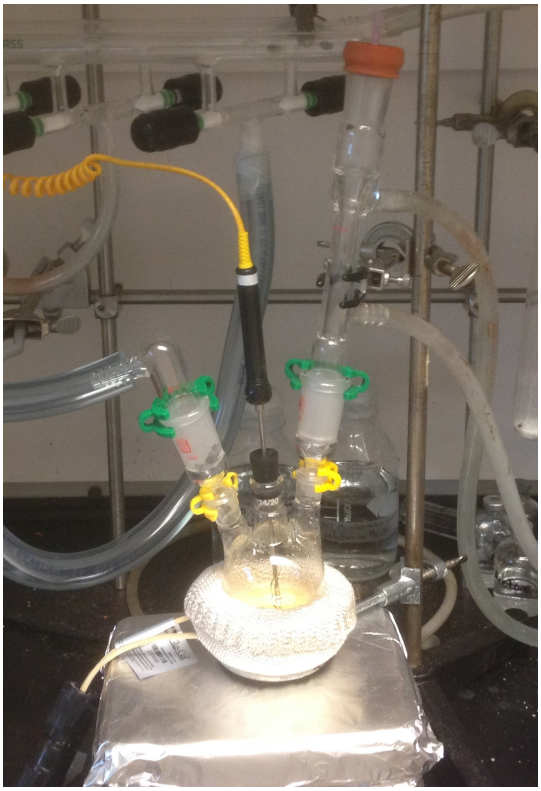

Figure 2.1: Typical experimental setup using a round bottom flask and water cooled condenser (left). The round bottom flask is heading using a hemispherical heating pad while utilizing magnetic stirring and temperature readings are measured using a thermal couple. All N_2 gas is delivered through a Schlenk line. A typical crimp vial with Se powder and TOP under N_2 atmosphere (right). The solution will become yellowish in color as the Se dissolves into solution

the waxy organics (TOPO and SA) should begin to melt around 40 °C and be completely melted by 70 °C. The solution is held isothermally at 120 °C for 1.5 hr under flowing N_2 and constant stirring. Initially, the solution should be cloudy and will become clear with visible $CdCO_3$ grains during this process. After heating for 1.5 h at 120 °C, heat the mixture rapidly to 360 °C at 50 °C/min and hold at 360 °C for an hour. Initially, the solution should be clear, but after heating for an hour, the solution becomes slightly yellowish in color at 360 °C, and heating beyond an hour leads to a dark yellowish or a dark amber solution. Note, if the heating apparatus is not properly sealed, air may contaminate the mixture and the Cd precursor becomes black. At this time, the air contamination of the reaction flask does not appear to affect the NC growth.

To form the Se precursor, dissolve 0.383 mg (4.9 mmol) of Se powder in 5.0 mL of TOP under N_2. To maintain an air free condition, the Se precursor is dissolved in a crimp vial that has been purged with N_2 to prevent oxidation (Figure 2.1). The vial is then sonicated for 5-10 min to fully dissolve the Se powder in TOP. Note, the Se will crash out of solution after an hour or more; it is therefore important to re-sonicate before drawing for hot injection. Anecdotally, the reaction appears to be exothermic and will dissolve if the Se solution is shaken vigorously, so minimal sonciation is required. After the Cd precursor has been heated to 360 °C and held isothermally for 1 hr, quickly inject ($\sim$2 s) 5 mL of the Se precursor into the reaction vessel followed immediately by 5 mL of 1-ODE. Allow the reaction to proceed until the desired size NCs are formed. NC size can be quickly determined by pulling aliquots of the reaction mixture and performing UV-Vis spectroscopy. Anecdotally, however, I have found that reaction times of about 10 s produce 4 nm size NCs, $\sim$1 min produce 5-6 nm NCs, and reaction times of $\sim$4 min produce 8 nm NCs. Also, it has been found anecdotally that the reaction is still successful if scaled up or down so long as the molar ratios are scaled accordingly.

Once the desired time has passed, quench the reaction by removing the heat source. Note that the reaction temperature is too high to quench in an ice/water bath (the reaction vessel will shatter). Additionally, quenching the reaction that quickly will result in an increase of non-uniformity of NC size. When the solution cools to 50 °C, 10 mL of toluene is injected into the reaction flask to facilitate the purification process. The reaction mixture is separated into three 45 mL centrifuge tubes with about 20 mL of NC slurry in each vial. To each slurry, 10 mL of toluene is added to each tube along with 6 mL of ethanol and 5 ml of methanol. The solution is shaken vigorously for $\sim$30 s, mixed for 30 s using a vortex mixer, and centrifuged for 5 min at 3050 rpm. After centrifugation, two distinct layers should form. The bottom layer should be a colored or dark precipitate and the top layer should be a clear supernatant. Decant the supernatant and disperse the precipitate in hexanes. Note, adding too much hexanes will make separating the NCs from

solution impossible. The final product is always dispersed in solution and stored in the dark under N_2 at 15 °C. The solution can then be purified repeatedly to achieve the desired number of purification as described below.

2.1.3 ZnO Synthesis

ZnO NCs were synthesized by one of two synthetic methods, the first is a base-initiated hydrolysis (Figure 2.2) and Zn^{2+} condensation technique described by Gamelin's group [61] while the second method follows a modified one-post method. The hydrolysis method follows by dissolving 22 mmol of TMAH in 40 mL of ethanol and added dropwise to a stirring solution of 13 mmol of $Zn(OAc)_2{\cdot}2H_2O$ in 135 mL of DMSO at room temperature. After the addition of the Zn precursor, the reaction quenched by adding 50 mL of ethyl acetate. The reaction consistently yields NCs with d = 6.0 nm in size, because the reaction is not time dependent. To grow NCs with d = 4.5 nm, $Zn(OAc)_2{\cdot}2H_2O$ is dissolved in a 2:1 DMSO:ethanol solution while stirring the solution in an ice bath. NCs were collected by centrifugation and NCs are re-dispersed in ethanol.

The second method follows a modified one pot approach described by O'Brien's group [7] and Yin's group [62]. In a standard reaction, a 1:1 molar ratio of $Zn(OAc)_2{\cdot}2H_2O$ and OA are mixed in 15 mL of OD. The reaction is heated under vacuum to 120 °C and held isothermally for 1.5 hr. This step is important to degas the Zn acetate. The solution will be clear after the degasing step, but gradually turns white during the temperature ramp up. The solution is then heated to 286 °C, and held isothermally until the desired size is achieved (5-30 min). The growth rate is plotted in Figure 2.3; after 20 mins the growth rate slows down significantly. NCs were collected after centrifugation and re-dispersed using hexanes.

Figure 2.2: Typical reaction set up for ZnO NCs using acid base hydrolysis usiing a glass Burette that allows the solution to be add drop-wise into an Erlenmeyer flask with constant magnetic stirring. The entirety of the reaction is performed in air at room temperature

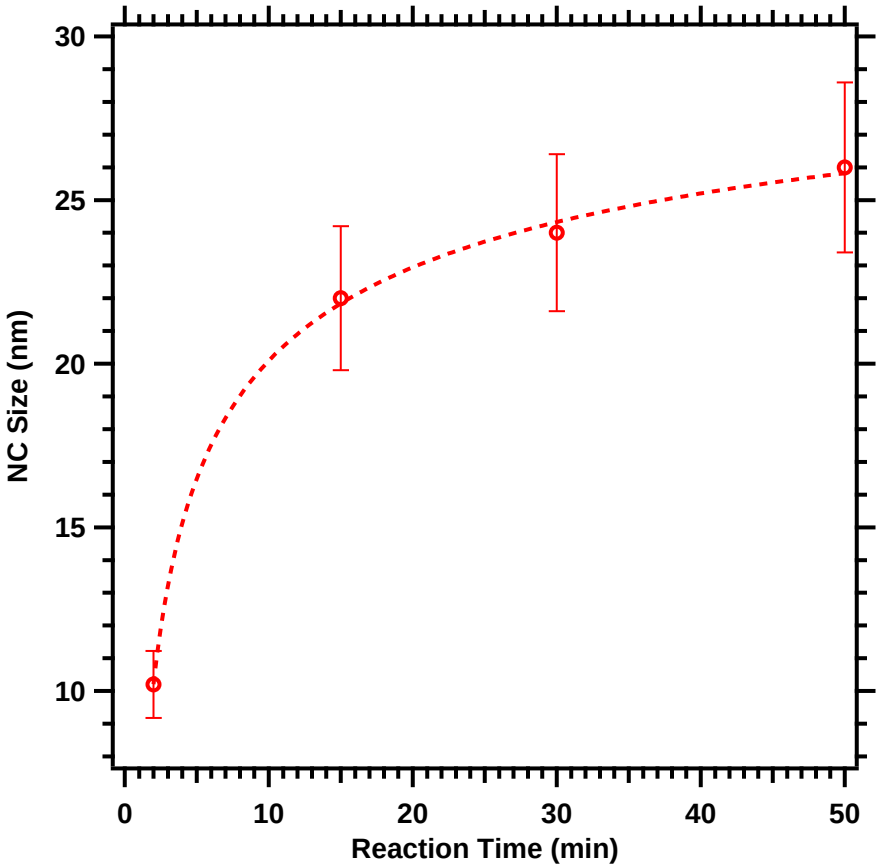

Figure 2.3: ZnO NC sizes as a result of various reaction times for the one-pot method by Andelman *et.al.* [7]

2.1.4 Post-processing of the nanocrystals

Post-processing strategies (i.e. purification or washing methods) are adapted from the procedures developed by Shakeri and Meulenberg [57]. To begin the purification process, start with NCs that have been cleaned once, as described in the prior section. For CdSe NCs, either 20 mL of ethanol or a 11:10 mL ratio of ethanol:methanol is added. Using ethanol only is a gentler procedure, where less ligands are removed while the ethanol/methanol mixture is a more aggressive wash, and can lead to a large number of ligands displaced from the NC and even the possibility of etching the NC surface [57, 63]. After the non-solvent solution has been added, the NC solution is shaken vigorously for ∼1 min before centrifuging at 3000 rpm for 5 min. The supernatant is decanted and discarded while the NCs are re-dispersed in 5 mL of hexanes. Repeat the purification as needed but it is worth noting that the NCs will become less stable in solution as more ligands are removed from the surface and each successive purification step a small amount of NCs will be lost in the supernate. The ZnO NCs are purified similarly, however, the solvent and non-solvents are reversed. Ethanol is the primary solvent while hexanes is the flocculant and the NC solution to antisolvent ratio are still 50/50.

2.1.5 Ultraviolet-visible and photoluminescence spectroscopy

Ultraviolet-visible (UV-vis) and photoluminescence (PL) spectroscopy is a simple and effective method to extract information like NC sizes for many NC systems including CdSe [3, 37, 59]. UV-vis and PL spectra were collected using a CCD Ocean Optics spectrometer (USB 2000). A deuterium-tungsten halogen lamp was used for the UV-Vis experiments while a 405 nm Thor Labs diode laser was used for the PL measurements. Samples are prepared in solution phase and added to a standard plastic or quartz 1 cm x 1 cm cuvette. Typically, 3 mL of solvent is used for every 0.5 mL of concentrated NC solution.

A typical example of UV-vis and PL spectrum for CdSe NCs are shown in Figure 2.4. In this example, the NCs exhibit the first exciton absorption peak at ∼585 nm and PL at

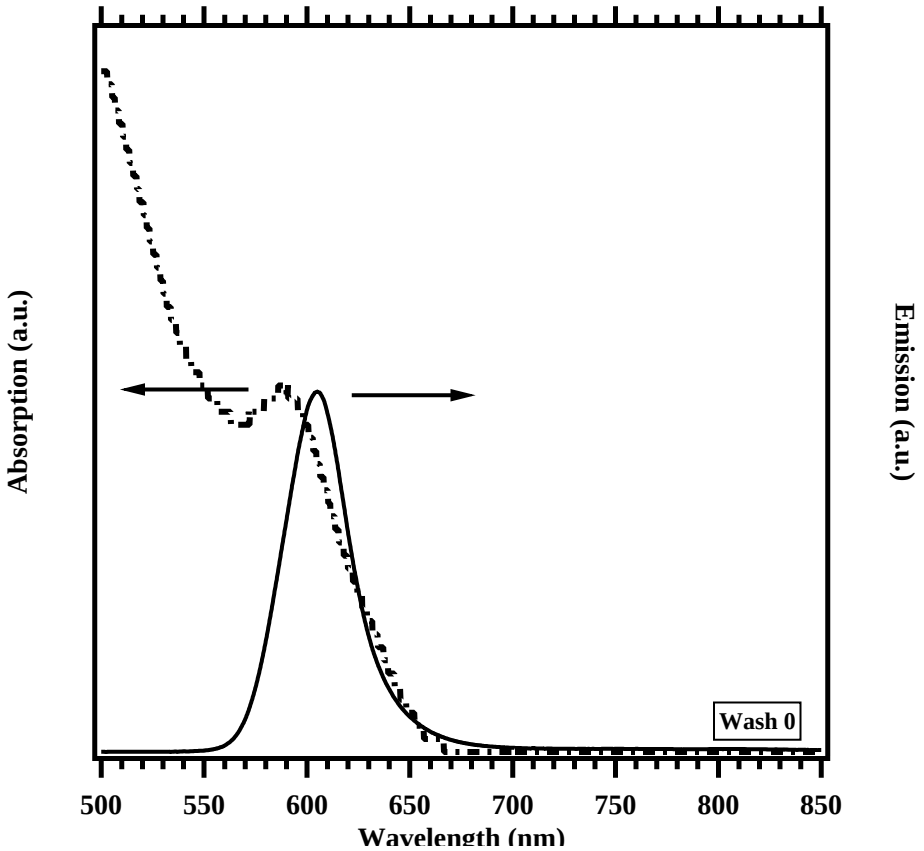

Figure 2.4: Absorption spectrum (red) and florescence spectrum (blue) for CdSe (left) and Example of CdSe with band edge PL at 520 nm

~610 nm, resulting in a Stokes shift (the difference between the absorption band edge and band edge emission) of about 25 nm. The first exciton absorption peak has been shown to be strongly correlated to CdSe particle size (in nm) and can be described by the empirical formula found by Peng's group [59],

$$D = (1.6122x10-9)\lambda^4 - (2.6575x10-6)\lambda^3 + (1.6242x10-3)\lambda^2 - (0.4277)\lambda + (41.57) \quad (2.1)$$

where λ is the first absorption wavelength in nm. For this example, Equation 2.1 yields D = 4 nm for λ = 585 nm.

2.1.6 X-ray diffraction

X-ray diffraction (XRD) is a powerful method to probe both crystallinity and particle sizes of NCs [64]. A brief overview of the theory for XRD is given in Appendix A. Powder

XRD experiments are performed using a PANanalytical XRD diffractometer. Sequences were for θ-2θ scans with Cu K_α radiation using line focus mode. A Pixcel detector and x-ray mirror incident optics were chosen to perform the experiment.

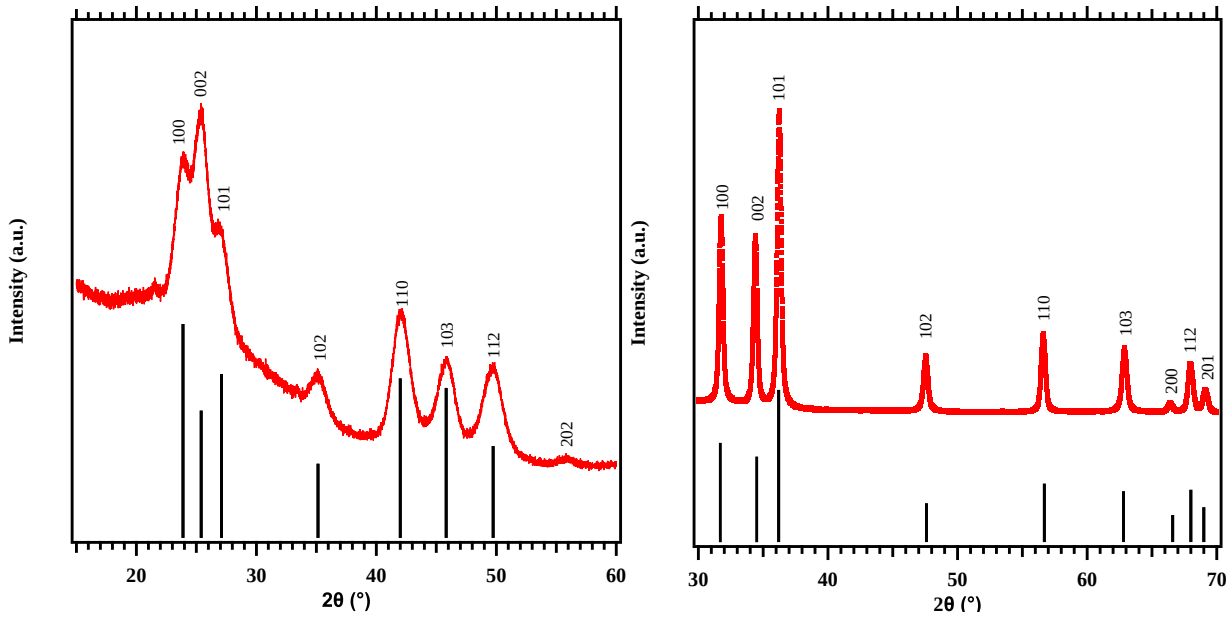

(a) CdSe XRD (b) ZnO XRD

Figure 2.5: Example of typical XRD Pattern for CdSe (left) and ZnO (right) NCs exhibiting wurtzite crystal structure [43, 61]. The black lines are relative intensities from referenced database [65]

In general, to prepare a colloidal sample for XRD, a small amount of the colloidal solution is dripped onto to a glass or silicon substrate and allowed to dry in air or under N_2. If sample quantity is limited, a small (5 mm x 5mm) Si wafer is used instead of the glass substrate. As the sample disperses, the surface tension is enough to retain the solution onto the Si substrate allowing for a more localized sample. A couple of example patterns for CdSe and ZnO NCs are shown in Figure 3.5. Both the CdSe and ZnO examples show wurtzite structure [43, 61] consistent with respected literature reports.

After obtaining the XRD pattern of the NCs, the size of the NCs can be estimated using the Scherrer equation [64] (Equation 2.2) is used to estimate the NC size,

$$\tau = \frac{k\lambda}{\beta \cos\theta} \tag{2.2}$$

where K is a form factor (unitless, but typically takes on a value of 0.9), λ is the x-ray wavelength (1.5 Å), β is the fullwidth half max (FWHM) of the x-ray peak in radians, and θ is the Bragg angle. Applying the Scherrer equation to NCs in Figure 2.5 above we estimate the size of the CdSe sample to $\tau_{CdSe} = 6.2$ nm for $\beta = 1.384°$ at $2\theta = 41.9°$ and the ZnO sample to $\tau_{ZnO} = 22.3$ nm for $\beta = 0.375\ °$ at $2\theta = 36.2\ °$. As NCs decrease in size, peak broadening of the XRD pattern occur as a result of nonuniformity in the nanocrystal sample. This is evident when examining the FWHM, where broader peaks give a larger FWHM value, thus a smaller D value.

2.1.7 Photoelectron spectroscopy

X-ray photoelectron spectroscopy (XPS) measurements were performed to determine the atomic constituents of the material [66]. A brief overview of the theory for XPS is given in Appendix A. The photo-electrons have kinetic energies given by,

$$KE = hv - BE - \phi \tag{2.3}$$

where hv is the energy of the photon, BE is the binding energy of the photo-electron, and ϕ is the work function of the spectrometer.The XPS measurements were performed using either the Al- or Mg-anode. The advantage of using the Mg-anode when examining CdSe samples is because the Mg-anode shifts the Se LMM Auger peaks away from the Se $3p$ peaks [67] (Figure 2.6). To prepare the samples for XPS, NCs films were prepared drop-wise from solution on either a glass or Si substrate and substrates are attached to transfer pucks using either carbon tape, double sided scotch tape, or tacked on with Ta wires. The samples were allowed to dry fully before loading into the ultra-high vacuum chamber. Survey scans are performed from 0-1300 eV with a pass energy of 100 eV and step size of 0.5 eV. The binding energies of Cd, Zn, O and C, elements discussed in this thesis, are given in Table 2.1.

For higher resolution, fine scans are performed near a particular element edge with a pass energy of 20 eV and a step size of 0.2 eV. XPS spectrum for CdSe materials examine

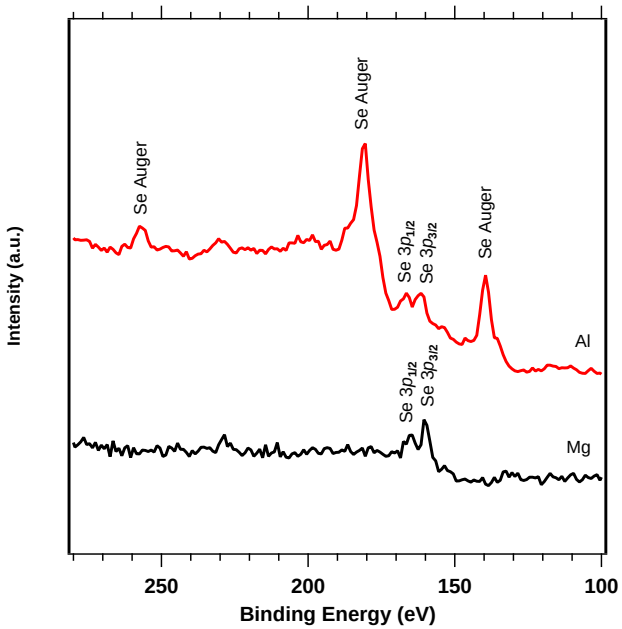

Figure 2.6: Difference between using the Mg- and Al- anodes for XPS on CdSe NCs, where the Se LMM Auger peaks appear around to the Se $3p$ peaks when using the Al- anode.

Cd $3d$ and Se $3d$ photoelectrons (Figure 2.7) and for ZnO materials examine Zn $2p$ and O $1s$ photoelectrons (2.7). It is important to also measure the carbon $1s$ (BE = 285 eV) peak so that XPS spectra can be calibrated to a known reference energy. The examples of Cd $3d$ and Zn $3d$ show doublet peaks as a result of spin-orbit splitting. The Se $2p$ should also appear as a doublet, however, due to the small difference in BE (∼1 eV), it becomes difficult to distinguish between the $2p_{1/2}$ and $2p_{3/2}$. Note the shelf feature at ∼52 eV is associated with Au $5p$.

Cd	BE (eV)	Se	BE (eV)	Zn	BE (eV)	O	BE (eV)	C	BE (eV)
$3s$	772	$3s$	232	$2s$	1195	$1s$	531	$1s$	284
$3p_{1/2}$	652	$3p_{1/2}$	169	$2p_{1/2}$	1045				
$3p_{3/2}$	618	$3p_{3/2}$	163	$2p_{3/2}$	1022				
$3d_{3/2}$	412	$3p_{3/2}$	57						
$3d_{5/2}$	405	$3p_{3/2}$	56						

Table 2.1: Select binding energies for Cd, Se, Zn, O, and C as reported in ref [67] when performing XPS on materials discussed in this thesis.

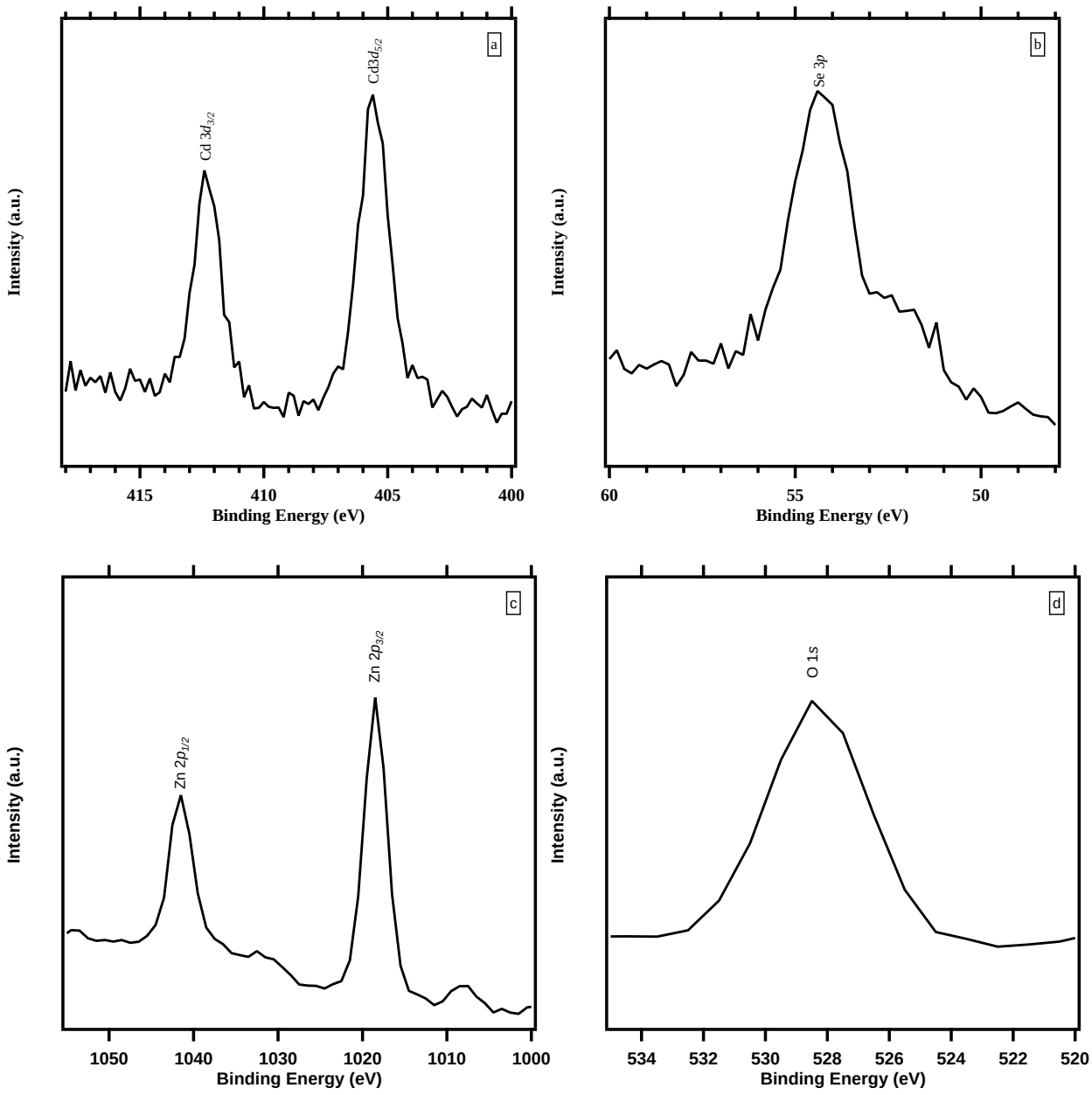

Figure 2.7: Example of typical XPS spectra for (a) Cd, (b) Se, (c) Zn, and (d) O.

2.1.8 Magnetometry measurements

Magnetic measurements were performed using a Quantum Design magnetic property measurement system (MPMS XL 7) using either the direct current (DC) or reciprocating sample oscillator (RSO) sample transport. To minimize the number of magnetic sources, all samples were placed in a polycarbonate pill capsule and then inserted into a plastic sample holder, which is a plastic straw ordered through Quantum Design. Both the pill capsule and plastic straw exhibit diamagnetic responses in the presence of an external magnetic field. It is worth noting that commercially available straws may contain paramagnetic impurities, therefore poly-carbonate straws through Quantum Design are the only ones approved for MPMS. The sample holder is then attached to the sample rod and placed inside of the MPMS sample chamber. Once secured, the chamber is purged 3 times to minimize the amount of oxygen present in the chamber, and finally the sample is centered between the two superconducting coils of the MPMS. After centering, the desired field dependent or temperature dependent sequences are performed.

The following is a detailed explanation on how to properly prepare the colloidal NCs for the MPMS. As a reminder, when working with weakly magnetic materials, remember that non-magnetic tools should be used to prevent contamination with magnetic ions in the sample. Sapphire blades should be used to cut the straws, plastic spatulas should be used to transfer samples, and titanium tools can be used to puncture holes or to transfer samples after being wiped clean with alcohol. Always wear new nitrile gloves when handling new or different samples, again as means to prevent accidental contamination of the sample.

When filling the plastic pill capsules with material, consider one the following procedures depending on sample quantity. If the samples are in the solid phase and enough sample ($\sim$100 mg) is present to fill the pill capsules without leaving a gap in the capsule, then that is the preferred method. If the samples are in the solid phase and only a small amount of sample is available (less than 100 mg) then the larger diameter pill capsule is filled and the lower diameter is applied to compress the sample into the pill capsule. If

samples are still in the solution phase in hexanes or ethanol, then the solution is slowly added dropwise into one of the pill capsules and allowed to dry before inserting into the sample holder.

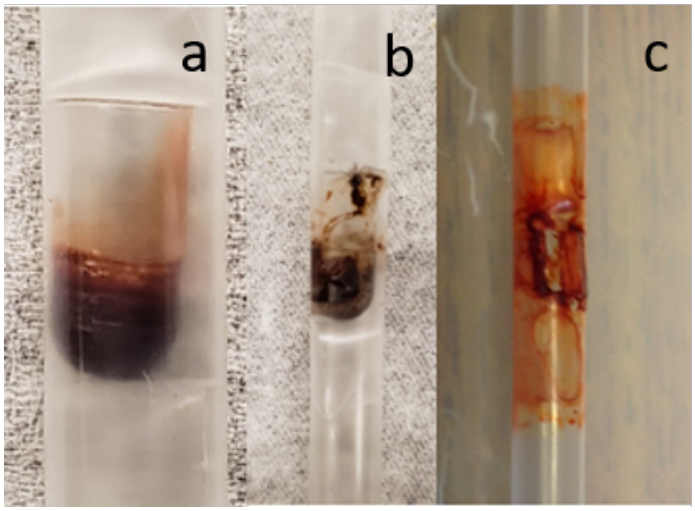

Figure 2.8: Failed attempts at preparing samples for MPMS. (a) depicts a sample prepared using toluene, (b) depicts a sample that was not completely dried and (c) depicts a sample with no pill capsule.

The following are the variations in filing pill capsules for solution phase materials that have been attempted but are not recommended for weakly magnetic samples. The first method involves drop casting the NC solution with toluene into the plastic pill capsules (Figure 2.8a). This method is not recommended because any amount of toluene will deform the pill capsules, leading to a nonsymmetric sample which causes problems when centering the sample for magnetic measurements. Pill capsules that are inserted sideways into the sample holder using a trap door are not a good idea as the sample can fall out of the holder and into the bottom of the MPMS dewar. This can cause issues both from a cleaning and contamination perspective. Pill capsules that are glued sideways are not a good option either because the glue adds another magnetic signal to compete with. Also, in either scenario, a sideways pill capsule would also break the symmetry required to produce a proper voltage curve.

Note, if the sample is still oily (from ODE) the transfer can become very messy. In those types of samples, during the purging sequence the low pressure can cause the oily material to leave the pill capsule, especially if a hole was punched into pill capsule for ease of purging (Figure 2.8b). This is an issue for small grains of materials as well, due to the low chamber pressures can cause the material to exit the pill capsule making measurements difficult. Always use a pill capsule to mount the sample inside the straw, do not attempt to drop cast a colloidal NCs solution inside the straw in an opening of the pill capsule (Figure 2.8c). For colloidal particles the diffusion of material across the sample holder is too vast and is not recommended. Lastly, it is not recommended to take a colloidal sample that that has been dried and then scraped into the pill capsule. The static electricity caused by the friction of scraping is enough to attract or repel the dried material.

To set the pill capsule inside of the plastic straw, use two pieces of a straw to wedge the pill capsule approxiatmely 4" from the top of the straw, as shown in Figure (2.9). The sample should be immobilized when done correctly; this ensures that the sample always remains in the exact same centering position in the MPMS. After the pill capsule and wedge pieces are loaded into a plastic straw, the straws are capped with centering caps (Figure 2.9) and then attached to the sample rod.

Figure 2.9: (left) How a proper sample should look when packed correctly and loaded into the sample holder. (right) Samples should be seated 4" from the top of the sample holder for easy centering in the MPMS.

Load the sample into the MPMS chamber at 300 K to ensure no water crystals form inside of the sample chamber. If using the RSO attachment, the chamber valve should always be open, even while mounting the sample rod. Once the sample is loaded into the

chamber, purge and vent the sample chamber three times to limit the amount of oxygen is present inside of the chamber. The "ready light" should turn green after a successful purging cycle and the chamber is now under partial vacuum.

To center the sample, apply a small field (200 Oe) and initialize the transport. From the DC centering window, perform a full centering scan to locate the sample position. If using the RSO transport it is recommended to us the full centering scan before performing the RSO centering, unless the sample position is already known. Assuming the sample is placed 4" from the top of the sample holder, then the center position is approximately 5 cm. As the sample is oscillated through the SQUID coils, the changing flux induces a current, which is read as a voltage. The magnetization is obtained by fitting to the resulting voltage as the sample is oscillated through the superconducting coils. The voltage is a function of sample position ($V(x)$) and the response is fitted to the following equation:

$$V(x) = 0.9123M\Big[\left(\frac{2}{0.9409+(x-x_0)}\right)^{\frac{3}{2}} - \left(\frac{2}{0.9409+(1.519+x-x_0)^2}\right)^{\frac{3}{2}} - \left(\frac{2}{0.9409+(-1.51+x-x_0)^2}\right)^{\frac{3}{2}}\Big] + V_0 + V' \tag{2.4}$$

where M is the magnetization, x_0 is the expected center position for the type of scan, V_0 is the voltage at the expected center, and V' is the maximum voltage.

There are two types of measurements that are generally performed using the MPMS; the first is an isothermal measurement commonly referred to as magnetization scan, or M(H) scan. The second varies the temperature at a constant magnetic field, commonly referred to as temperature susceptibility or susceptibility scan, or χ(T) scan. The magnetization scans can be performed at any temperatures between 1.8-300 K, although in this thesis most M(H) scans were performed at either 2 K with varying magnetic field. The field begins at 0 T and is increased stepwise to 7 T before reversing to -7 T and finally back to 7 T. A typical magnetization measurement is shown in Figure 5A. If the material under study is weakly magnetic, as is the case for the samples described in this thesis, a diamagnetic signal dominates at large fields, as illustrated by the linear (negative)

component of the M(H) curve at large fields. This is associated with the diamagnetic signal from the sample holder and plastic pill capsules. To remove the diamagnetic signal a linear fit is made at large fields and then subtracted from the data to reveal the weak paramagnetic signal, as shown in Figure 2.10.

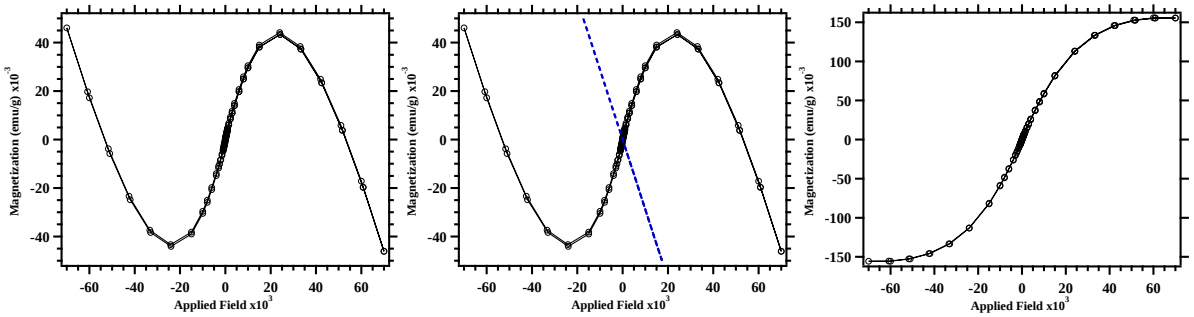

Figure 2.10: Example of background subtraction on CdS nanoplatelet where the raw data (left) exhibits both a strong diamagnetic signal from the sample holder at large fileds. The paramagnetic signals is observed at lower fields. The diamagnetic signal at large fields is fitted linearly and plotted along with the raw signal (middle). The paramagnetic contribution (right) is obtained by subtracting linearly negative $\chi(T)$ from the raw data.

The resultant paramagnetic curve of the isothermal magnetization scan can be fit to a Brillouin function [39],

$$M = m_0 \underbrace{\left[\frac{2J+1}{2J}\coth\left(\frac{2J+1}{2J}x\right) - \frac{1}{2J}\coth(\frac{x}{2J})\right]}_{B_j(x)} \tag{2.5}$$

where $B_j(x)$ is the Brillouin function and,

$$m_0 = Ng\mu_b J \tag{2.6}$$

with g is the gyromagnteic ratio, J the spin value (total angular momentum), N the number of magnetic contributors, and $\mu_B = 9.274\times10^{-21}$ emu is the Bohr magneton. An example of a Brillouin fit is shown in Figure 2.11.

The temperature dependent susceptibility measurements are performed and are categorized as either zero field cooled (ZFC) or field cooled (FC) sequences. For ZFC scans the sample is cooled from 300 K to 2 K without an applied magnetic field while for FC

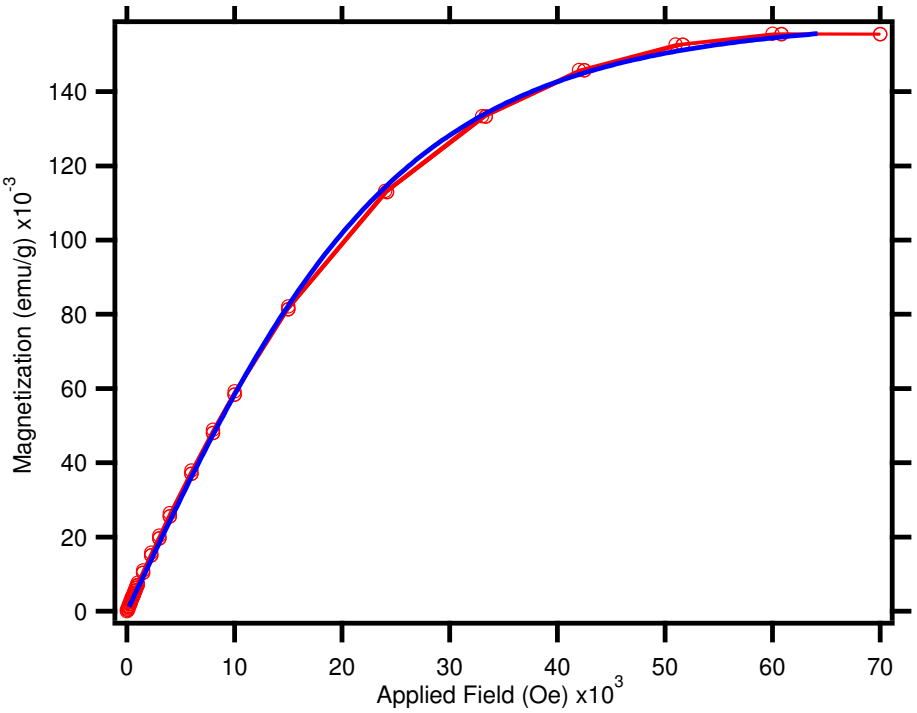

Figure 2.11: Magnetization data after linear subtraction (red) that has been fitted to the Brillouin function (blue) (Equation 2.5)

scans, the sample is cooled to 2 K from 300 K with an applied magnetic field, usually 100 Oe. Note, when cooling to 2 K, the sample chamber is held isothermally at 20 K for an hour to ensure sample thermalization. After cool down, the temperature is ramped to 300 K over the course of 4 hrs at a constant applied field, usually 100 Oe. The measurement yields the magnetic susceptibility, $\chi(T)$, and is fitted to a modified Curie-Weiss Law as follows:

$$\chi = \chi_0 + \frac{C}{T - \Theta} \tag{2.7}$$

where χ_0 is a temperature independent susceptibility term, C is the Curie Constant, T is the temperature, and Θ is the Weiss Temperature. An example of $\chi(T)$ for CdSe is shown in Figure 2.12. The large in crease in susceptibility below 20 K is commonly referred to as a Curie tail, which is a result of the spontaneous spin alignment in the material. The governing mechanism likely due to surface spin states [6]. The negative $\chi(T)$ is expected due to the diamagnetic contribution from the sample holder and organic ligands on the NCs. The small separation between the ZFC and FC curves are likely a result of having a

nonuniform sample distribution in the sample holder. In some instances when preparing the sample for magnetometry, even after performing multiple purging cycles, oxygen can still be trapped in the polycarbonate pill capsules. This can be observed as a small bump around 50 K is associated to oxygen contamination (Figure 2.12b).

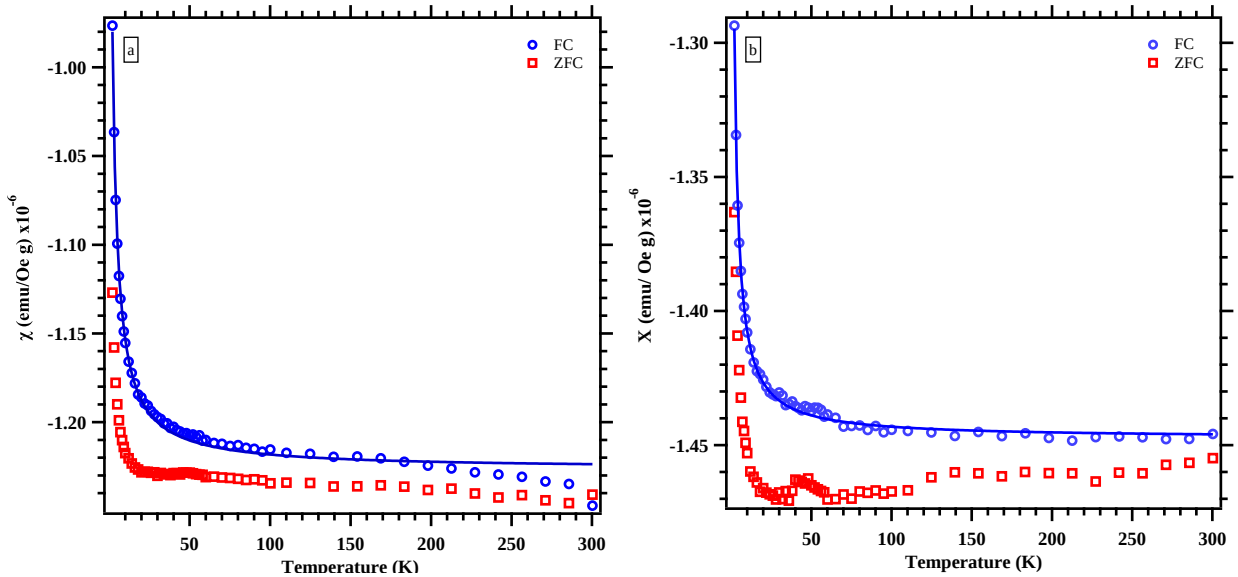

Figure 2.12: (a) A typical $\chi(T)$ curve for CdSe NCs, the zero field cooled (ZFC) (Red) and field cooled (FC) (Blue) follow the Curie Weiss Law (solid lines respectively). (b) A typical $\chi(T)$ where a weak oxygen signal is can be observed around 50 K.

The error propagation follows algebra covered by Taylor [69], where for products and quotients (i.e. $a \times b \times c$ and $\frac{a}{b \times c}$) have an error propagation formula as follows:

$$\delta M = M \times \left[\left(\frac{\delta a}{a} \right)^2 + \left(\frac{\delta b}{b} \right)^2 + \left(\frac{\delta c}{c} \right)^2 + ... \right]^{\frac{1}{2}} \tag{2.8}$$

where M, a, b, and c are measured values and the prefix of δM, δa, δb, δc indicate the error or uncertainty in those values. For a detailed description of uncertainty for magnetization see the methods section in Appendix Chapter B.

CHAPTER 3
INVESTIGATING THE WEAK MAGNETIC PROPERTIES OF CDSE NANOCRYSTALS

3.1 Brief introduction on CdSe nanocrystals

Semiconductor nanocrystals (NCs) or quantum dots (QDs) have been extensively studied due to a wide range of applications in optoelectronic [3] and light emitting devices (LED) [70], as well as biomedicine [71]. These applications utilize the size tunable, quantum confined properties that can modify the optical properties from the red to ultraviolet energy spectrum[12, 60, 72]. Figure 3.1a demonstrates the inverse relationship between QD size and photoluminescence (PL) energy for CdSe/ZnS core/shell QDs. As the NCs decrease in size, quantum confinement of the electronic energy level leads to an increase of the band gap, which is simply observed as a blue shift of the PL (i.e. smaller QDs look more blue than larger QDs). The size tunable PL can be exploited via surface functionalization of the QDs for directed attachment to various cellular components demonstrating the potential role for QDs as biomolecular optical labels inside mammalian breast cancer cells (Figure 3.1a).

The size tunability in the electronic structure becomes important at particle sizees which are ∼2X the size of the exciton Bohr radius, r_B, which is a material dependent property. For CdSe, $r_B = 5.6$ nm [73] which means that as the diameter of the CdSe semiconductor particles reach ∼12 nm, we should observe a shift in the band gap to higher energies. This behavior is depicted beautifully in the first report of high quality CdSe NCs by the Bawendi group where both shifting of the band edge and quantization of the band edge was observed as particles sizes as large as 11.5 nm [74]. Many authors have exploited these properties by growing smaller and smaller CdSe NCs that results in a series of CdSe NCs that can emit throughout the entire visible spectrum [12, 60, 72]. As a result, many

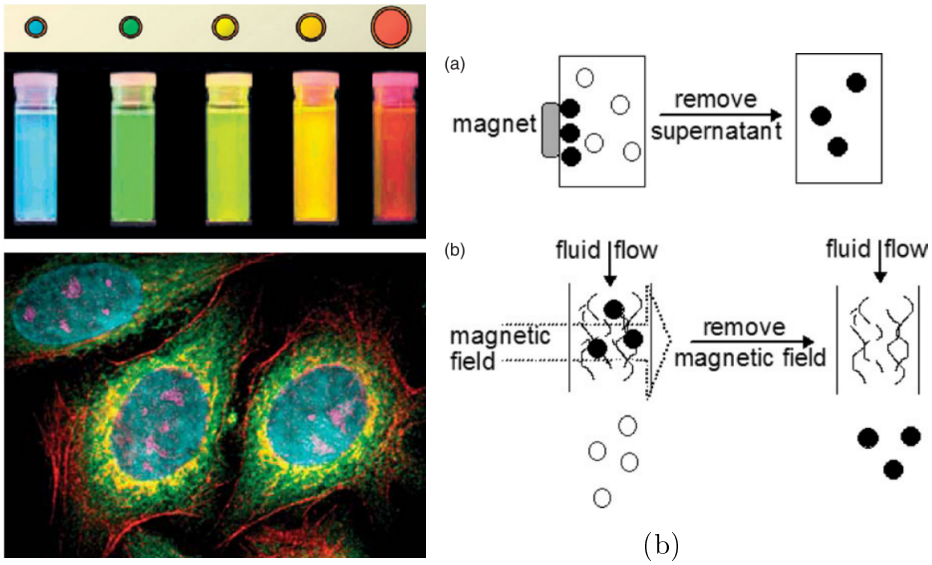

(a) (b)

Figure 3.1: a)The size tunability of QDs is demonstrated where the smaller the NCs, the shorter the photoluminescence emission wavelength (top) and applications as cellular labels in a mammalian breast cancer call (bottom) [12]. b) Illustrates the idea of using magnetic NPs as drug delivery agents in vivo [21].

synthetic methods have been developed [8, 58, 68] and an extensive amount of information on the CdSe NC system has been accrued [19, 57, 59, 66, 70, 72].

Magnetic NCs, like Fe_3O_4, have been used as contrast agents [12], drug deliverers [75], and in cancer treatment like magnetic hyperthermia [76]. For drug delivery, NCs can be guided to or localized at a particular site with the aid of an external magnetic field, as illustrated in Figure 3.1b. Figure 3.1b demonstrates how colloidally stable magnetic NCs can be collected from a static supernate (top) or while in a flowing solution (bottom). In either case, the NCs can be localized with the aid of an external magnetic field, however, a flowing solution better illustrates an *in vivo* application of magnetic nanoparticles. While there are many examples of magnetic NCs, most QDs that posses the size tunable optical properties previously discussed are diamagnetic in the bulk and thus thought to be diamagnetic at the nanoscale. The reason for the diamagnetic nature in CdSe NCs arises from fully occupied d orbitals (d^{10}), commonly referred to as a d^0 magnetic material, and should have no unpaired electrons to align paramagnetically or ferromagnetically.

To impart a net spin, the traditional method of inducing magnetic properties in CdSe NCs is to dope or insert a magnetic impurity into the lattice of the NCs. Typical dopants consist of Cu, Fe, Ni, and Mn which incorporate unpaired *d* shell electrons into the CdSe matrix [4, 15–20]. Although doping NCs can lead to new magnetic properties, the dopants can also disrupt many of the unique size tunable properties observed in the undoped NC. An ideal system would posses the ability to tune and/or induce magnetic properties in a material while maintaining the native optical properties. In prior work, it has been reported that undoped CdSe NCs can exhibit weak paramagnetic or ferromagnetic properties depeding on certain parameter of the QD system [47, 55, 77]. Meulenberg *et al* [55] showed that the surface molecules, or ligands, can induce paramagnetism in CdSe NCs which is consistent with related work on ZnO NCs by Garcia's group [54]. The organic ligands play an important role for colloidal NCs because they prevent aggregation of NCs through electrostatic repulsion or stearic hindrance [36]. In addition, the type of solvent in which NCs are colloidally stable is dependent on the the polarity of the ligands. For instance, polar ligands allow NC stability in polar or aqueous solvents and apolar ligands allow for stability in apolar solvents such as hexanes or toluene [36]. The organic ligands that bond to the NC surfaces can be separated into three classes, based on the covalent bond classification method proposed by Green [78] and illustrated in figure 3.2. The classifications are based on the number of electrons the bonding ligand donates to the bonding atom on NC and are referred to as X-type, L-type, and Z-type ligands. X-type ligands donate one electron, L-type ligands donate two, while Z-type ligands are two electron acceptors [79, 80]. Unfortunately, little has been done to examine if any specific correlations exist between the nature of the type of organic ligand and the report of novel magnetic behavior in these types of materials.

Partly, the lack of understanding of the magnetic behavior of these systems arises from the difficulty in measuring the magnetic properties of undoped species. The prior work on undoped colloidal NCs has been focused on observing the effect of changing organic ligands

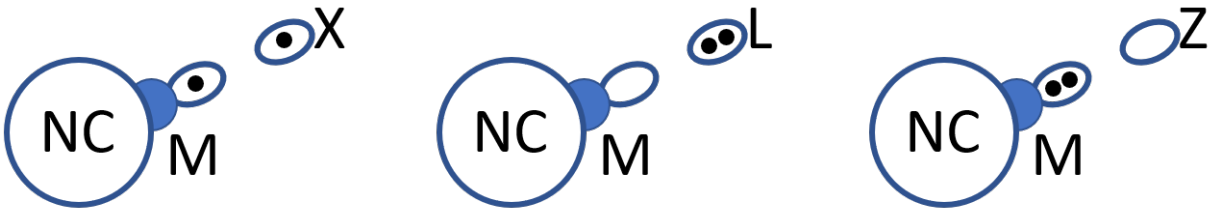

Figure 3.2: Illustration of Green's covalent bond classification method [78] where organic bonds to a metallic atom on the surface of the NC (M). A) X-type ligands donate one electron, B) L-type donate two electrons, C) Z-type ligands accept two electrons.

on the surface of the NCs [55]. Aside from induced magnetism arising from surface ligands, a recent report by Biadala *et al* [38] suggests that the finite size of these systems leads to undercoordinated surfaces with dangling bonds which can lead to unpaired spins. Given the recent results correlating spin polarization via dangling bonds with magnetic properties in NC and nanowire (NW) systems, we have sought to understand if we can (a) control the degree of magnetism via control of dangling bonds and (b) elucidate the atomic nature of the induced magnetism. For instance, recent theoretical work by Infante's group has shown that removal of Z-type ligands leads to Se-Se surface reconstruction and is the source of midgap trap states in CdSe NCs [79]. We hypothesize that these midgap states can combine in such a way to produce a net spin and therefore influence the magnetic behavior. In this work, we show that, when prepared carefully, the magnetic properties of undoped CdSe NCs are a result of the undercoordinated surface. Removal of the organic ligands leads to a reduction of the coordination number of the surface atoms and reveals dangling bonds. As these surfaces are highly reactive [80], the probability for surface reconstruction is high [79] and can lead to new types of surface states. We will show evidence that both control over the number of uncoordinated surface atoms and the degree of surface reconstruction allows control over the resultant magnetic properties in CdSe NC systems.

3.2 Methods

3.2.1 Materials

Cadmium carbonate ($CdCO_3$) (98%, Aldrich), selenium powder (Se) (100 mesh, 99.5% trace metals basis, ACROS), tri-n-octylphosphine oxide (TOPO) (99%, Aldrich), tri-n-octylphosphine (TOP) (90%, Aldrich), 1-octadecene (ODE) (90%, Aldrich), stearic acid (SA) (95%), toluene (99.5%, VWR), methanol (Fisher, 99.9%), and ethanol (Alfa Aesar, 94-96). All chemicals were purchased and used without further purification.

3.2.2 CdSe Synthesis

The synthesis of CdSe NCs is performed using a hot injection method modified from Shakeri [57] and Webber [58] . The concept of the hot injection method is to heat a Cd precursor to 360 °C before injecting a Se precursor, as shown schematically in Figure 3.3. A typical reaction combines 3.4 mmol (590 mg) of $CdCO_3$, 12.9 mmol (5.0 g) of TOPO, and 17.6 mmol (5.0 g) of SA in a three-neck round bottom flask. Prior to heating, the flask is purged with nitrogen (N_2) gas at room temperature. The reaction vessel is heated to 120 °C at about 10 °C/min under N_2 atmosphere while stirring. The Cd precursor is held isothermally for 1.5 h under flowing N_2 while stirring. The Se precursor is prepared by combining 4.9 mmol (0.383 mg) of Se powder with 10 mL of TOP under N_2 under sonication until the Se powder is well dissolved. After the isothermal hold of the Cd precursor at 120 °C, the Cd precursor solution is heated to 360 °C and held isothermally for an hour. At the completion of the 1 hour, 5 mL of the Se precursor is quickly injected into the Cd precursor solution and followed with 5 mL of octadecene. The reaction vessel is removed from the heating mantle once the desired reaction time has elapsed (1-4 min) and is cooled using air to avoid shocking the three-neck flask.

The purification process is performed similarly as reported by Shakeri [57]. Once cooled to about 50 °C, toluene is injected to the vessel to help facilitate the purification process. The mixture is separated equally into three 50 mL centrifuge tubes with an approximate

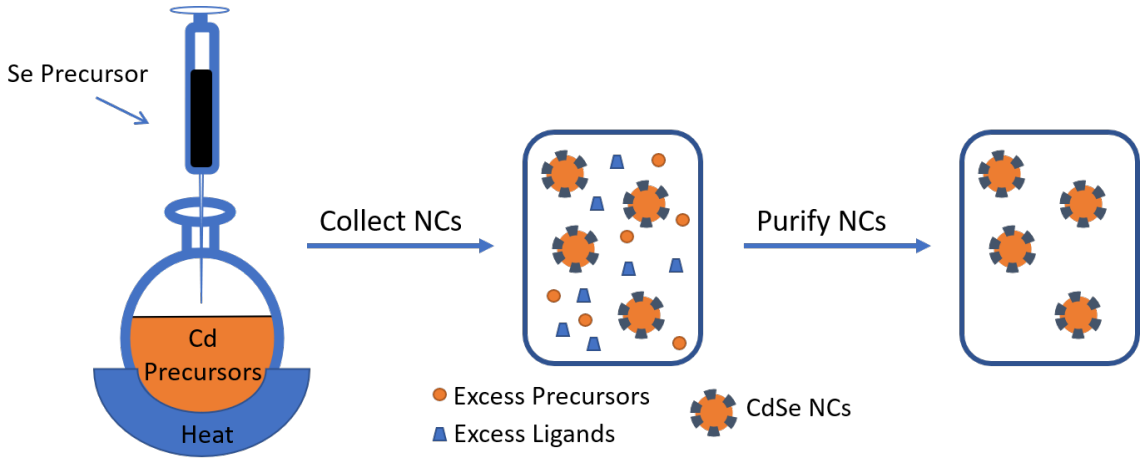

Figure 3.3: Schematic of hot injection method followed by collection and purification of NCs to remove any unreacted or excess precursors and ligands.

volume of 20 mL for each centrifuge tube. To one centrifuge tube, 20 mL of toluene is added followed by 11 mL of ethanol and 10 mL methanol. The tubes are shaken vigorously and centrifuged for 5 min at 1200 rpm. The liquid or supernatant is decanted and the precipitate is resuspended in hexanes. The first purification step is to remove any unreacted precursors and any excess ligands in the supernate as depicted in figure 3.3.

To remove the organic ligands from the surface of the NCs either pure ethanol or a mixture of ethanol/methanol is used during the purification process. To initiate the purification procedure, the rinsed NC solution (as described above) is combined with either 20 mL of ethanol or a 50/50 ratio ethanol/methanol to the NC solution. The solution is shaken vigorously and centrifuged at 1200 rpm for 5 min. The supernatant is decanted and the NCs are re-dispersed in 20 mL of hexanes. The vials are flooded with N_2, wrapped in parafilm, and stored in the dark at 2 °C. This purification process can be continually repeated to a desired number of "washing steps". Note, for an in-depth description see the methods section in Chapter 2.

3.2.3 Magnetometry

3.2.3.1 Magnetometry Measurements

Magnetometry measurements were performed using a Quantum Design magnetic property measurement system (MPMS) with superconducting quantum interference device (SQUID) with the reciprocating sample oscillator (RSO) as the transport attachment. Temperature dependent susceptibility measurements are performed and are categorized as either zero field cooled (ZFC) or field cooled (FC) sequences. For ZFC scans the sample is cooled from 300 K to 2 K without an applied magnetic field while for FC scans, the sample is cooled to 2 K from 300 K with an applied magnetic field, usually 100 Oe.

Isothermal magnetization experiments are performed at either 2 K or 300 K with applied magnetic fields ranging from -7 T to +7 T. A standard magnetic field ramp begins at 0 T, increases to +7 T, decreases to -7 T, and finally increases back to 7 T. For this work, at large fields the diamagnetic components will dominate over the weak paramagnetic signal of the sample. To eliminate the diamagnetic contribution at large fields, the magnetization at large fields can be fit to a linear expression, extrapolated over the total magnetic field range, and the resultant extrapolated line is subtracted from the magnetization curve (Figure 2.10). Subtraction of the diamagnetic component can allow for the observation of phenomena that was previously obscured, such as magnetic saturation due to spin alignment in the sample.

3.2.4 UV-vis and PL

UV-vis and PL experiments are performed using an Ocean Optics USB2000 spectrometer with either a deuterium-tungsten halogen lamp (absoprtion) or a 405 nm diode laser (PL) for excitation . All samples were prepared as colloidal solutions using hexanes or toluene in a 1 cm×1 cm cuvette. Prior to the measurement of the UV-vis or PL spectrum, background scans are taken of the pure solvent to remove the signal of the solvent. For an absorption spectrum both a light and dark background are taken, but for a

PL scan only a dark spectrum is required. A standard sample preparation combines a ~0.05 mL aliquot of a 4 mM NC solution diluted with 3 mL of solvent. For UV-vis measurements, integration times are typically on the order of a few hundred ms and averaged 10 times to reduce the noise. For a PL spectrum integration times are on the order of seconds and averaged 5 times. The absorbance is fitted to the empirical formula by Peng [59] to extract the particle size,

$$D = (1.6122 \times 10^{-9})\lambda^4 - (2.6575 \times 10^{-6})\lambda^3 + (1.6242 \times 10^{-3})\lambda^2 - 0.4277\lambda + 41.57 \quad (3.1)$$

where D is the size the NCs and λ is the absorption peak wavelength (nm).

3.2.5 Density Functional Theory

Atomic simulations were performed using density functional theory (DFT) calculations using the PBE exchange-correlation functional and a double-ζ basis utilizing CP2K 3.0 quantum chemical package [79]. All structures have been optimized in the gas phase using effective core-potentials. The CdSe cluster used in the calculations contained 176 Cd atoms, 147 Se atoms, and 58 Cl atoms, for a total cluster size of 381 atoms. The ratio of Cd to Se was chosen based on experimental reports for similar CdSe NCs [79, 80]. The Cl atoms are used to account for the presence of organic ligands on the NC surface. The surface of the cluster is predominately Cd and the number of Cl atoms was chosen to maintain charge neutrality of the cluster. Infante's group has suggested that the removal of X- or L-type ligands do not alter the electronic structure in the same way as Z-type ligands so we have therefore focused only on simulating the removal of Z-type ligand in the calculations. To simulate the washing method, two approaches were adopted to remove Z-type ligands (1 Cd and 2 Cl atoms) from the surface of the NCs. In the first approach, the NC structure was optimized after the removal of one Z-type ligand. After optimization, another Z-type ligand is removed and the NC undergoes optimization. This process is repeated until the desired number of ligands are removed. In the second approach, multiple ligands are removed at once and then undergo optimization. We envision this method may

emulate real experimental conditions where many ligands may be removed from the particle surface before the NC surface reconstructs.

3.2.6 X-ray diffraction and x-ray photoelectron spectroscopy

X-ray diffraction were performed on an PANalytical X'Pert Pro diffractometer with Cu anode, using the x-ray mirror monochromator and PiXCel detector. Typical sequences interrogated the [110], [103], and [112] Bragg peaks, following Bragg's Law [81]. X-ray photoelectron spectroscopy experiments were performed using a SPECS hemispherical analyzer with an Al K-α anode as the excitation source. Typical XPS survey scans are performed from binding energies 1400 eV to 0 eV with a pass energy of 100 eV and step size of 0.5 eV. Fine scans on particular elements of interest use a pass energy of 20 eV and a step size of 0.2 eV. Samples were prepared from colloidal solutions by adding the solution dropwise to a Si wafer or a glass slide.

3.3 Results and Discussion

3.3.1 Nanocrystal structure and characterization for CdSe NCs purified in air

The ultraviolet-visible (UV-vis) and photoluminescence (PL) results for NCs purified in air using the ethanol/methanol mixtures (what we will refer to as the "aggressive" cleaning method) or ethanol only are shown in Figure 3.4. The general behavior for the absorption spectra show an initial absorbance peak owing to energy quantization followed by continual increase in absorbance at shorter wavelength or higher energies. The PL spectra show only a single PL peak with no broad emission at higher wavelength or lower energies. For smaller NCs there is often a broad defect band at lower energies due to surface trap states [60]. After multiple purification steps, no obvious shifts in absorption nor band edge emission are observed, suggesting that no surface etching occurs during purification. We do note that there appears to be some increase in absorption at lower energies with increasing washes, which could be a result of either surface state absorption or an increase in

scattering due to colloidal instability. Importantly, however, no defect emission emerges as a result of purification. The lack of a defect emission suggests that either surface trap states are not forming after each purification or the surface traps do not introduce a defect emission. Both sets of samples exhibit similar optical properties with a first exciton absorption peak at 595 nm and PL peak at 605 nm. Using equation 3.1, the approximate size of the NCs are 3.9 nm, which we will refer to as 4.0 nm.

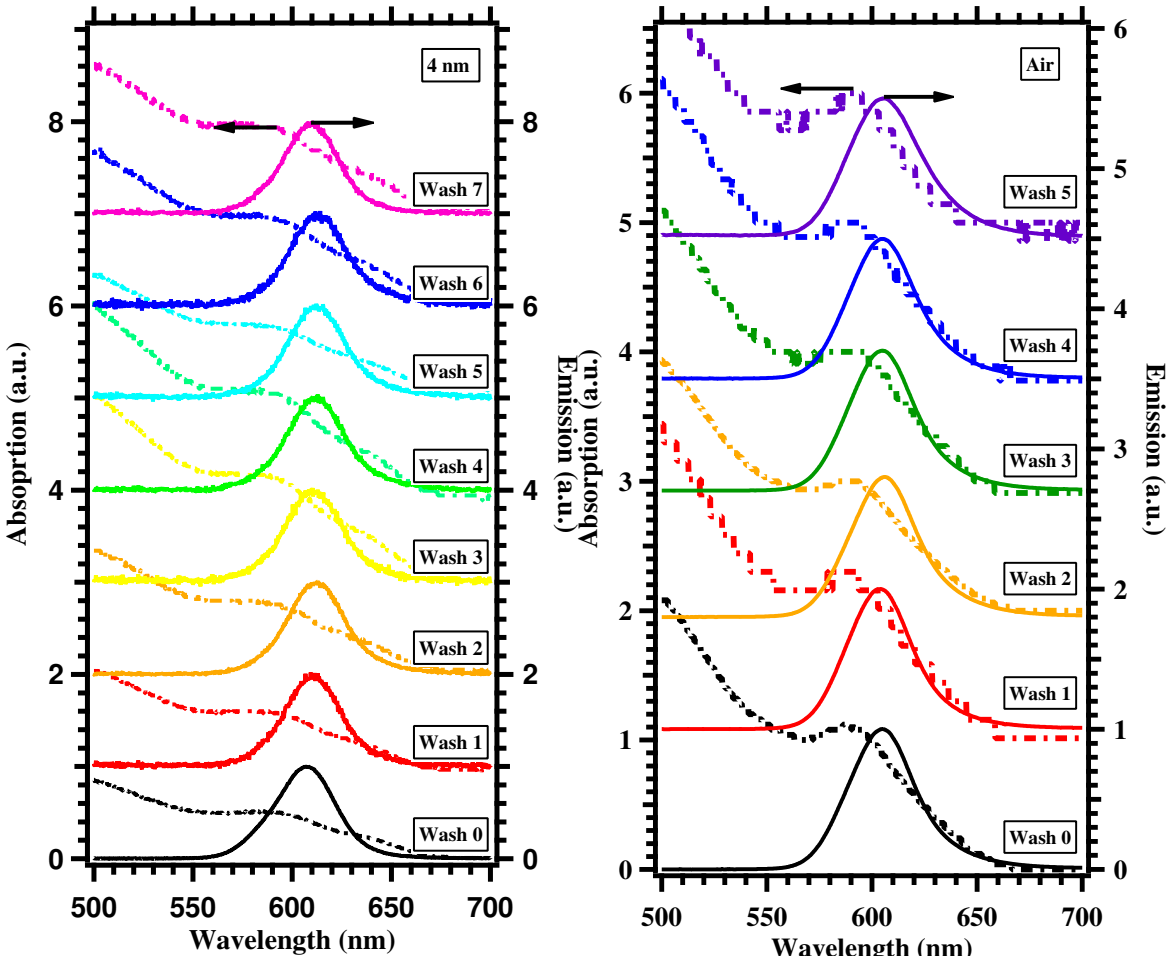

Figure 3.4: UV-vis (dotted) and PL (solid) spectra as a function of purification steps for 4 nm CdSe NCs for (left) ethanol/methanol and (right) ethanol only.

The x-ray diffraction (XRD) patterns for the NCs purified using the ethanol/methanol mix or ethanol only both exhibited the hexagonal wurtzite structure (Figure 3.5), similar to XRD patterns reported in the literature [47, 57, 60]. The main peaks ([100], [002], and [101]) were indistinguishable from one another due to peak broadening while the Bragg

peaks for the [110], [103], and [112] crystal planes are readily observed. After the sequential purification procedures, no significant changes to the crystal structure are noticeable. Changes in intensity are a result of CdSe oxidizing when left in air [37, 68]. From the Scherrer equation (equation 2.2), the NCs purified with ethanol/methanol or ethanol only are approximately 4 nm in size for $2\theta = 45°$ which is in good agreement with NC sizes estimated from the absorption results.

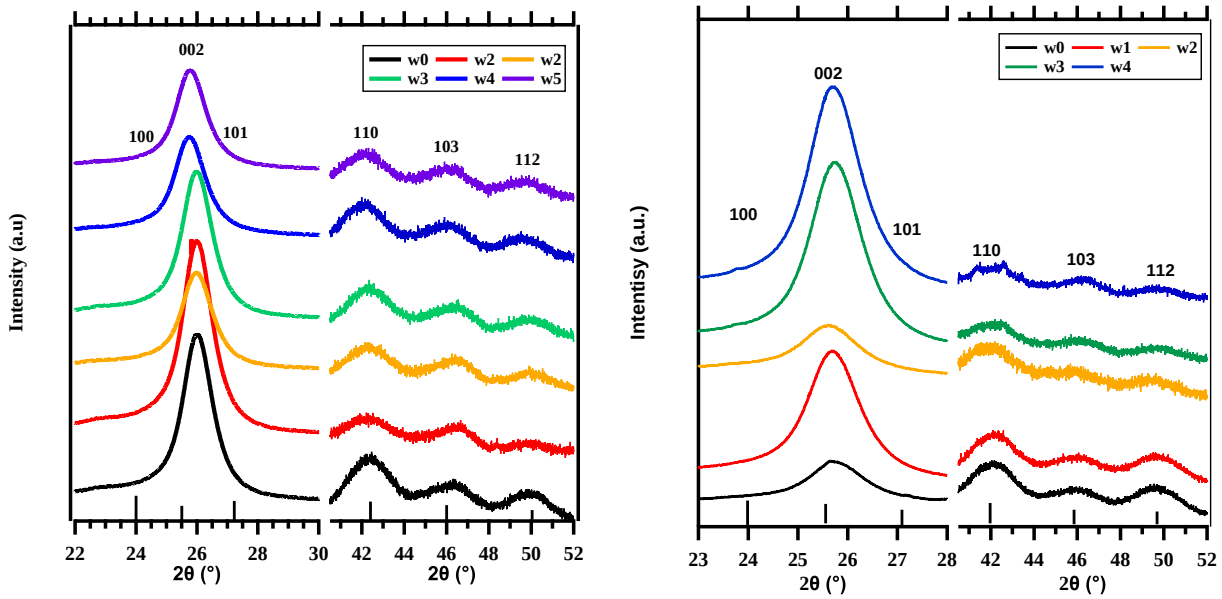

Figure 3.5: XRD patterns for CdSe NCs after purifying with an (a) ethanol/methanol mix or (b) ethanol only as the anti-solvent after drying in air.

Survey X-ray photoelectron pectroscopy (XPS) spectra for the CdSe NCs purified in air are displayed in Figure 3.6. A typical XPS spectrum for CdSe exhibits a number of peaks, including Cd $3p$ and $3d$ and Se $3p$ as well as the C $1s$ peak at 285 eV and the O $1s$ peak at 532 eV [67]. These peaks are present for every washing step and the carbon peaks are typically attributed to the organic ligands on the surface of the NCs and adventitious carbon from being exposed to atmospheric conditions while the oxygen peaks are related to oxygen in the TOPO ligand and to oxidized surfaces on the NCs. Fine scans can be taken at specific element edges to ascertain more information about the chemical state of that particular element. Figures 3.7 and 3.8 display the Cd and Se $3d$ peaks as a function of

purification step, and are in general good agreement with respect to CdSe and Se references [27, 82]. The identifying peak for Cd is the $3d$, which appears as a doublet at 410 eV and 405 eV for the $3d_{3/2}$ and $3d_{5/2}$ peaks, respectively [67]. The full width half max (FWHM) of the Cd peaks is approximately 2.0 ± 0.2 eV for each purification step. The consistent FWHM with increasing purifications suggest minimal oxidation of the Cd atoms to form CdO. The Se $3d$ peak appears at 55 eV and 54 eV for the $3d_{3/2}$ and $3d_{5/2}$ respectively [67]. The two identifying Se peaks overlap forming a single, broad peak centered around 54.5 eV. A third Se peak around 59 eV is associated with the formation of SeO_2 [82]. For both ethanol/methanol and ethanol only cleaning, an increase in the peak at 59 eV associated with SeO_2 is observed with increasing purification step, which suggests that excessive cleaning and exposure to air leads to oxidation of the particle surface.

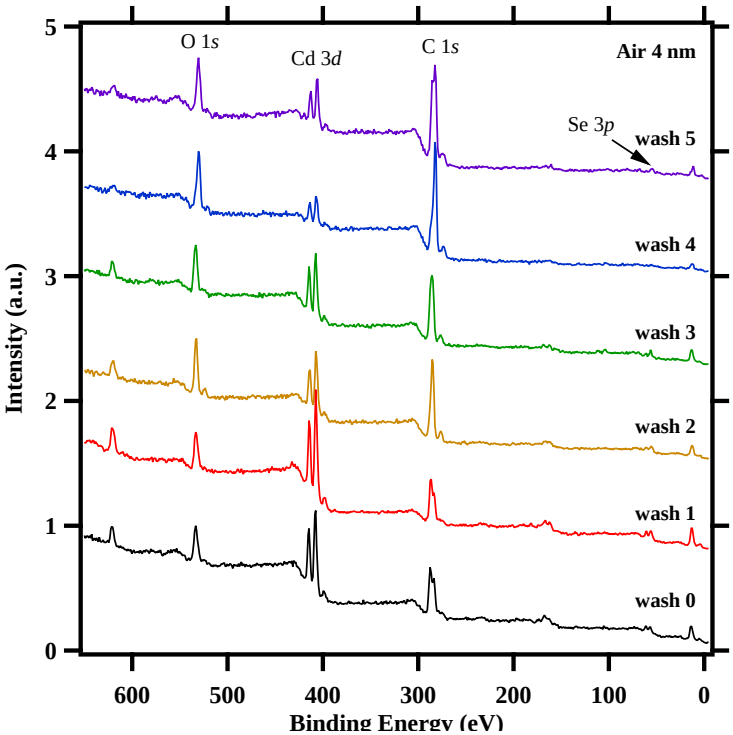

Figure 3.6: Broad XPS spectrum of 4 nm CdSe NCs washed using ethanol/methanol mix and dried in air. Broad spectrum includes expected Cd, Se, O, and C peaks. The vertical lines mark the locations of the Bragg peaks with relative and vary in magnitude relative to bulk xrd database []

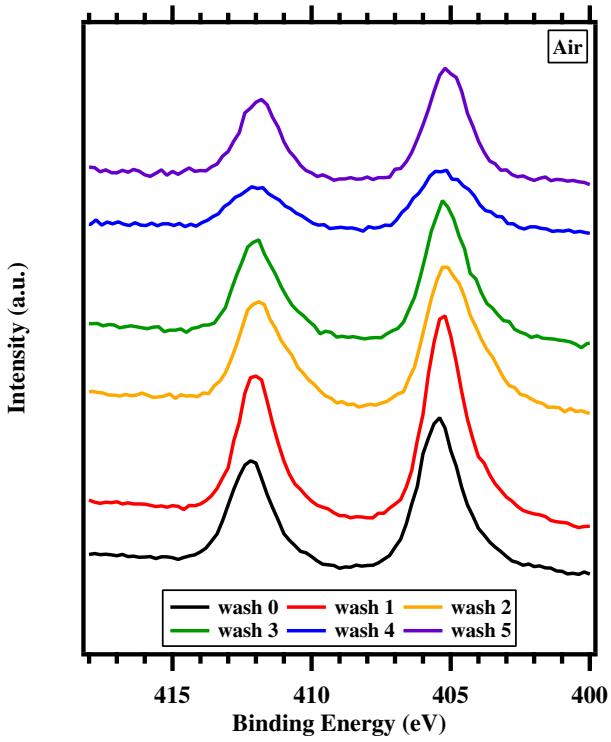

Figure 3.7: Cd $3d_{1/2}$ and $3d_{3/2}$ XPS spectra for CdSe dried in air for ethanol only.

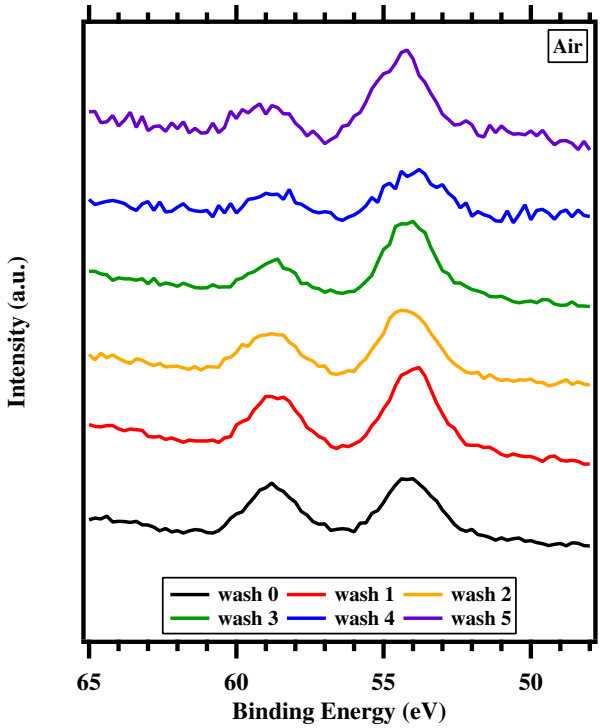

Figure 3.8: Se $3d_{3/2}$ and $3d_{5/2}$ XPS spectra for CdSe dried in air for ethanol only.

3.4 Magnetic Properties of CdSe Nanocrystals post purification

3.4.1 Magnetic properties of CdSe nanocrystals purified in ethanol/methanol mixtures

Although we have shown that the choice of anti-solvent during the purification process does not drastically alter the structural properties of the NCs, prior work by our group and others suggest that the anti-solvent can affect the degree of ligand coverage on the surface of the NC [57, 63]. The removal of ligands leads to a reduction of the surface coordination and promotes the formation of dangling bonds as illustrated in Figure 3.9. These dangling bonds can be a source of electron spin and could result in a net moment. By using an ethanol/methanol mixture during the purification process, more surface ligands can be removed than when using ethanol only [57]. The potential side effect of incorporating methanol is the possibility of etching the surface of CdSe NCs, as methanol has been shown to remove surface atoms [57]. By utilizing a combination of ethanol and methanol, we can slow the etching process, as observed from the consistent FWHM of the XRD for the 4.0 nm NCs (Figure 3.5) and lack of shifting of the exciton absorption and band edge PL peak positions. We begin by examining the effects of dangling bonds for two different sets of CdSe NCs, a 4.0 nm and 8.0 nm series.

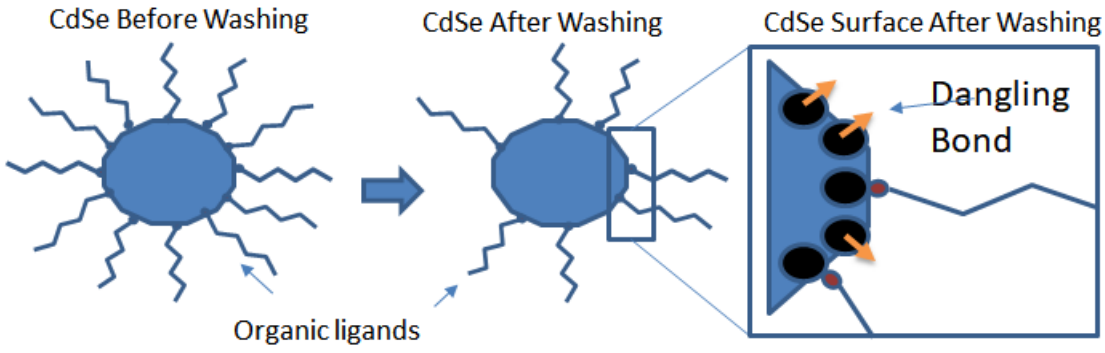

Figure 3.9: Purification process of CdSe NCs using an anti-solvent to wash/ purify the NC surface of organic ligands. Post synthesis the surface of the NC surface is covered with organic ligands. After purifying, the NCs lose organic ligands exposing unbound electrons (dangling bonds)

Figure 3.10 plots the isothermal magnetization curves ($T = 2$ K) for 4.0 nm (Figure 3.10a) and 8 nm (Figure 3.10 b) CdSe NCs. Irrespective of washing step, all NCs exhibit magnetic ordering and saturate or approach a maximum magnetization for values $\mu_o H > 5$ T. For clarity the magnetization saturation values, M_s, are plotted as a function of purification step (Figure 3.11). The 4.0 nm CdSe NCs, M_s exhibit an initial increase in M_s that is about twice the value of the wash 0 sample. The M_s values exhibits a spike in M_s value at wash 4 to 60×10^{-3} emu/g before decreasing to 15×10^{-3} emu/g, very similar in value to the NCs washed one time (wash 1). The 8.0 nm CdSe NCs exhibit similar increases in M_s to the 4.0 nm NCs after the first purification step, but exhibit oscillatory behavior as washes greater than 1. In either case, both samples show enhanced M_s values after the first purification step, suggesting that after the first step the number of dangling bonds increases.

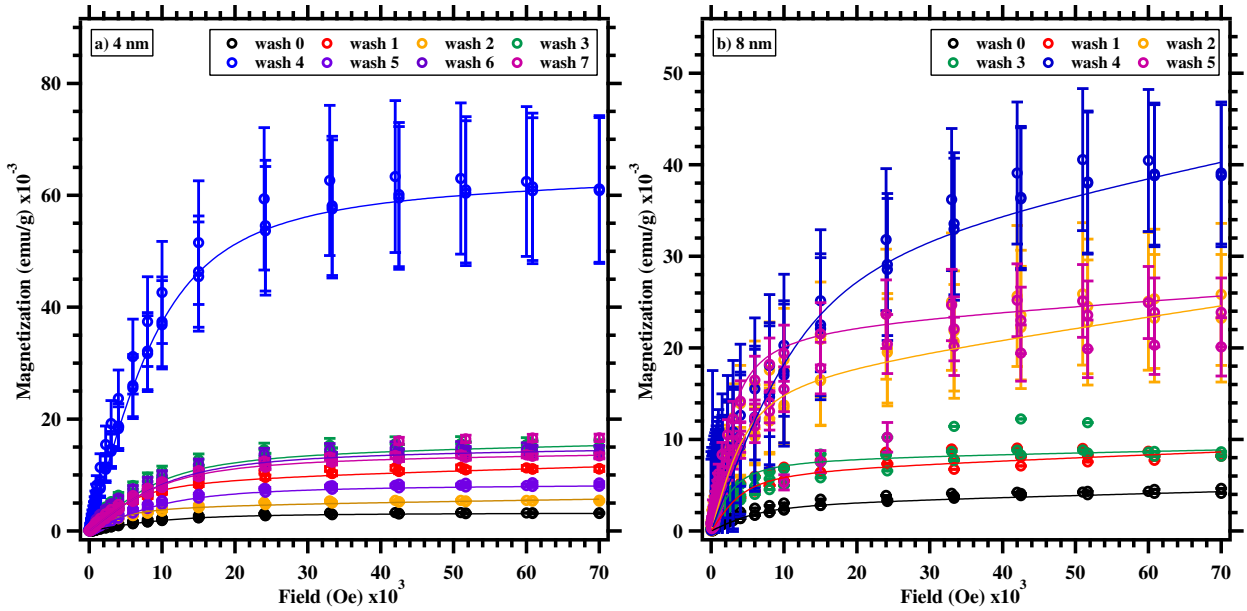

Figure 3.10: Isothermal magnetization performed at 2 K for CdSe NCs purified using ethanol/methanol as anti-solvents for (a) 4 nm and (b) 8 nm NCs. The solid lines are fitted to the magnetization results using the Brillouin function (Equation 2.5).

An interesting observation is the similarity of the values for M_s although the particle sizes vary by a factor of two. The implications associated with this observation suggest the ability to engineer two different particle sizes with similar magnetic properties which

exhibit two distinctly different emission energies. In the in the realm of multi-functional NCs for biomedical applications, this could prove useful for developing a magnetic cellular label with a specific material that is easily distinguishable another another due to an inherent property (i.e. PL).

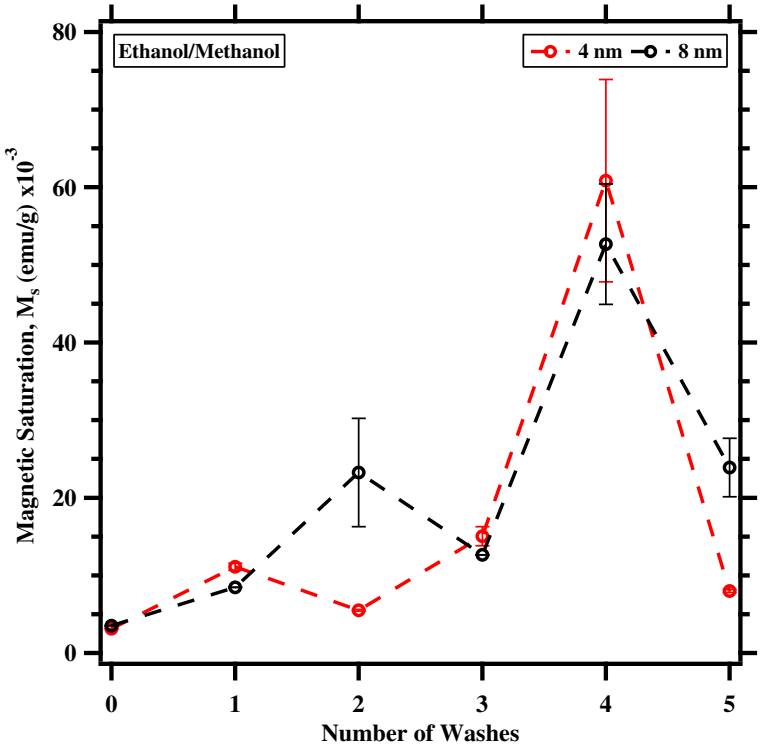

Figure 3.11: Magnetization saturation values, M_s, for 4 nm (red) and 8 nm (black) CdSe NCs purified using an ethanol/methanol mix and dried in air

By fitting the M(H) curves to the Brillouin function (Equation 2.5), we extract the number of magnetic ions, N, in the system (Figure 3.12). In general, the number of magnetic ions generally increases after the wash 0 sample in both the 4.0 nm and 8.0 nm CdSe NCs and reaches a maximum after four washes (wash 4). This alone would suggest that at wash 4, the NCs have reached a maximum number of magnetic ions or dangling bonds, but in combination with the results from the M_s results we see a similar feature, where at wash 4 the maximum value for M_s is achieved. The oscillations or fluctuations in M_s and N are significant as we'd expect a purely dangling bond magnetism mechanism to result in a step-wise increase in M_s and N after each successive wash.

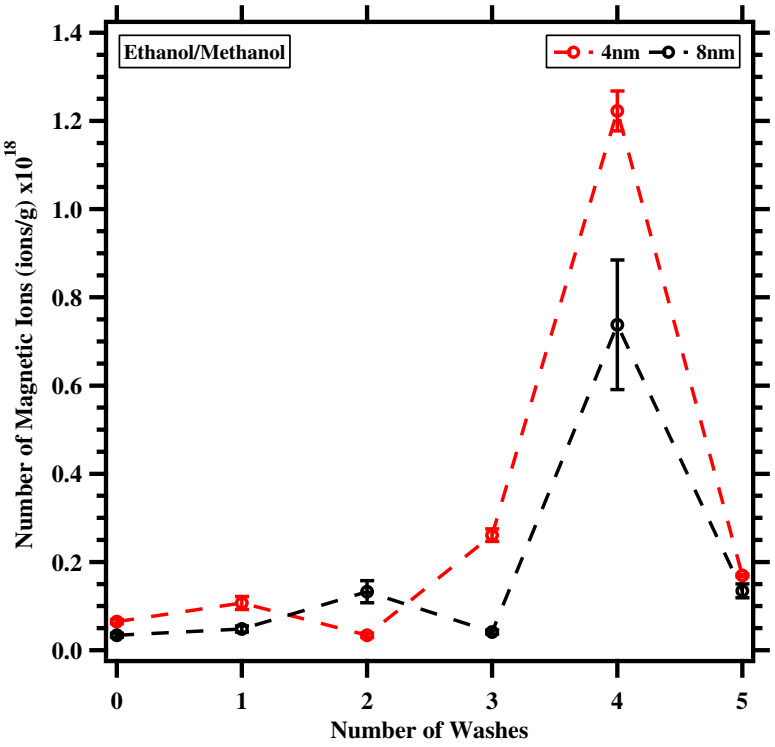

Figure 3.12: The number of magnetic "ions" from fitting to a Brillouin function (equation 2.5) for NCs washed with ethanol/methanol mix for 4 nm (red) and 8 nm (black) size NCs.

From the Brillouin fits (equation 2.5), for the 4.0 nm CdSe NC wash 0 samples we calculate values for the total angular momentum to be $J = 3$ which increases to a maximum $J = 6.5$ by wash 2 and decreases a consistent value of $J = 3$ for subsequent purification steps. The convergence to a $J = 3$ value suggests that the magnetic order is likely due to a similar, but competing mechanism from purely dangling bonds. Until now, I have assumed the dangling bonds are solely from the Cd sites. If we assume a pure dangling bond mechanism, the J value can be treated as a free $1s^1$ electron [51] with $J = 0.5$. It is obvious then, that for $J > 0.5$ suggests a magnetic mechanism beyond a simple dangling bond argument for both the 4.0 nm and 8.0 nm CdSe NCs.

The J values for the 8.0 nm CdSe NC do not converge at $J = 3$ as observed for the 4.0 nm CdSe NCs, but instead oscillate around $J = 7$. This oscillation suggests that the mechanism is changing after each wash. By simply purifying or cleaning the NCs, changes to the paramagnetic properties occur while the small changes in J suggest that the

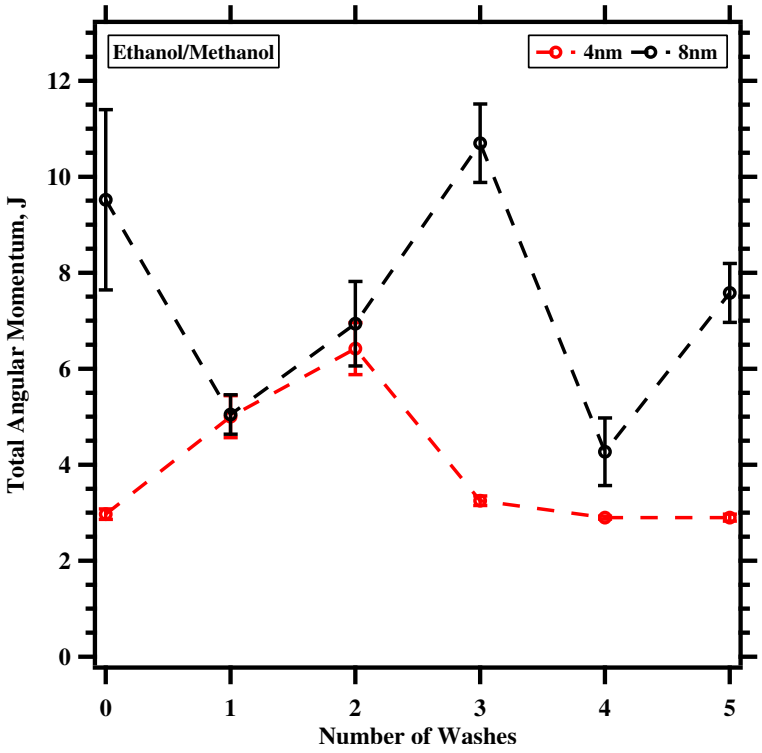

Figure 3.13: Total angular momentum,J , values for CdSe NCs washed with an ethanol/methanol mix and dried in air

underlining magnetic mechanism consistently varies, and cannot simply be ascribed to a dangling bond effect as discussed previously with the 4.0 nm NCs. Therefore, we expect that competing magnetic mechanisms (*i.e.* sum of at least two distinct spin angular momenta) may be responsible for the "spikes" present in the M_s values.

A possible competing factor to the magnetic properties is oxidation of the NC. Upon aggressive purification of the NCs, the lack of a significant amount of organic ligands could render the NCs susceptible to oxidation (as observed from the XPS results). The initial increase in M_s followed by the constant M_s suggests that the mechanism follows the oxidation model described in figure 3.14. For an ideal NC, the synthesized crystal begins with a surface that is "saturated" , thought maybe not 100% completely covered, with organic ligands. After the first purification some ligands are removed exposing dangling bonds. By continuing the purification process, more ligands are removed to expose more dangling bonds. The M_s values for the 8.0 nm NCs do not converge, unlike the 4.0 nm NCs

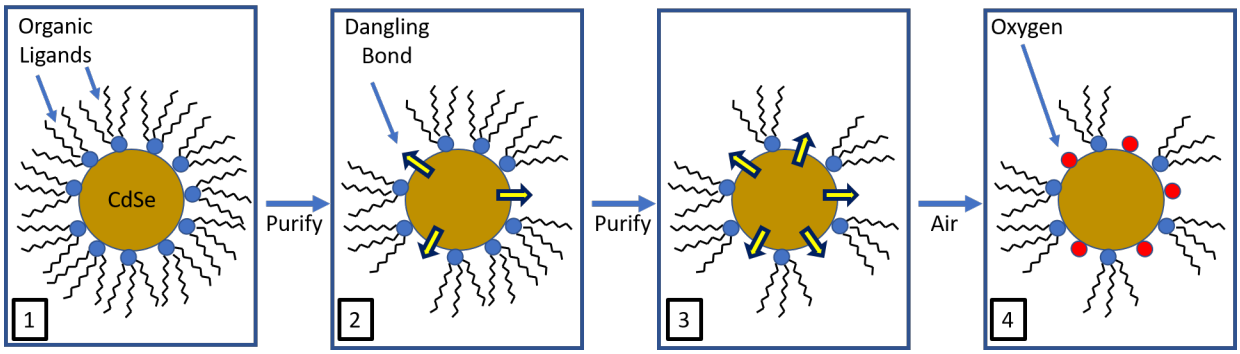

Figure 3.14: Model of how CdSe NCs transition from passivated NCs to oxidized NCs through multiple purification steps. Panel 1: illustrates an ideal NC passivated with organic ligands. Panel 2: After purification some ligands are removed exposing dangling bonds. Panel 3: After further purification more ligands are removed, exposing even more dangling bonds. Panel 4: While exposed to air oxygen bonds to dangling bonds the surface

samples. There are a number of possible reason to expect differences between the 4.0 and 8.0 nm CdSe magnetic behavior, with a simple observation that the surface area of the 8.0 nm NCs is 4X larger than the 4.0 nm. We'd expect, therefore, the number of purification steps needed to induce certain properties to depend strongly on particle size. For instance, if the number of purification steps for the 8.0 nm NCs were to exceed wash 5, we may expect the M_s values could reach a constant value due to a saturation of oxidized surface atoms. Unfortunately this proves difficult to do in practice, as the loss of material during each purification step leads to very small amount of material in later purification steps. To tackle the problem from a reverse vantage point, we explore more gentle methods of NC purification using ethanol only, which can help limit the rate of surface oxidation, as the antisolvent to remove surface ligands.

3.4.2 Magnetic properties of CdSe nanocrystals purified in ethanol only

Our group has previously shown that purification of CdSe NCs with ethanol only is enough to remove the organics on the NC surface [57]. After washing the NCs with ethanol, some of the bound organic ligands are removed which lead to unbound electrons. We hypothesize that using ethanol only during the purification process can successfully remove organic ligands which lead to dangling bonds (i.e. a source of magnetism), but due

to the less aggressive nature of the process, the NC surface will not undergo as rapid of oxidation and thus the only magnetic mechanism will be dangling bonds.

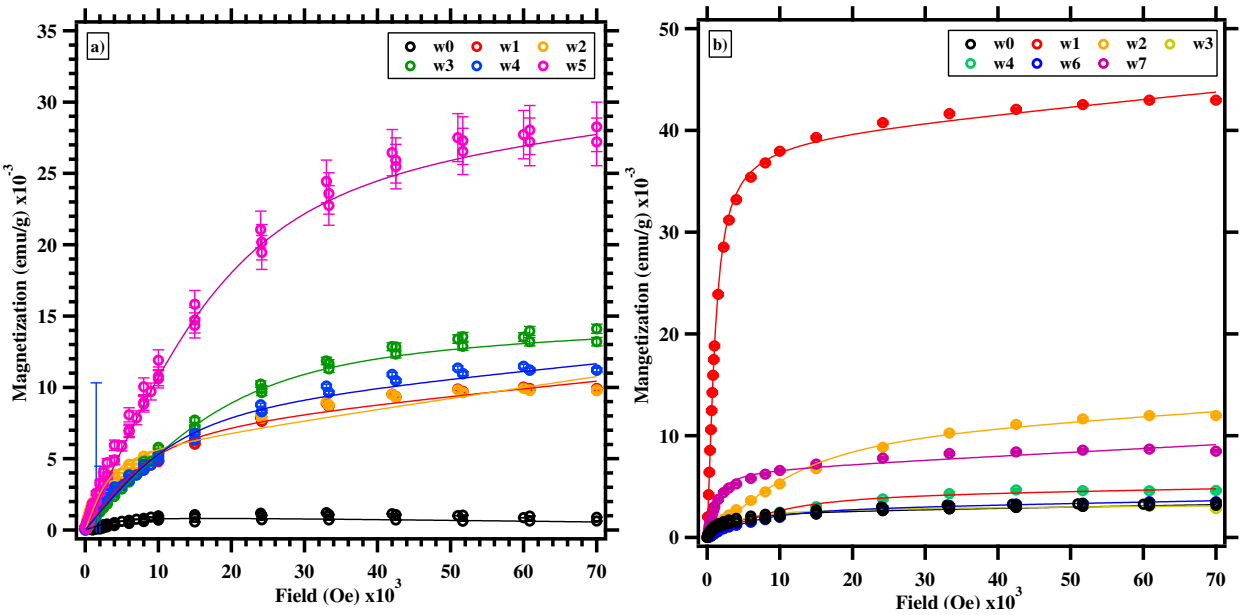

Figure 3.15: The first leg of the isothermal magnetization curves (T=2 K) for (a) 4.0 nm and (b) and 6.0 nm CdSe NCs purified using only ethanol.

Isothermal magnetization (T= 2 K) for both 4.0 nm (Figure 3.15a) and 6.0 nm (Figure 3.15b) CdSe NCs suggests magnetic saturation at all stages of the purification process. The "wash 0" samples for the 4.0 nm CdSe NCs (Figure 3.22) exhibit magnetic saturation values similar to reports by Singh *et. al.* for undoped CdSe nanorods [5]. These NCs exhibited an increase in the magnetic saturation from 0.64×10^{-3} to 9.2×10^{-3} emu/g after 1 wash, an increase of ~15 times the wash 0 sample. The following three washes do not result in a drastic increase in M_s, but the final purification reaches a maximum of 25.5×10^{-3} emu/g, more than doubling in value after the first purification. The increase in M_s generally follows the model of dangling bonds, though not monotonically increasing after each purification step.

To gain further insight, we examined the field cooled (FC) magnetic susceptibility, χ(T), of the 4.0 nm CdSe prepared in air (Figure 3.17) which exhibits a strong temperature dependence below 10 K. The strong temperature dependence is commonly

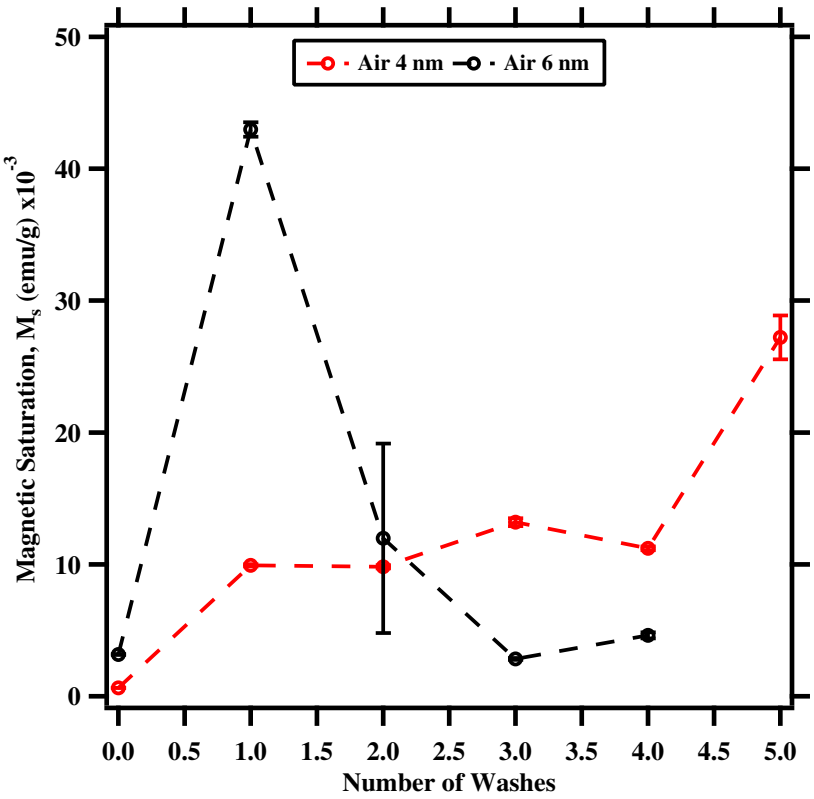

Figure 3.16: Magnetization saturation values, M_s, for 4 nm (red) and 6 nm (black) CdSe NCs purified using an ethanol only and dried in air

referred to as a Curie tail and is likely due to the ordering of dangling bonds [83, 84]. Above 20 K, the susceptibility slowly varies with temperature consistent with a paramagnetic Curie law ($\chi = C/T$). In some of the plots there is a "bump" or peak around $T = 50$ K, which can be attributed to oxygen present in the sample. Though the sample chamber operates at low vacuum pressures, oxygen can be trapped in the sample holder during the sample preparation process. Generally, we observe no differences between the FC and ZFC (not shown) susceptibility scans which is different from the behavior expected typical superparamagnetic NCs like iron oxide [14], suggesting species such as iron oxide are not sources of magnetic impurities [85, 86].

The temperature dependent magnetic susceptibility results (Figure 3.17) are fitted to a modified Curie-Weiss law (Equation 2.7) suggesting paramagnetic behavior at low temperatures (T $<$ 10 K). Ideally, paramagnetic materials will exhibit positive magnetic

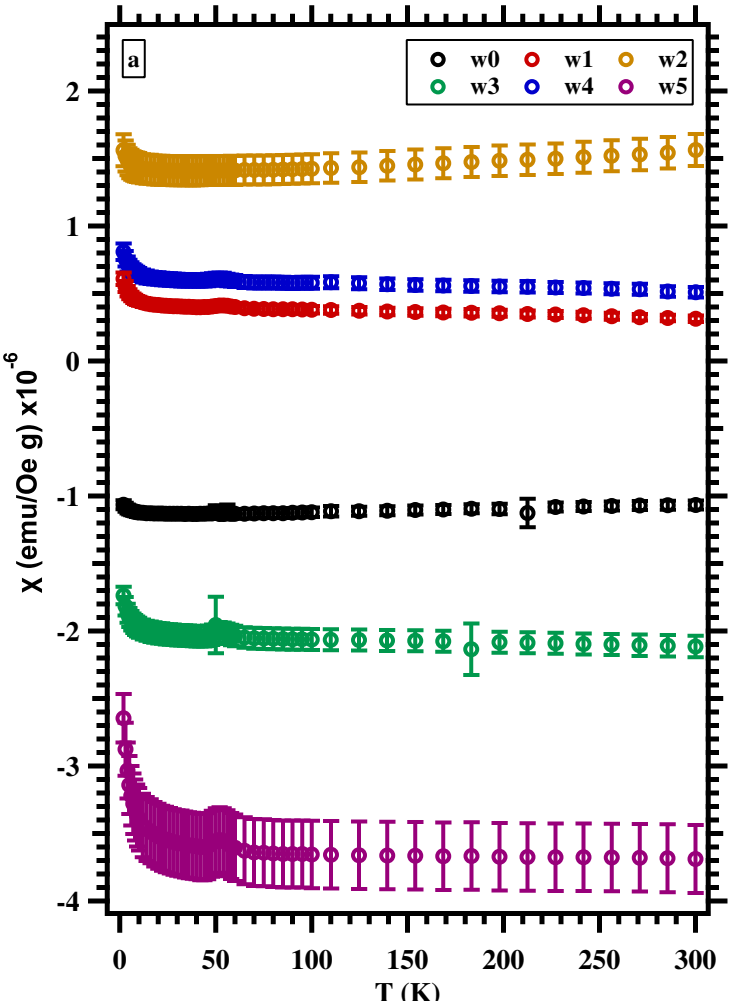

Figure 3.17: Magnetic susceptibility for air dried 4.0 nm CdSe NCs as a function of temperature.

susceptibility values, χ, while a negative χ value is typically associated with a diamagnetic response. Though the χ responses are shown as negative values, this does not automatically suggest that the NCs are diamagnetic. The reason for the negative magnetic signal is likely due to a combination of competing diamagnetic signals from the sample holder and the organic ligands on the NCs. The large increase in susceptibility or Curie tail at low temperatures are suggestive of dangling bonds aligning at low temperatures.

For the 6.0 nm CdSe NCs, after the first purification step, we observe a similar increase in M_s a previously seen, where the initial M_s increased from 3.2×10^{-3} to 43×10^{-3} emu/g, an increase of $\sim$13 times the unwashed NCs. Unlike the 4.0 nm NCs, however, the

subsequent washes exhibit decreases in M_s and oscillate around 5×10^{-3} emu/g, which are values similar to the unwashed sample (3.2×10^{-3} emu/g). While the M_s values appear tunable by varying the number of purification steps, the two sizes of CdSe NCs show different trends in M_s with purification step. The 4.0 nm NCs show a continual increase in M_s as the number of washes increased suggesting an increase in the number of dangling bonds as more ligands are removed. The 6.0 nm NCs, however, do not show evidence for this quasi-linear increase in M_s, and is strongly reminiscent of the behavior observed for the ethanol/methanol mixtures which suggest that surface oxidation [37, 68] may pose a problem in cases even when purifying with ethanol only.

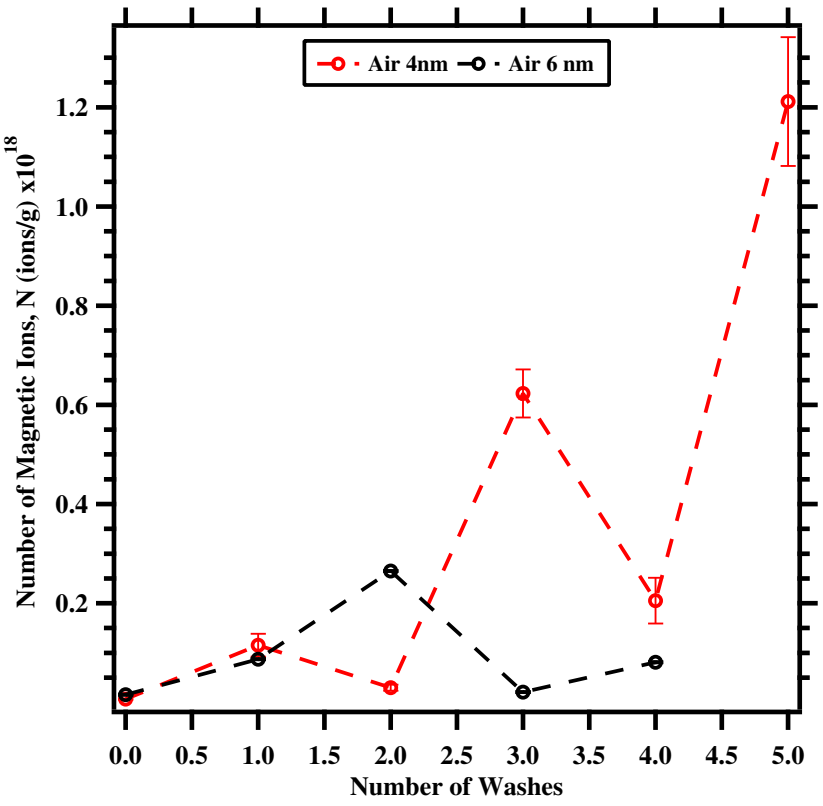

Figure 3.18: Number of magnetic "ions", N, for for 4 nm (red) and 6 nm (black) CdSe NCs purified using an ethanol only and dried in air

To better understand the discrepancies, the magnetization curves are fitted to a Brillouin function (Equation 2.5) to extract the number of magnetic "ions", N. The number of magnetic "ions" (Figure 3.18) for the 6.0 nm CdSe NCs show that the number of

"ions" increases to a maximum at wash 2 before decreasing. We propose that the number of dangling bonds increases after the first couple of washes resulting in an increase in M_s but after the maximum M_s step, the dangling bonds on the surface become passivated thus reducing the M_s value. The dangling bonds are likely passivated with oxygen as a result of drying the NCs in air. While drying in air, the the dangling bonds bond with oxygen forming SeO_2, which would be more likely in the latter purification because there should be a larger density of dangling bonds on the surface, leading to easier oxidation [37, 66]. While there have been no reports on the magnetic properties of pure SeO_2 nanoparticles, work from Sundaresan et al [14] and Coey et al [46] suggest that oxide nanoparticles may have an inherent ferromagnetic nature. The mechanism behind the increase in magnetic saturation is likely due to unpaired spins as a result of oxidation and whole the exact mechanism is still under debate in these types of materials, most researcher agree that the likely culprit behind ferromagnetism in oxide materials is oxygen vacancies. We expect, therefore, that surface oxidation of the CdSe particle could result in new magnetic properties, similar to the work reported in the oxide literature. We note, however, that any observed magnetic properties should be much weaker in the CdSe system versus the pure oxide system, as the oxide later is confined to the surface layer of CdSe. We hypothesize therefore that many of our observed magnetic phenomena, while initially started via a dangling bond mechanism, can be attributed to oxidation of the CdSe surface. An oxide layer could explain why Curie constant values for the 4.0 nm NCs dried in air are fairly constant values, and are not monotonically changing due to increase in dangling bond concentration.

For the 4.0 nm CdSe NCs, the number of magnetic "ions" generally increase after each of the purification steps. The increase of N with each purification is also consistent with the M_s trend for the 4.0 nm NCs dried in air (figure 3.18), except it appears that the number of "ions' is oscillating while increasing. Upon further inspection of M_s, those values also oscillate, though not as drastically as the values of N. Interestingly, upon closer inspection there are small oscillations in M_s and N for the 6.0 nm NCs as well. The oxidation process

should be quick, meaning that any dangling bonds present would be passivated upon exposure to air within 48 hrs [68]. This would imply that the magnetization values should eventually plateau as the number of dangling bonds would effectively remain constant.

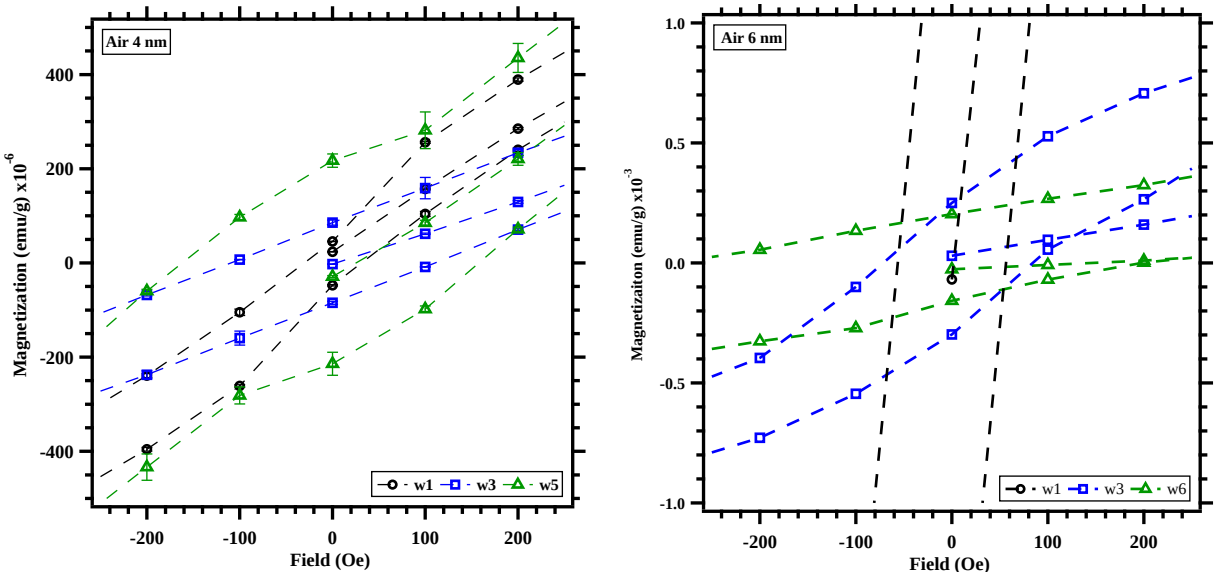

Figure 3.19: Hysteresis loops of 4 nm (left) and 6 nm (right) CdSe NCs washed using ethanol only. Only select washes are plotted for clarity.

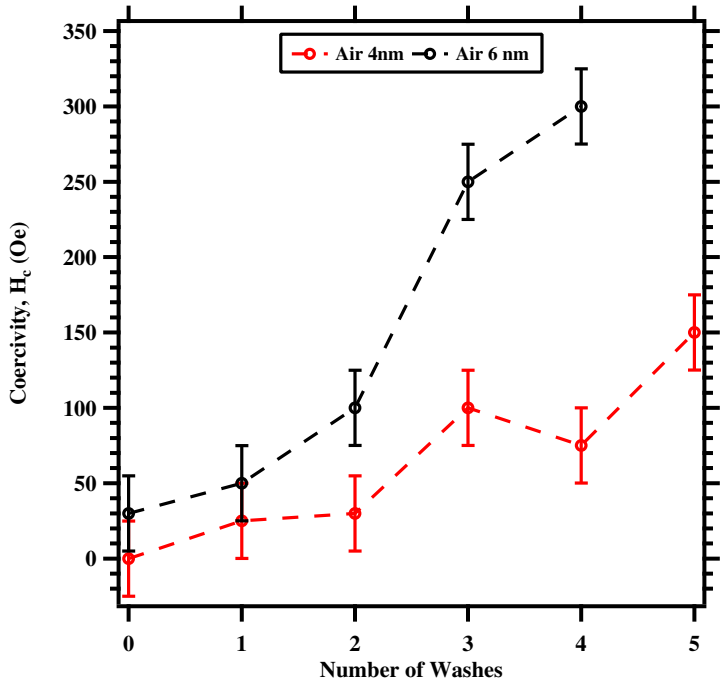

Figure 3.20: Coercivity, H_c, for 4 nm (red) and 6 nm (black) CdSe NCs purified using an ethanol only and dried in air.

At 2 K, the NCs exhibit ferromagnteic hysteresis at low fields (Figure 3.19). Interestingly, at 2 K, the NCs exhibit a transition from a paramagnet to a soft ferromagnet (Figure 3.20). The coercivity of the NCs begins ∼40 Oe and continually increases to a maximum of 150 Oe and 280 Oe for 4 nm and 6 nm samples. Unfortunately this is not practical in spintronics where device temperatures are usually above room temperature [87] and at 300 K all NCs behave as weak paramagnets (not shown). Interestingly, there is a linear trend with H_c as the number of purification increased (Figure 3.20). The results suggest that there is the potential for magnetization tunability for two different size NCs. Though this is exciting news, that is consistent with our results on NCs purified using both the ethanol/methanol mix, this hysteresis can still be a side effect of surface oxidation. The increasing number of NC purifications leads a decrease in surface ligand density which may lead to oxidation of the particle surface.

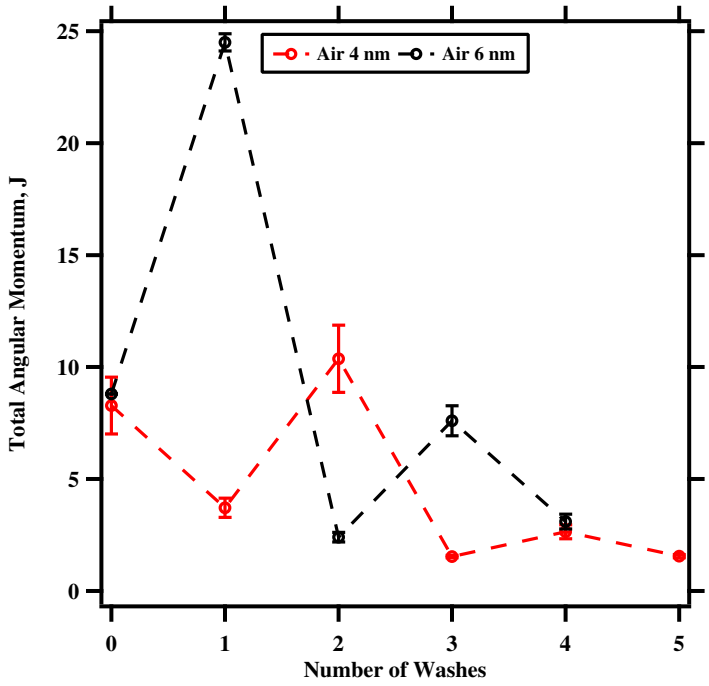

Figure 3.21: Angular momentum value, J, for 4 nm (red) and 6 nm (black) CdSe NCs purified using an ethanol only and dried in air

By fitting to a Brillouin function and extracting the total angular momentum values, J, we can gain insight as to the type of spin mechanism that is associated with the M(H)

curves. The values are more complicated to address, because there could be multiple mechanisms involved or that the spins could randomly aligned and can assume any magnetic ordering ($J \to \infty$). Following Hund's rules [39], we can calculate expected values of J for a particular spin system. For example, if a Cd atom had a missing d electron (d^9), then the total angular momentum quantum number $J = 5/2$. Inspecting figure 3.21, the 4.0 nm CdSe NCs dried in air exhibit a transition from a complex $J = 8$ to $J = 1.5$. I say complex because no one mechanism should have a J larger than $J = 5$ for a s, p, or d orbital which suggests multiple mechanisms must be in play for $J > 5$.. The transition to a $J = 1.5$ system is suggestive of oxygen vacancies, where oxygen vacancies can have $S = 0$ or 1 where two electrons can be aligned parallel or anti-parallel. For a $J = 1.5$ the oxygen vacancy will have two electrons anti-parallel to each other. The transition in J values that suggest oxygen vacancies is consistent with the oxidation of the NC surface suggesting that the primary mechanism for CdSe NCs dried in air is likely due to oxygen vacancies on the surface of the NCs after exposure to air. Another contributor to the magnetic properties could be from unfilled p orbitals localized on O atoms. We note, however, that the various mechanisms should be taken with caution since the J value derived from fits of the M(H) data is an average of many possible mechanisms. The presence of oxygen vacancies does not, however, fully explain the oscillating spikes in the M_s and N values, where the large J values can not represent a single magnetic mechanism. When considering both sets of CdSe NCs prepared using ethanol or an ethanol/methanol mixture as antisolvents, I believe that dangling bonds from an under coordinated surface initially leads to the weak magnetic behavior, but it is also joined in conjunction with another mechanism recurring spikes in M_s, N, and J. In order to examine the true nature of magnetism in these materials, developing methods for preparing the samples in inert atmospheres is crucial.

3.4.3 CdSe Nanocrystals Purified Using Ethanol Only and Dried under Nitrogen

In an attempt to eliminate all oxygen and minimize the amount of surface oxidation, 4.0 nm CdSe NCs were purified and prepared under an inert atmosphere. We expect that purification under N_2 should minimize the exposure to air (*i.e.* O_2) and reduce the oxidation of the NC surface. The expectation is that the magnetic response of the NCs prepared under inert conditions should only reflect the magnetic contribution of a "pristine" NC surface.

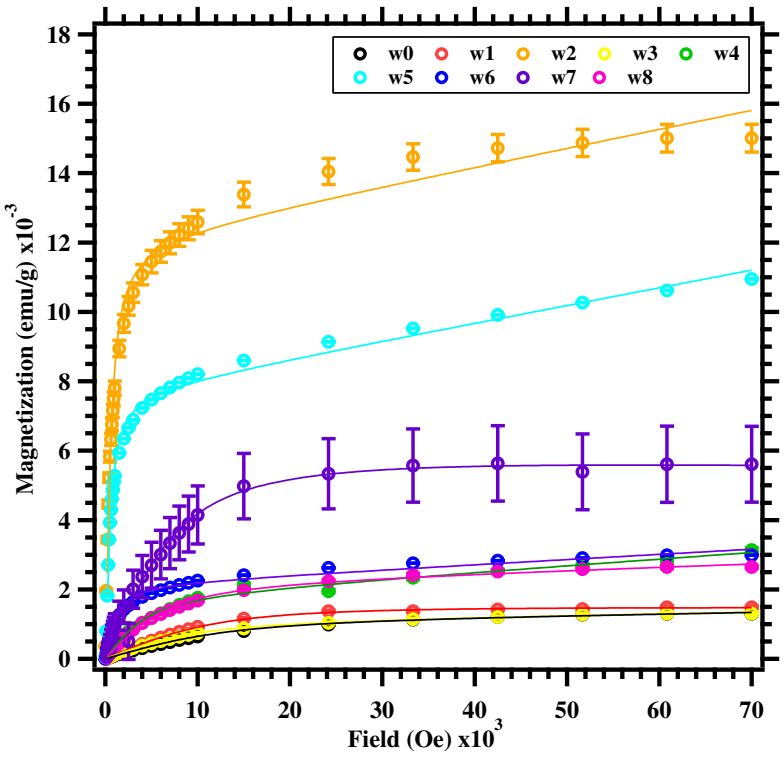

Figure 3.22: The magnetization results for 4 nm CdSe NCs prepared under N_2 atmosphere

The isothermal M(H) curve at 2 K for the N_2 prepared samples (Figure 3.22) exhibit the familiar magnetization curve even before purification. Surprisingly, these NCs do not exhibit a large increase in M_s after the first purification, like in previous cases, but instead exhibits a large increase on wash 2. After the first purification, the M_s value only increases by 10%, but the second purification increases the M_s by 11 times the wash 0 sample

(Figure 3.23 red line). After examining the M_s of the 4.0 nm CdSe NC N_2 dried samples, the M_s shows a more pronounced fluctuation in M_s. The oscillatory behavior, contradicts the notion that increasing more dangling bonds leads to increasing M_s. This suggests that simply removing surface ligands does not correlate to an increase in M_s, and again points to the possibility of a more complex mechanism or mechanisms at work.

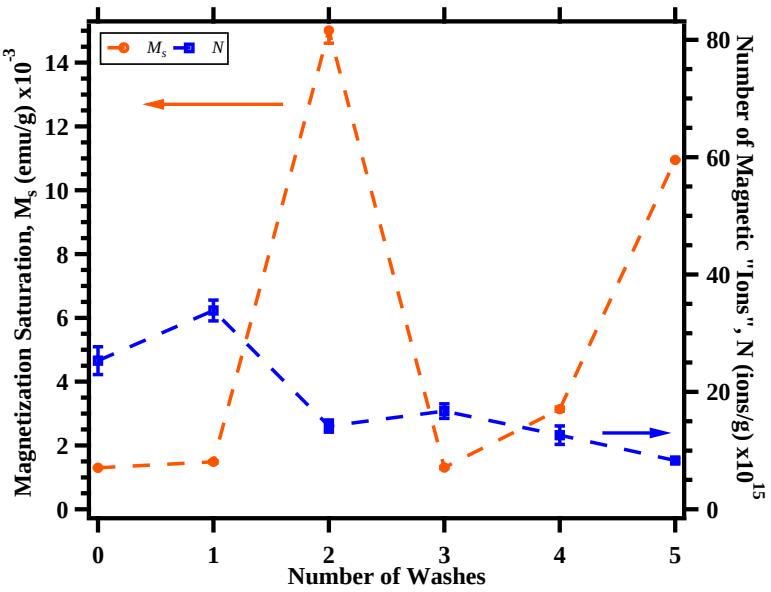

Figure 3.23: Combined magnetic saturation (red), M_s, and Total angular momentum (blue),J , values for NCs washed with ethanol only and dried under a N_2 atmosphere

The CdSe NCs dried under nitrogen have M_s values (Figure 3.23) that follows a similar trend to the 6.0 nm NCs dried in air (Figure 3.16), where there is an initial "peak" or "spike" in M_s. Instead of arriving at a steady M_s value as observed for the 6.0 nm NCs dried in air, however, the M_s values increases again on the last wash step. This is also in contrast to the 4.0 nm NCs dried in air, which continually increase in M_s values during purification. The number of magnetic "ions" (Figure 3.23 blue) decreases after increased purification instead of continually increasing, suggesting that dangling bonds are being lost after more purification. Contrary to our expectations, even after preparing the NCs under an inert atmosphere the number of dangling bonds do not monotonically increase with increasing the number of purifications.

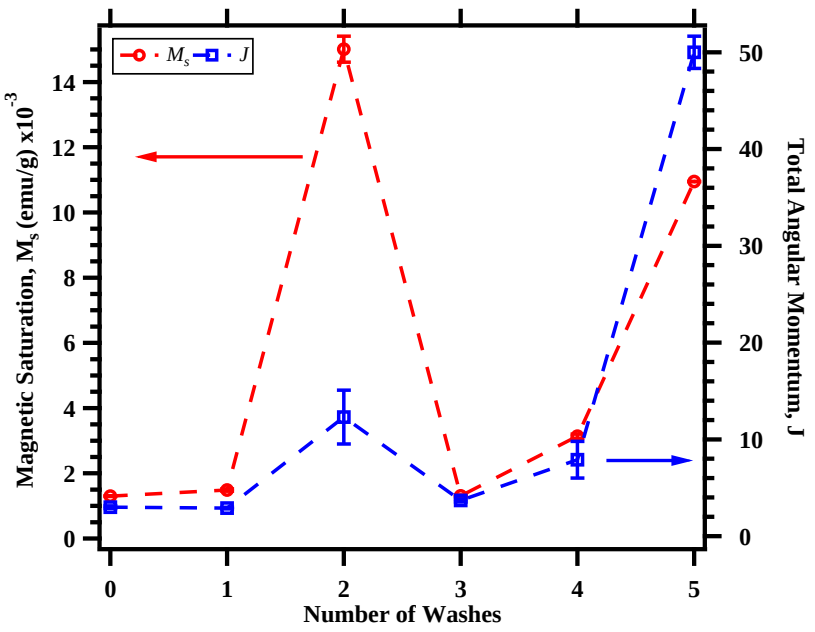

Figure 3.24: Combined magnetic saturation (red), M_s and total angular momentum (blue), J , values for NCs washed with ethanol only and dried under a N_2 atmosphere

Interestingly, the NCs prepared under N_2 exhibit increases in N before decreasing below the N value of the wash 0. This suggests that the NC surface is not oxidizing and can be verified via from XPS (Figure 3.25), specifically by examining Cd and Se $3d$ XPS peaks (Figure 3.26). The XPS data suggest that there is very little oxidation of the CdSe surface via the absence (or minimal intensity) of the SeO_2 photoelectron peak at 59 eV. We have found that under inert conditions the CdSe NCs do not oxidize quickly and can remain oxide "free" for up to 9 months in a glove box filled with N_2. While the absence of surface oxidation is a welcome result, the observations of decreases in N with increasing purification steps become perplexing without an argument for particle oxidation. Although the M_s and N values are not self-consistent, the M_s and J values (Figure 3.24) follow very similar trends, with the "spikes" or "peaks" in M_s appearing consistent with the oscillatory behavior in J. This suggests that while the NCs are purified, the surface of the NC exhibits a combination of spin states where multiple mechanisms emerge to strengthen the M_s values at wash 2 and 5.

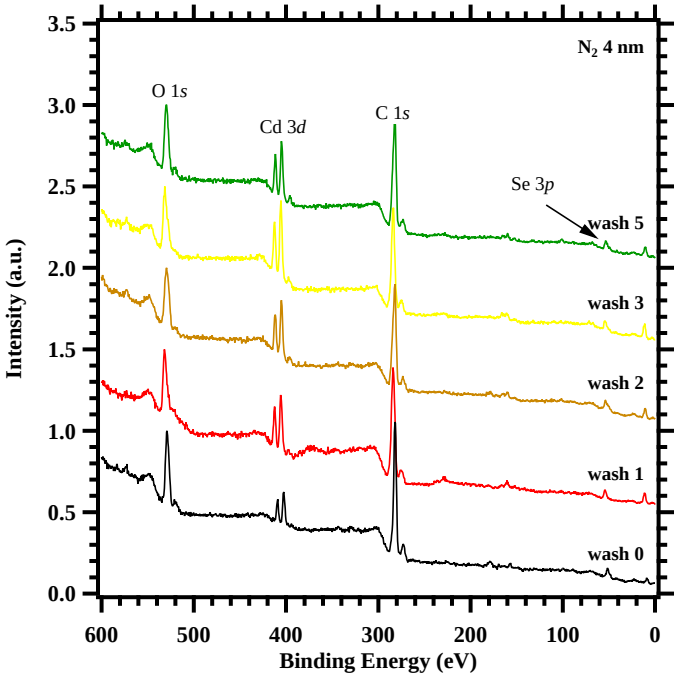

Figure 3.25: XPS spectrum of CdSe NCs dried under N_2 that exhibit a similar broad pattern as CdSe NCs dried in air.

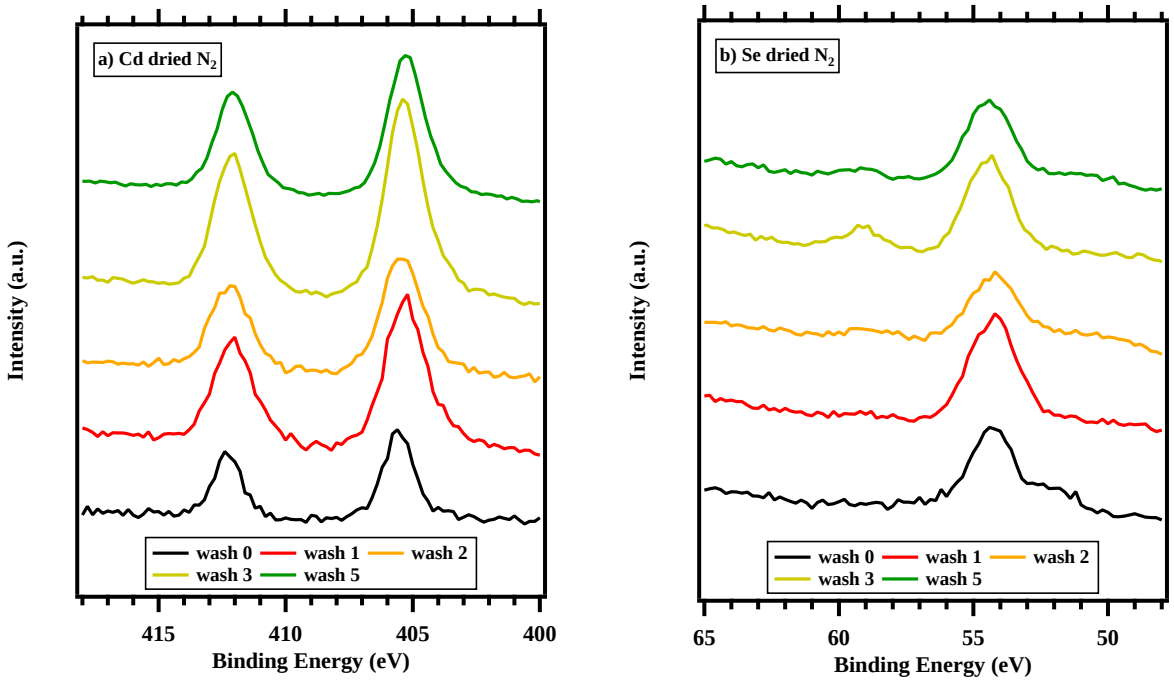

Figure 3.26: (a) Cd 3d and (a) Se 3d XPS spectra for 4.0 nm CdSe dried under N_2.

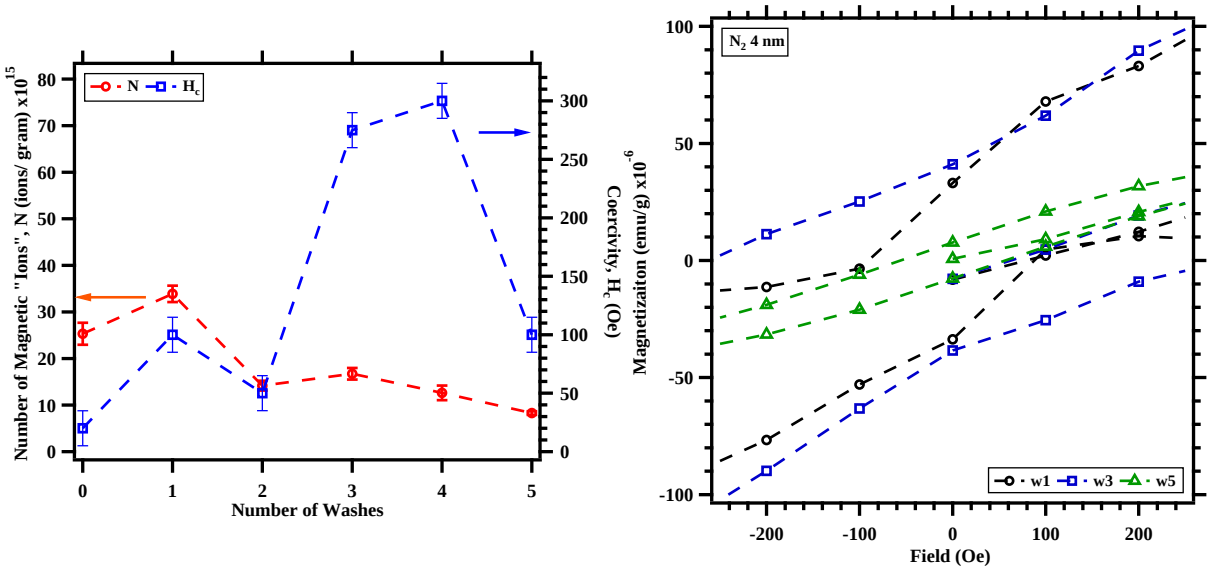

Figure 3.27: Number of magnetic "ions" (red), N, and coercivity (blue), H_c, values for NCs washed with ethanol only and dried under a N_2 atmosphere. (Right) Select, zoomed in view of M(H) curves for CdSe NCs dried under N_2 that exhibits the weak ferromagnetic properties at 2 K.

Coincidentally, N and H_c and values are self-consistent to each other, where increases and decreases in N align with values of H_c. The is expected, because if there are more magnetic sources then the distance between them is smaller, thus allowing for stronger ferromagnetic exchange coupling. The interesting take away, however, is that the positive "spikes" in M_s occur at wash 2 and 5 while the negative "spikes" in N occur at wash 2 and 5 also. This is behavior appears to be contradictory, as we'd expect with *more* magnetic ions (N) we'd observe larger M_s values. This begs the question, to what else can we attribute the bizarre M(H) results? The data suggests that there is a changing or recurring mechanism at various stages of the purification process that appears to switch "on or off" and is not related to oxidation of the surface. In an attempt to help understanding how the particle surface may change upon surface ligand removal, we turn to density functional theory (DFT) calculations to simulate the purification process and possibly provide a plausible mechanism for magnetism in these materials.

3.5 Role of Surface Reconstruction during the purification process

In the DFT simulations, the CdSe cluster is passivated with Cl atoms to simulate the effects of organic ligands. A report from Infante's group [79] has shown that trap states or dangling bonds on the surface of the NCs require a 1:2 excess metal to X-type or L-type ligands to form and it is the removal of Z-type ligands is the likely source for the formation of trap states on the surface of the NCs. Thus, to examine the effects of removing surface ligands, Z-type ligands were removed. In these calculations, a Z-type ligand is comprised of 1 Cd atom and 2 Cl atoms which allows the NC to maintain charge neutrality. Two different methods of ligand removal from the surface were employed: (a) first the removal of a Z-type ligand and then optimizing the structure before removing another Z-type ligand followed by optimization, etc. or (b) remove the desired number of Z-type ligands all at once and then allowing the structure to relax. While the former case is the approach commonly used in most theoretical studies [79], we employed the latter case as that may be representative of how ligands are removed during the actual purification process.

In either case of ligand removal, trap states form inside of the bandgap as show as seen in Figure 3.28b. After the removal of one ligand, a trap state emerges and after the removal of five ligands, we observe the appearance of two midgap states. From the calculation the bandgap of the crystals is about 0.7 eV, however, the bandgap of bulk CdSe is about 1.74 eV (at 300 K) and the difference can be attributed to the fact that DFT-PBE calculations underestimates the bandgap by about 1 eV [79]. The discrete energy levels in the conduction band are typical for DFT-PBE calculations [79] and the different colorings are to show the percentage of atomic orbital contributes per atom to the density of states (DOS). From figure 3.28b, the conduction band is predominantly formed by Cd atoms (blue) while the valence band is dominated by Se atoms (red). Notably, Cl atoms (black), i.e. surface ligands, contribute very little to the DOS. Interestingly after the removal of 2, 3, or 4 Z-type ligands there does not appear to be the emergence of defect states implying

that only under the certain conditions trap states appear. This could be related to the non-equivalency of surface energies for different surface atoms [79].

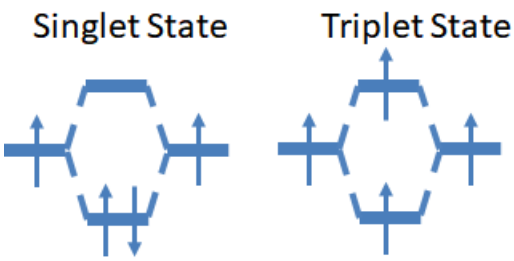

(a) CdSe singlet and triplet states

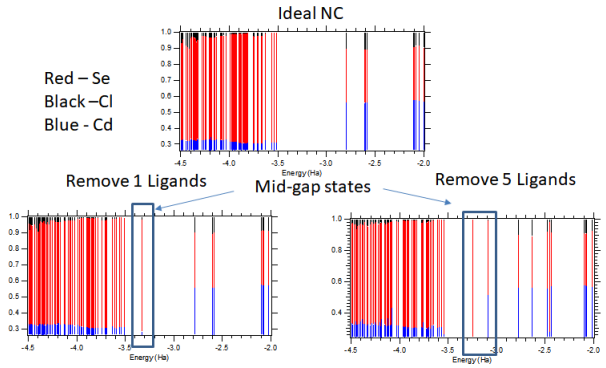

(b) CdSe DOS band diagram

Figure 3.28: Diagram of showing the difference between a two electron singlet and triplet bonding states using a molecular orbital diagram (a). The singlet state refers to bonding where both electrons are in the same energy level while the triplet state refers the scenario where both electrons are in different orbitals. The density of states (DOS) band diagram (b), where the percentages of each atom are colored as follows: blue is Se, red is Cl, and black is Cl.

Upon removal of Z-type ligands, for either ligand removal method, we observe the formation of Se-Se bonds of under-coordinated Se surface atoms via surface reconstruction (Figure 3.29). Visually the formation of a Se-Se bond can be interpreted as Se migrating closer to a near-by, undercoordinated Se atom. The Se-Se reconstruction can be thought of in terms of a simple molecular orbital approach, where we produce bonding/antibonding orbitals that can be populated in a singlet or triplet state (Figure 3.28a). In the singlet state, electrons couple together with opposing spins, resulting in a $J = 0$, suggesting no net magnetic moment is possible. An interesting case could arise, however, if the Se-Se reconstruction was in the triplet state which would result in a net spin and a net magnetic moment. An obvious question, therefore, is asking if the formation of triplet states is energetically favorable.

After energy minimization, examining the difference in total energy will provide evidence for the favorability of either singlet or a triplet state formation. When performing a sequential ligand exchange, in most cases the singlet state is favored, with a very small

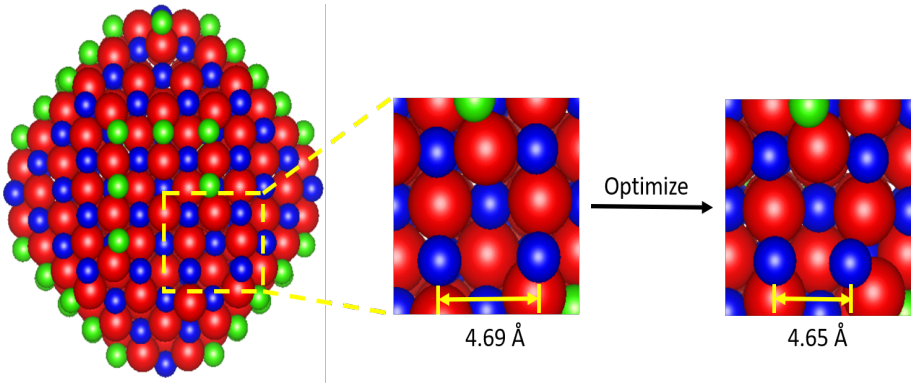

Figure 3.29: CdSe cluster showing Se migration to form Se-Se bond

favorability for triplet formation for the removal of 2 Z-type ligands. When the ligands are abruptly removed, as the number of Z-type ligands removed increase, we observe favorable conditions for triplet state formation. When you consider the both ligand exchange results together, there is evidence for oscillatory behavior towards to formation of the triplet state, which is similar to the oscillatory behavior observed in the M_s values. We speculate that as more ligands are removed, surface reconstruction results in the removal of dangling bonds which either increases or decreases the number of free electrons. As the singlet state is almost always preferred, we observe a reduction in the number of dangling bonds and thus the M_s values. Under certain conditions, however, the reconstructed surface is in the triplet state, which leads to a net moment and an increase in M_s values. These two factors together help produce a plausible model to explain the oscillatory behavior in the magnetization of undoped CdSe NCs prepared under inert conditions.

3.6 Conclusion

To summarize, the prospect of a multi functional CdSe NCs that has both the optical and magnetic properties desirable for applications in biomedicine or magneto-optical applications is exciting. I've shown that the NCs exhibit weak paramagnetic behavior as a result of an dangling bonds resulting from multiple sources from removing surface ligands on CdSe NC surfaces. The exact mechanism of dangling bonds, however, is difficult to

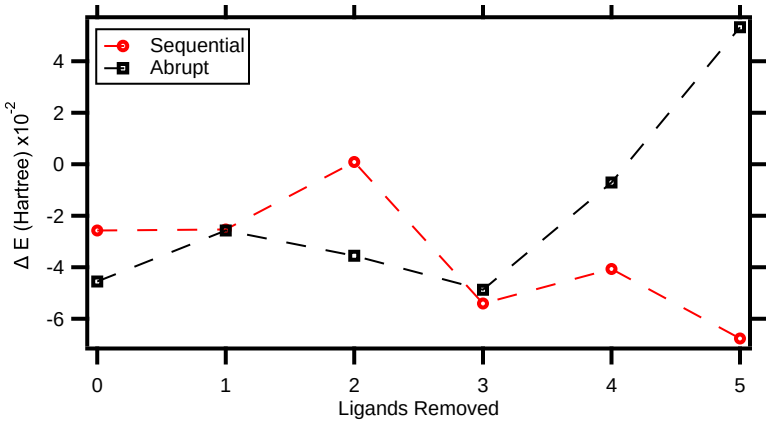

Figure 3.30: CdSe DFT ΔE for the sequential removal (red) and abrupt removal (black) of Z-type ligands

distinguish. The source of magnetism can be a combination of dangling bonds from an under-coordinated surface, an oxide layer, and/or Se-Se reconstruction on the surface the NCs.

CHAPTER 4
SURFACE PURIFICATION EFFECTS ON MAGNETISM IN ZNO NANOCRYSTALS

4.1 Introduction

Semiconductor nanocrystals (NCs) have applications in biomedicine [75], chemical and gas sensors [88], spintronics, and light emitting devices [89]. Wide gap nanoscale semiconductors like ZnO (bulk bandgap energy, $E_g = 3.3$ eV [5, 28]) have shown potential as light emitters due to the size tuneable band gap energy [90] and unlike CdSe, ZnO is relatively less toxic than CdSe and thus is more suitable in biomedical roles such as cell labelers [91], drug delivers [75, 92], and has the potential for magnetic hyperthermia treatments [75, 93]. Along with the size tunable optical properties, ZnO nanocrystals also have been shown to exhibit magnetic properties at the nanoscale, thus making them a candidate for spintronic applications [94]. The emergence of magnetism in ZnO NCs is facinating since ZnO is a d^{10} system leaving no spare spin states for ordering magnetically [52]. There have been much work to understand the source of magnetism in ZnO nanoparticles, but there is still debate as to the exact mechanism [52, 54, 95–97].

Reports suggest that the cause of nanoscale magnetism is likely due to surface defects such as oxygen vacancies, cation vacancies, or cation interstitial ions [23, 24, 28, 41]. Sundaresan [14] and Garcia's [54] groups have shown that changes in the magnetization of nanoscale ZnO can be attributed the type of ligand attached to the particle's surface. Typically colloidal NCs utilize ligands during synthesis to change the growth rate and structure of the NCs [7]. Anther important use of organic molecules is to help stabilize the NCs in organic solvents [97]. Generally the lack of organic passivation leads to less stable NCs in solution, however not much is known about how the reduction of the surface ligand density affects the magnetic properties. Interestingly, the literature suggests the magnetometry results vary drastically even when prepared with similar synthetic methods.

Here we report how the surface ligand density can alter the magnetic properties of colloidal ZnO NCs. In addition, our work provides information that can help explain the various discrepancies of the magnetic properties of nanoscale ZnO.

4.2 Methods

4.2.0.1 Materials

Tetramethylammonium hydroxide (TMAH), zinc acetate dihydrate ($Zn(OAc)_2 \cdot H_2O$), dimethyl sulfoxide (DMSO), ethanol, ethyl acetate, oleic acid (OA), hexadecanol (HD), hexanes. All chemicals were used without further purification.

4.2.0.2 Synthetic methods for colloidal ZnO nanocrystals

ZnO NCs were synthesized by one of two synthetic methods. The first is a base-initiated hydrolysis and Zn^{2+} condensation technique described by Gamelin's group [61]. In a standard reaction, 22 mmol of TMAH is dissolved in 40 mL of ethanol and added dropwise to a constantly stirring solution of 13 mmol of $Zn(OAc)_2 \cdot 2H_2O$ in 135 mL of DMSO at room temperature. The reaction is immediately quenched by adding 50 mL of ethyl acetate. The NCs solution is divided into three centrifuge tubes and the NCs are collected by centrifuging the stock solution solution at 1200 rpm for 5 min. The supernatant is decanted and the NCs are redispersed in ethanol. This method typically yields NCs with diameters, d = 6.0 nm in size.

The second method follows a modified one pot approach described by O'Brien's [7] and Yin's group [62]. In a standard reaction, a 1:1 molar ratio of $Zn(OAc)_2 \cdot 2H_2O$ and OA are mixed in 15 mL of OD in a round bottom flask. The flask is heated under vacuum to 120 °C and held isothermally for 1.5 hr. This step is important to degas the Zn acetate (evaporate H_2O). The solution will be clear after the degasing step, but gradually turns white during the temperature ramp up to 286 °C. The solution is then held isothermally until the desired size is achieved ($\sim$5-30 min after the reaction temperature has been

reached). Once cooled to 50 °C, 10 mL of hexanes is added to the reaction mixture to aid in the purification process. The reaction mixture is divided into 2 centrifuge tubes and spun at 1200 rpm for 5 min. The supernatant is decanted and the NCs resuspended in hexanes.

4.2.0.3 Post annealing method

Nanocrystals were annealed using a Mullen TP tube furance outfitted with a glass insulator. NCs were added dropwise to silicon substrates and then loaded into glass boats. The NCs were ramped to 600 °C at a rate of 10 °C/min under flowing air. The samples were held isothermally for 1 hr before cooling to room temperature under flowing air. Samples were kept in air.

4.2.1 SQUID magnetometry

Magnetometry measurements were performed using a Quantum Design magnetic property measuring device (MPMS) with superconducting quantum interference device (SQUID) utilizing the reciprocating sample oscillator (RSO) as the transport attachment. Samples are prepared for magnetometry by adding a solution of NCs in a dropwise manner into a MPMS pill capsule and allowing the sample to dry in either in air or under a N_2 atmosphere until all of the solvent has evaporated. NCs prepared under N_2 were prepared in a plastic dome that had undergone 3 purge cycles to remove as much oxygen as possible. All samples were prepared using nonmagnetic tools, like sapphire blades and titanium tweezers, to minimize contamination from spurious magnetic impurities.

Isothermal magnetization experiments are performed at either 2 K with an applied magnetic field ranging from -7 T to +7 T. A standard magnetic field ramp begins at 0 T, increases to +7 T, decreases to -7 T, and finally increased back to 7 T. For this work, at large fields the diamagnetic components will dominate over the weak paramagnetic signal of the sample. To eliminate the diamagnetic contribution, at large fields, is linearly fitted and subtracted from the magnetization curve (Figure 2.10). After the subtraction of the

diamagnetic component magnetic saturation can be observed as a result of total spin alignment in the sample.

4.2.2 X-ray diffraction and x-ray photoelectron spectroscopy

X-ray diffraction were performed on an PANalytical X'Pert Pro diffractometer with Cu anode, using the x-ray mirror monochromator and PiXCel detector. Typical sequences interrogated the [110], [103], and [112] Bragg peaks, following Bragg's Law [81]. X-ray photoelectron spectroscopy experiments were performed using a SPECS hemispherical analyzer with an Al K-α anode as the excitation source. Typical XPS survey scans are performed from binding energies 1400 eV to 0 eV with a pass energy of 100 eV and step size of 0.5 eV. Fine scans on particular elements of interest use a pass energy of 20 eV and a step size of 0.2 eV. Samples were prepared from colloidal solutions by adding the solution dropwise to a Si wafer or a glass slide.

4.3 Results and Discussion

4.3.1 Nanocrystal characterization

X-ray diffraction (XRD) experiments show that the prepared NCs preferred the hexagonal crystal structure [98] (Figure 4.1). The peak broadening can be attributed to the growth of smaller NCs [52, 99]. This is evident after applying the Scherrer equation (Equation 2.2) where the estimated NC sizes from the titration method is $\sim$6 nm in size while the one-pot method yielded NCs $\sim$25 nm in size. It was found anecdotally that the reaction time did not play a role in size selection for the NCs prepared using the base initiated titration method, assuming the same molar ratios were conserved in each reaction. This is not true in the case of the NCs prepared using the one-pot method. Generally the longer the reaction continues, the larger the NCs become and that is understood to be a result of Oswald ripening, where smaller NCs are cannibalized to form larger NCs [52, 99].

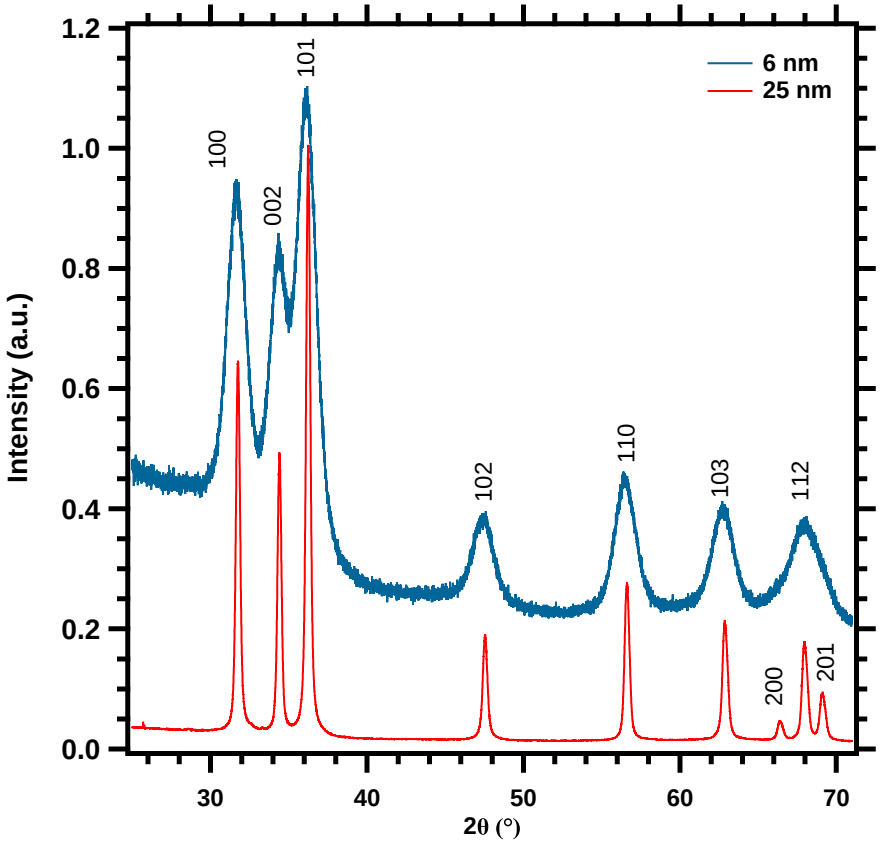

Figure 4.1: XRD Results for ZnO NCs prepared using the titration base method (blue) and the one-pot method (red). Both exhibit hexagonal structure owing to the main Bragg planes at $\theta = 32$ deg, 34 deg, and 36 deg for the [100], [002], [101] planes respectively. In general, the titration method will yield smaller NCs (∼6 nm) and the one-pot method will yield larger NCs (∼25) nm

X-ray photoelectron spectroscopy (Figure 4.2) results reveal binding energies for expected Zn, O, and C. Broad spectrum shows binding energies for Zn $2p_{1/2} = 1044$ eV, Zn2 $p_{3/2} = 1021$ eV, O $1s = 532$ eV, C $1s = 284$ eV, Si $2s = 149$ eV, and Si $1s = 100$ eV [67, 100, 101].

4.3.2 Variations in magnetization for similarly prepared ZnO nanocrystals

Interestingly, the variations in the magnetometry results for similarly prepared ZnO NCs, which is not surprising since reports in the literature are also in disagreement for similarly prepared ZnO NCs [52, 54, 95–97]. The NCs being compared are synthesized using the titration method (∼6 nm) and the one-pot method (∼25 nm). Both sets of NCs

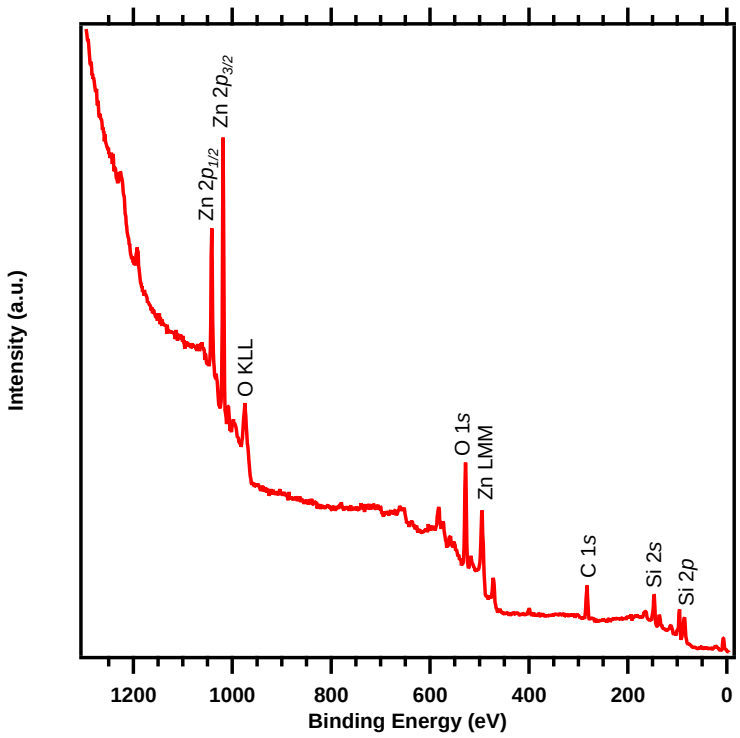

Figure 4.2: Survey scan of XPS spectrum for ZnO NCs prepared using the titration base method showing peaks expected Zn, O, and C peaks as a result of the sample and Si peaks because of the sample substrate.

are washed once to remove un-reacted materials and though the NCs are similar in size for the same synthetic method and the same number of post processing purification kept constant, there are significant variations in the 2 K magnetization curves (Figure 4.3).

The NCs prepared via the titration method possess TMAH (amine) as the capping layer while the one-pot method NCs are capped with OA (OH) and both synthetic methods display vast differences in M_s, which is consistent with literature reports. For instance, Garcia *et.al.* [54] have shown that ZnO NCs capped with tryoctylphosphine (TOPO), dodecylamine (amine), or dodecanethiol (thiol) showed significant differences in the M_s. Our titration based method (samples g1, g2, and g3 or 'g series') exhibit three distinct magnetization saturation values and the coercivities (Table 4.1) that vary greatly between various syntheses. Sample g1 exhibited the lowest M_s value for NCs prepared with the titration method, while the g2 and g3 samples exhibit 2 to 3 orders of magnitude larger magnetization values for similar size NCs. Interestingly, the coercivity, for the g1 sample is

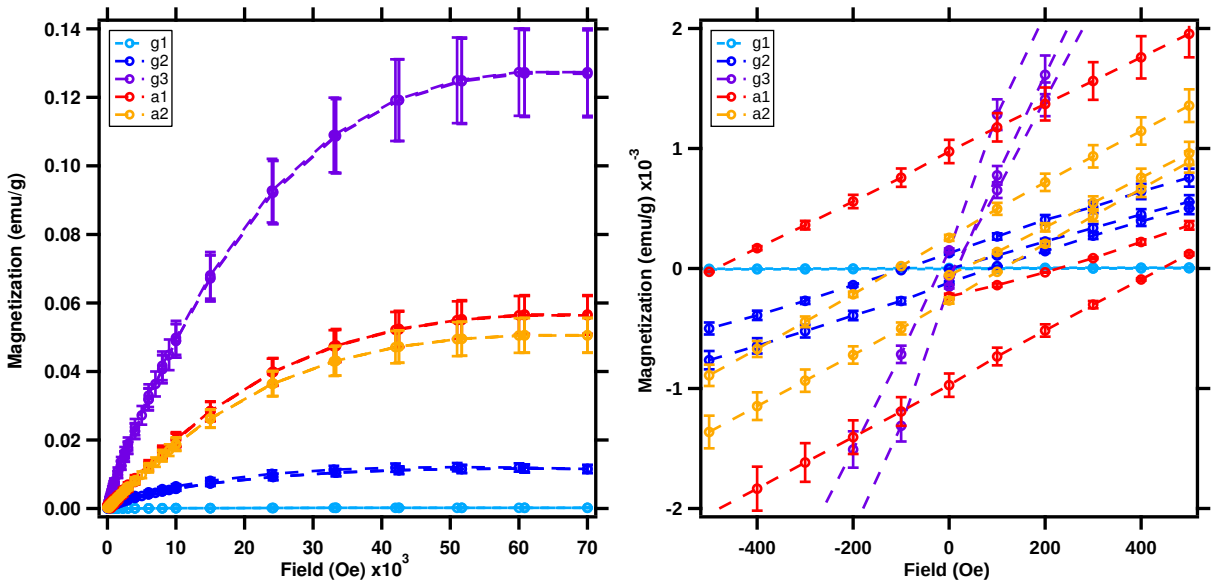

Figure 4.3: Magnetization results for ZnO nanocrystals prepared using the titration base method (g1,g2,g3) or the one-pot method (a1,a2). Only the first leg of the magnetization results are shown in the top figure and the bottom figure zooms in around 0 field to show coercivities for the samples

the largest (300 Oe) while the g3 samples possesses the coercivity (50 Oe). This is in contrast to the NCs synthesized using the one-pot method (a1 and a2 or a-series samples), where the magnetization values variations are similar, within error. That said, however, the coercivities of a1 is over twice as large as a2 (Table 4.1). To reiterate, the NCs are similar in size and post-processed similarly, yet the magnetic values are not consistent.

Sample	M_s (emu/g)	H_c (Oe)	Sample	M_s (emu/g)	H_c (Oe)
g1	0.0002	200	a1	0.056	350
g2	0.012	100	a2	0.051	100
g3	0.123	50			

Table 4.1: Table of the magnetization saturation, M_s, and coerivity, H_c values for ZnO nanocrystals prepared using the titration method (g series) and the one-pot method (a series).

A plasible explanation for the discrepancy in the magnetization data could depend on the number of oxygen vacancies. There have been reports discussing the effects of oxygen vacancies through annealing experiments to address this mechanism [24, 52], however, at this time I don't believe that the concentration of oxygen vacancies will change through

our post processing technique and that "starting" oxygen vacancy concentration should be the same for each set of NCs at wash 0.

The next variable that could account for the discrepancy in magnetization results is the "starting" ligand concentration. I have shown that for CdSe NCs (Chapter 3), through surface modification, we can alter the magnetic properties. We might expect similar behavior for ZnO as well, where the "starting" ligand density could vary from across synthesis. Going forth, I will examine the effects that surface coverage plays on ZnO NCs synthesized using the titration base method, based on the the preliminary results, as there is a larger deviation in the M_s and H_c values for what should be "identical" NCs.

4.3.3 Magnetization results of purified ZnO nanocrystals

The remainder of this chapter we will focus on the magnetization results for ZnO NCs prepared utilizing the titration method. Aside from the larger variation in M_s and H_c, I was able to consistently form a larger quantity and consistently similar sized ZnO NCs following this method over the one pot method. From the isothermal mangetization measurements at 2 K, the titration base synthesized ZnO NCs exhibit weak ferromagnetic properties (Figure 4.4). Each of the purified NCs exhibit weak ferromagnetic properties that changes nonlinearly after each wash. The NCs prepared in air show an initial magnetic saturation, $M_s = 0.1$ emu/g, and after the second purification of ZnO NCs, the magnetization increases to a maximum of $M_s = \sim 0.5$ emu/g. The NCs prepared under N_2 exhibit an initial magnetic saturation of $M_s = 0.4 \times 10^{-3}$ emu/g and increases to a maximum of 0.14 emu/g. The results are on the same order of magnitude to similarly prepared 4 nm ZnO NCs by Zhang's group [52] and to 3% Co doped 3nm ZnO NCs prepared similarly by Gamelin's group [94]. Interestingly, the coercivities (Figure 4.7) are not in agreement with reported values[52, 94]. Also note that the coercivity appears to change as we purify the NCs.

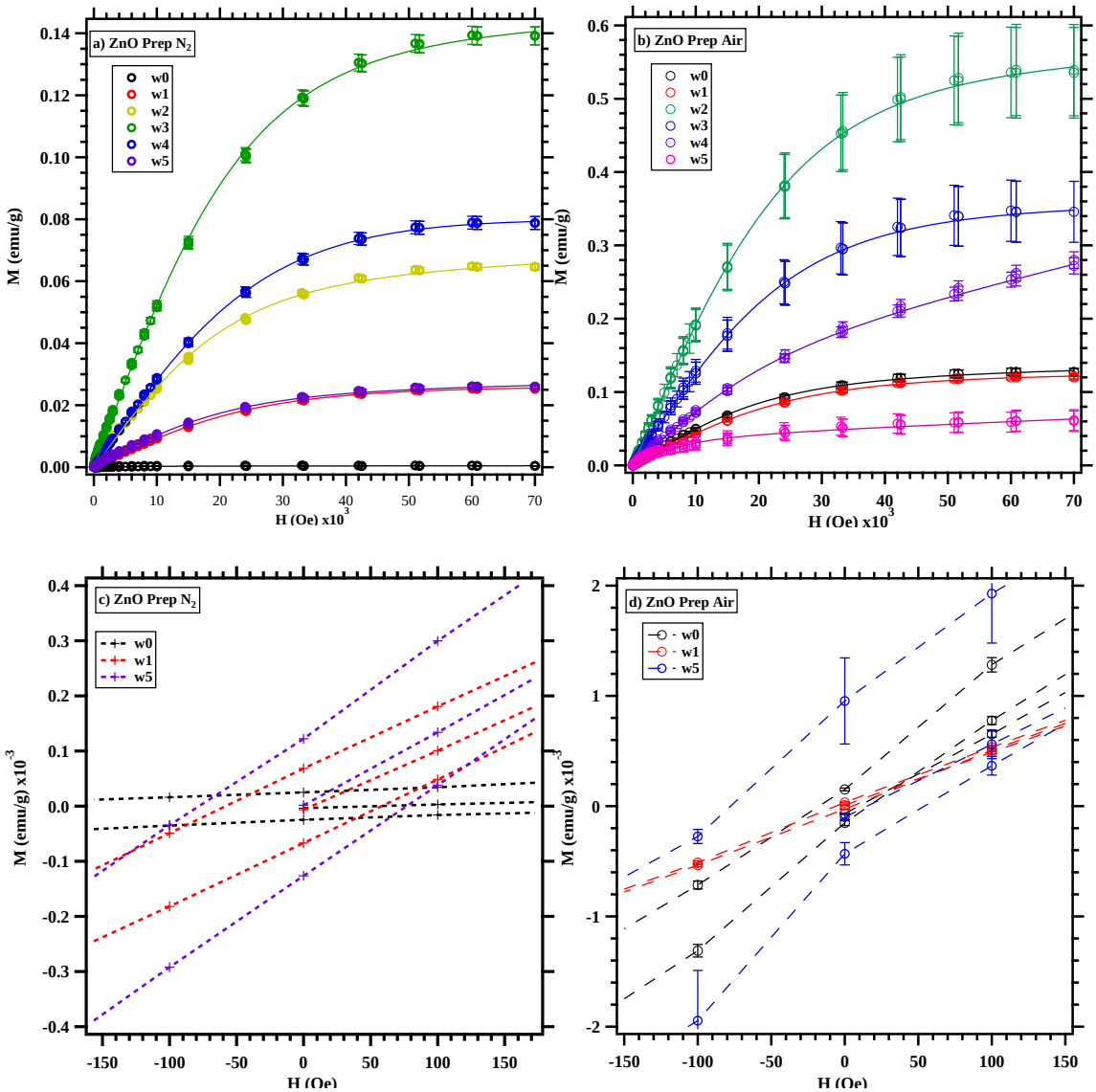

Figure 4.4: Magnetization curves for ZnO NCs dried under N_2 (a) and dried in air (b). Only the first leg of the of the magnetization data is shown, where the applied field ranges from 0 $<$ H $<$ 7 T. The solid lines are the fitted Brillouin curves using Equation 2.5. Select samples dried under dried under N_s atmosphere (c) and dried in air (d) zoomed in between -150 to +150 Oe, for clarity, in showing hysteretic behavior at low fields.

The M_s values for both the air and N_2 prepared samples exhibit an increase in M_s with increasing washes before a decrease in M_s. This trend is distinctly more noticable for the air prepared samples and occur relatively earlier (at wash 2) than for the nitrogen prepared samples (at wash 3) (Figure 4.5). This is reflective of an "on/off" mechanism, where by

removing ligands from the surface of ZnO NCs, we examine a switching "on" of magnetic "ions" to reach a "maximum" event in the magnetic saturation results, before an "off" event or ramping down of M_s begins. In the sense of dangling bonds, an increase in M_s is reflective of removing organic ligands after each purification step. That said, the continual decline in M_s is baffling, because this suggests the number of dangling bonds is decreasing.

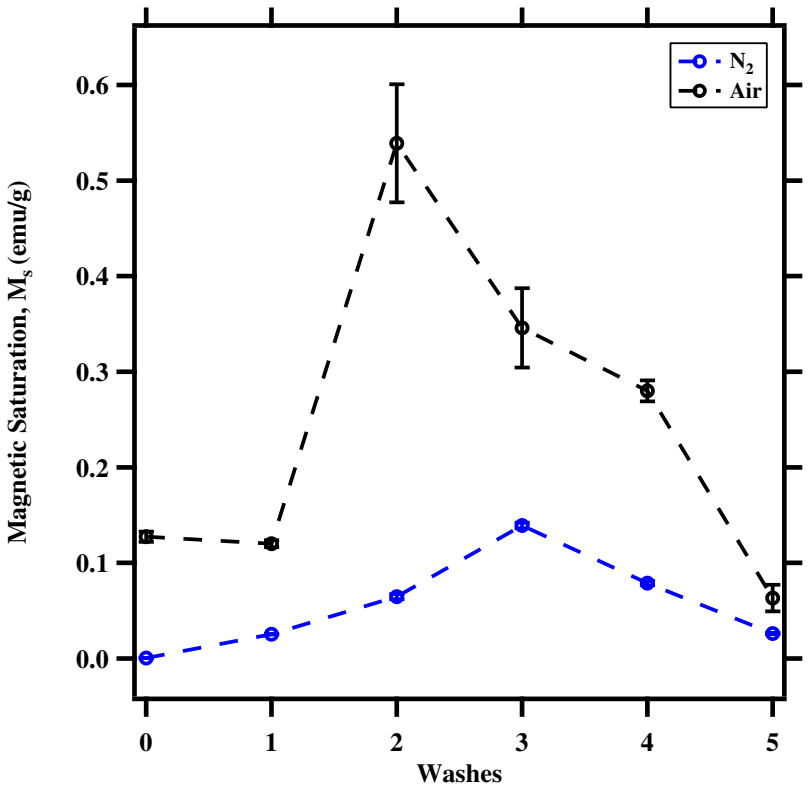

Figure 4.5: Magnetization saturation, M_s, values at 2 K for ZnO NCs prepared under N_2 (blue) and in air (black)

One potential side effect of utilizing ethanol as the antisolvent is that ZnO is known to adsorb easily ethanol [102, 103]. This means that as the native organic ligands are removed, ethanol can take the place of the ligands. When the NCs lose organic ligands, dangling bonds form, but because ethanol can bind to the surface of the NC, this reduces the number of danling bonds and thus reduce the M_s values. The change of magnetic "ions" N reflects the same behavior as M_s.

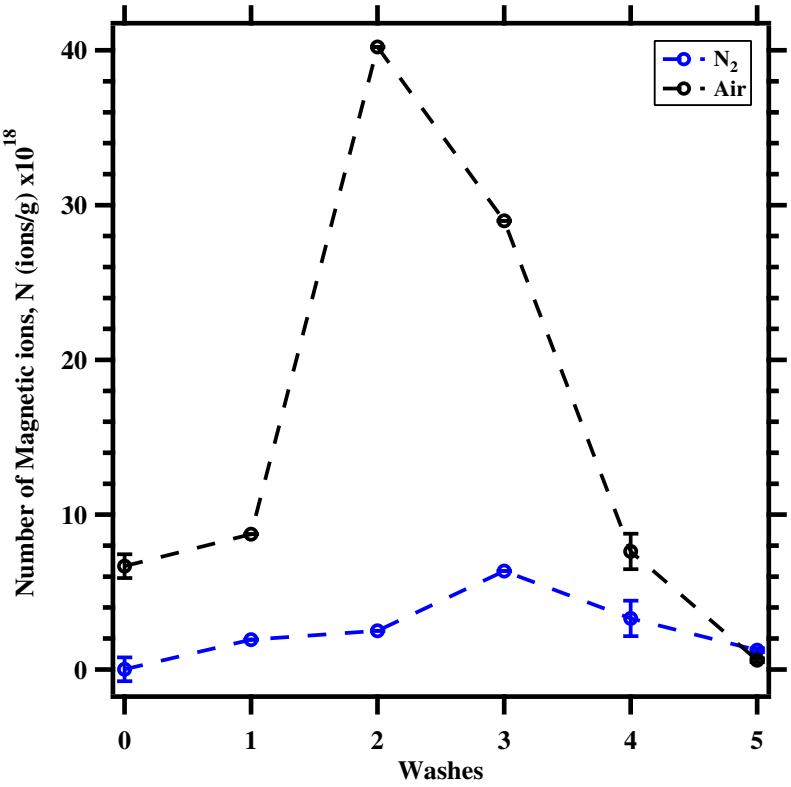

Figure 4.6: Number of magnetic "ions", N, fitted using the Brillouin function (Equation 2.5) from the M(H) at 2 K for ZnO NCs prepared under N_2 (blue) and in air (black)

The changes in the number of magnetic "ions", N, (Figure 4.6) are taken from fitting the M(H) curves to the Brillouin Fucntion (Equation 2.5). The N values for the NCs dried in air reach a "peak", at wash 2 and increase by a factor of 5 from wash 0. Then after the "peak" the N values decrease and at wash 5 N actually is below the N value for the wash 0. This suggests that for ZnO NCs dried in air, it is possible have fewer magnetic "ions" if purified enough times, presumably due to of ethanol adsorption. The NCs dried under a N_2 atmosphere follow a similar trend as the NCs dried in air, where there is a distinct "peak" in N value (wash 3). In this N_2 case, the wash 5 does not go below the N value for wash 0 like the NCs dried in air. The changes in M_s and N values as a function of purification suggests that ligand removal could be caused by the varying M(H) results that have been reported in the literature.

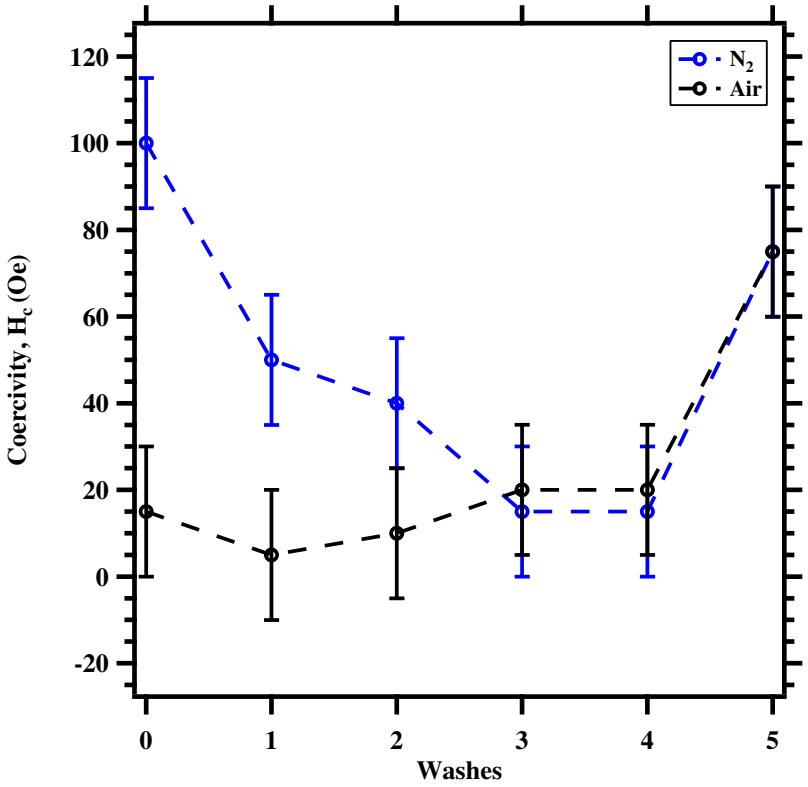

Figure 4.7: ZnO H_c values as a function of washing step.

The coercivity H_c (Figure 4.7) for the NCs dried in air show $H_c = 25$ Oe at wash 0 and gradually increases to a maximum of $H_c = 75$ Oe. The NCs dried under N_2 show an opposite trend where for wash 0 $H_c = 100$ Oe and decreases sequentially to $H_c = 20$ after the by wash 3. Then, interestingly the NCs dried under N_2 also reaches a final $H_c = 75$ Oe on wash 5 like the air dried samples. The convergence of H_c to 75 Oe for both air dried and N_2 dried samples suggests that after multiple washes the magnetic mechanism are tunable. Not only does H_c converge, but M_s as well, showing that even through the NCs are prepared differently, similar magnetic behavior can be achieved.

As the number of purification increases, the M_s values increase to a maximum of 0.5 emu/g before decreasing to $M_s = 0.05$ emu/g, below the wash 0 in air. At wash 4 and wash 5, the M(H) curves do not fully saturate (Figure 4.4), but there remains a positive linear response to an applied magnetic field. This could suggest an antiferromagnetic ordering beginning to emerge [6] as the number of surface ligands are removed after sequential

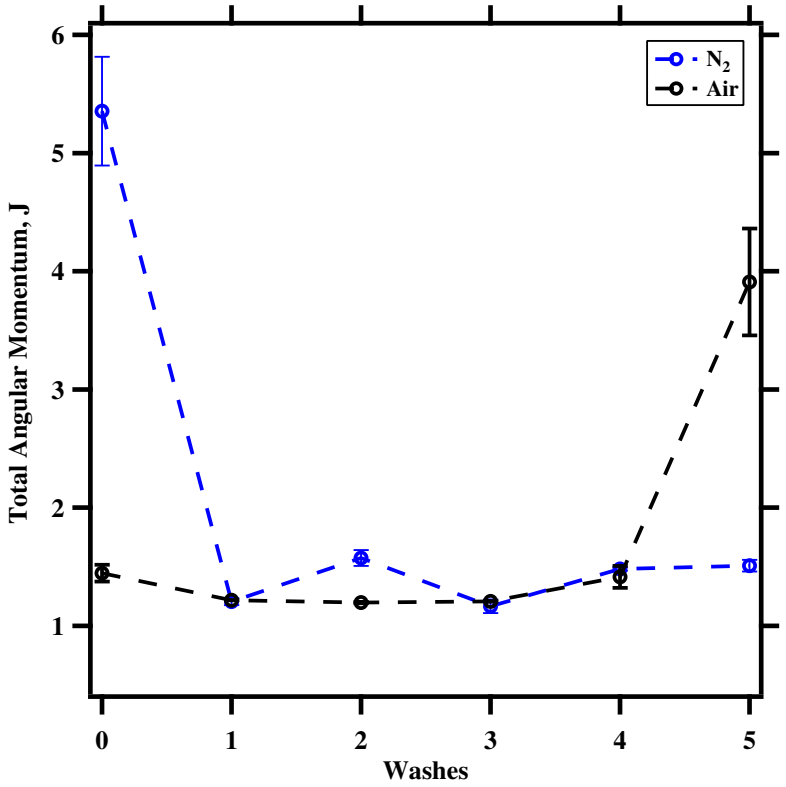

Figure 4.8: Total angular momentum, J, values for ZnO NCs fitted from the M(H) results using a Brillouin Function (Equation 2.5)

washing. To my knowledge, however, there have been no reports of ZnO NCs behaving antiferromagnetically without the aid of an antiferromagnetic impurity. Though unlikely an antiferromagnetic phase transition, it is plausible that another mechanism is emerging.

The total angular momentum, J, (Figure 4.8) show similar trends to the coercivity. The air dried samples show a final increase in J at wash 5 and the N_2 samples show an initially large $J = 5.5$ value before decreasing. In both cases, the majority of the washes we observe values of J =1.5 suggestive of oxygen vacancies. This does not help, however, explain the nonlinear response from the M(H) curves.

The complexity in the magnetic behavior arises from the observation that the magnetization does not continue to increase nor does it appear to asymptotically approach a large value with purification steps. I propose a modified model (Figure 4.9) on the previous dangling bond model presented in the CdSe chapter. It is believed the driving

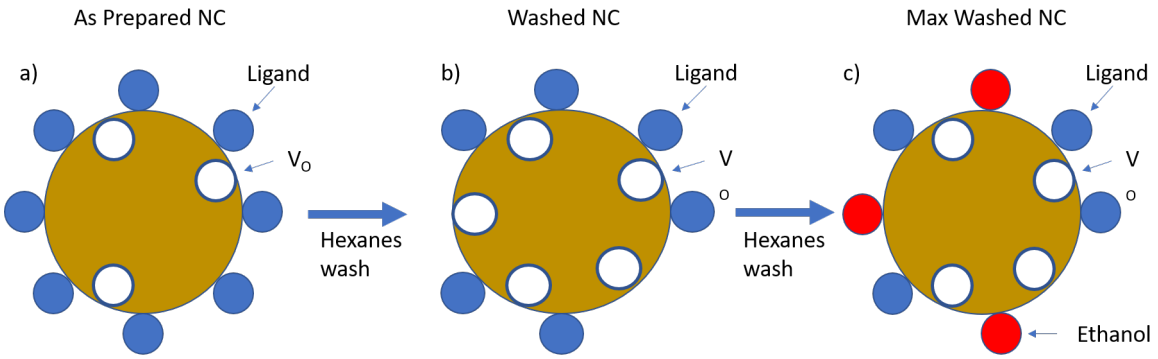

Figure 4.9: Model of ZnO NCs exhibiting an unwashed NC (a) with native oxygen vacancies. After purification ligands are removed and expose more oxygen vacancies (b). Upon further purification ethanol adsorbs the surface of the NC removing oxygen vacancies (c).

mechanisms behind the magnetic properties for ZnO NCs are oxygen vacancies, V_O [23, 24, 28, 41]. The NC surface is passivated with organic ligands, as previously described, but for ZnO NCs there exist oxygen vacancies that are passivated by the organic ligands. Upon removing organic ligands, we expose the oxygen vacancy. Then if we purify the NCs further, more ligands are removed. When enough ligands are removed, ethanol can bind to the surface of the NCs. ZnO is known to behave as a good ethanol sensor [102, 103], so it is likely that ethanol will bond to the exposed surface of the NC surface. This re-passivation of the NC surface reduces the number of oxygen vacanices on the surface of the NCs, thus resulting in the reduced M_s values by wash 5 for both sets of samples.

4.3.4 ZnO Annealed at 600 °C

To investigate the effects of oxygen vacancies on ZnO NCs we performed annealing experiments [24, 52] at 600 °C on the wash 0 NCs prepared in air. The M(H) results reveal ferromagnetic behavior at 2 K (Figure 4.10). The magnetic saturation, $M_s = 0.05$ emu/g is decreased by 50% compared to the un-annealed NCs. This is consistent with previous reports of annealed ZnO NCs [24, 52]. Assuming oxygen vacancies are a source of magnetism, annealing the NCs in air will passivate the oxygen vacancies. Fewer oxygen vacancies will reduce the magnetization saturation values. This is reflected by the number of magnetic "ions" obtained via fits of the M(H) curves to the Brillouin function (Equation

2.5). From the fit, $N = 2 \times 10^{18}$ "ions"/g, which is 4× smaller than the fit of the un-annealed sample. Interestingly, the M_s and N values of the annealed sample is attained by reducing the surface ligand density.

Along with the number of "ions", the fitted total angular momentum value is $J = 1.5$. This J, however, is associated with oxygen vacancies, similar to the un-annealed sample. Based on the fitted J value, this suggests that even after annealing at 600 °C for 1 hour not all oxygen vacancies are passivated. Remember, the surface is passivated with organic ligands that can be burned off during the annealing process, thus removing the possibility of surface ligand interaction. This means that the source of magnetism in "bare" ZnO is now unbound elections in the form of oxygen vacancies or dangling bonds.

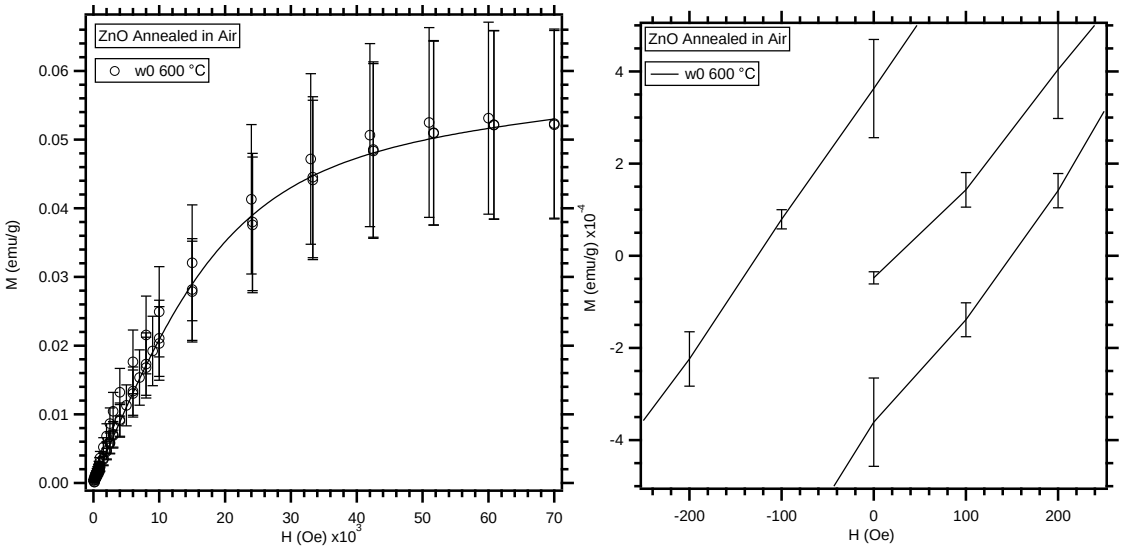

Figure 4.10: Magnetization curve (left) and the coercivity (right) for ZnO NCs annealed at 600 °C in air.

At first, unintuitively, the coercivity increased by 100% post annealing. One explanation could be that while annealing, ZnO NCs are forming larger grains or granuals. This has yet to be investigated at this time, but is a reasonable side effect of annealing at 600 °C. While annealing, the surface ligands that normally prevent agglomeration of NCs, would be removed allowing the NCs to fuse together. The closer proximity could lead to stronger ferromagnetic coupling, thus an increase in coercivity post annealing.

Interestingly, the coercivity for the annealed NCs prepared in air are approach the values of the wash 5 of the unannealed crystals, thus showing the potential in understanding the surface ligand density and it's role in magnetism of nanocale ZnO NCs.

4.3.5 Conclusion

The results from purifying colloidal ZnO NCs show that the magnetization can be tuned or controlled. We show, that the strength in magnetization increases to a maximum value with increasing number of purification steps, before decreasing to a value near the un-purified samples. Interestingly the M_s, H_c, and N values are similar in value to the highest post processed un-annealed samples. The difference are the amount of surface ligands, where the J values for un-annealed samples suggest that complex magnetism mechanism emerge when ligands are involved.

CHAPTER 5

COMPETITION BETWEEN MN DOPANTS AND SURFACE DEFECTS ON THE MAGNETIC PROPERTIES OF CDS AND CDS/ZNS CORE/SHELL NANOPLATELETS

5.1 Notice of Publication

Much of the work presented in this chapter has been reported in the Journal Chemistry of Materials, see "Exciton Energy Shifts and Tunable Dopant Emission in Manganese Doped Two-Dimensional CdS/ZnS Core/Shell Nanoplatelets [6]. The primary focus of this chapter will revolve around the magnetometry experiments of CdS and CdS/ZnS core/shell nanoplatelets.

5.2 Introduction

The previously discussed 0-dimensional CdSe and ZnO nanocrystal (NC) systems and found that the surfaces of these materials play an integral role in producing spin states that allow these d^0 magnetic systems to behave magnetically. This chapter focuses on an emerging class of nanostructure systems called nanoplatelets (NPLs) while focused on the same family of chalcogenide II-VI semiconductors. NPLs have an advantage over conventional NCs due to their narrow absorption and flouresence properties [6, 104] along with improved photoluminescence quantum yield over quantum dots[105–107]. As a result, these semiconductor NPLs are highly desirable in optical and electronic applications [108, 109]. Little is known, however, about the magnetic properties of CdS or CdS/ZnS core/shell NPL systems

As seen from the previous work on CdSe and ZnO, surface defects are the primary source of magnetism in these nominally nonmagnetic materials. NPLs are predominantly surface, but are generally well passivated, and possess few trap states [110], i.e. few dangling bonds on the surface. Surprisingly, the results provide evidence for

paramagnetism in undoped CdS and CdS/ZnS core/shell NPL systems and suggest that this magnetism is driven by surface defects. Furthermore, the postulate is that the magnetic properties of these systems can be enhanced by introducing a magnetic impurity, such as Mn, that can interact with the surface states. Herein we attempt to exploit the surface defect states of CdS and CdS/ZnS NPL by introducing Mn atoms in an attempt to couple the unpaired spin in the Mn d orbital states with the surface states, which can lead to novel magnetic properties.

5.3 Methods

CdS and CdS/ZnS core/shell nanoplatelets (NPLs) were synthesized by Zheng's group [6]. Briefly a typical synthesis of 2D Mn:CdS NPLs is performed via a one-pot method. Cadmium myristate (0.2 mmol), zinc acetate (0.2 mmol), s-octadecene (1.0 mL), and 1-octadecene (9.0 mL) were combined in a three-neck round bottom flask. The mixture was degassed for 30 min at 100 °C and then cooled to room temperature under argon. Manganese nitrate, in minimal methanol, is injected and the solution is degassed for 30 min at room temperature and another 30 min at 100 °C. Afterwards, the mixture is heated to 200 °C and held isothermally for 1 h under argon and lastly the mixture was cooled to room temperature for post processing.

Powder x-ray diffraction patterns were performed using a Bruker D2 Phaser with LYKXEYE 1D silicon strip detector using Cu Kα radiation (λ = 1.5406 Å). Samples were drop-cast onto pyrolitic graphite and vacuum dried. Ultraviolet-visible spectroscopy measurements were collected on an Agilent Cary 60 spectrophotometer [6]. To reiterate, both the XRD and UV-vis characterization techniques were performed by the collaborators at Syracuse University and further reading can be found in Ref [6].

Magnetometry experiments were prepared on as received NPLs. All samples were prepared for magnetometry experiments in air. The magnetometry measurements were performed using a Quantum Design superconducting quantum interference device (SQUID)

with a DC transport head. Once the sample has been positioned on the transport, the sample chamber is purged 3 times to remove as much O_2 as possible. After purging, temperature dependent susceptibility measurements are performed as either zero field cool (ZFC) or field cooled (FC) sequences. For ZFC scans the sample is cooled from 300 K to 2 K without an applied magnetic field. For FC scans, the sample is cooled to 2 K from 300 K under the influence of an applied magnetic field, usually 100 Oe. Note, when cooling to 2 K, the sample chamber is held isothermally at 20 K for an hour to ensure the sample is are thermalized. After the cool down, the temperature is ramped to 300 K over the course of 4 hrs at a constantly applied field, usually 100 Oe. The measurement yields the magnetic susceptibility, $X(T)$, and is fitted to a modified Curie-Weiss Law as follows,

$$\chi = \chi_0 + \frac{C}{T - \Theta} \tag{5.1}$$

where χ_0 is a temperature independent term, C is the Curie Constant, T is the temperature, and Θ is the Curie Temperature.

Isothermal magnetization experiments are performed at either 2 K with an applied magnetic field ranging from -7 T to +7 T. A standard magnetic field ramp begins at 0 T, increases to +7 T, decreases to -7 T, and finally increased back to 7 T. For this work, at large fields the diamagnetic components will dominate over the weak paramagnetic signal of the sample. The diamagnetic contribution, is removed by taking a linear fit to the M(H) curve at large fields and subtracting the linear contribution from the magnetization curve. After the subtraction of the diamagnetic component magnetic saturation can be observed as a result of total spin alignment in the sample.

5.4 Results

5.4.1 X-ray diffraction results

The powder x-ray diffraction of CdS and Mn:CdS NPLs revealed cubic phase CdS (Figure 5.1). Further examination of XRD patterns indicates diffraction peaks shifting to

higher angles with increasing concentrations, this can be explained as a lattice compression from replacing Cd^2+ (92 pm) ions with Mn^2+ (80 pm) atoms [6].

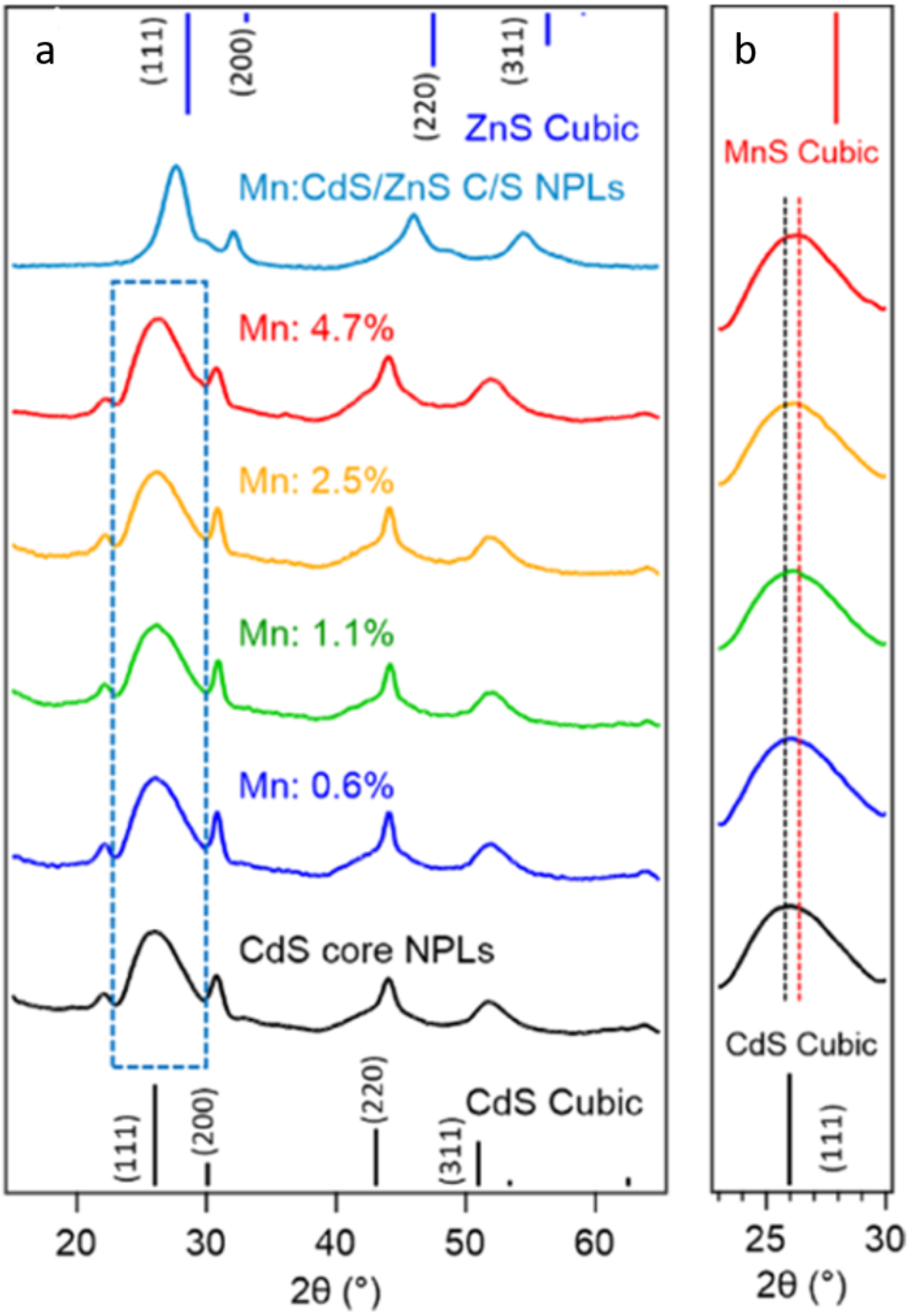

Figure 5.1: (a) Powder XRD patterns of Mn:CdS core NPLs and Mn:CdS/ZnS core/shell NPLs. (b) Zoomed-in XRD patterns showing peak shifting of the (111) diffraction peak by increasing Mn-doping concentration.

5.4.2 Magnetometry of CdS and CdS/ZnS Nanoplatelets

The isothermal magnetization curves for undoped CdS and CdS/ZnS core/shell NPLs exhibit paramagnetic (PM) properties (Figure 5.2). The NPL systems do not show evidence for magnetic impurities [6], suggesting that this PM nature is likely due to surface defects. In both the core and core/shell NPL systems, the M_s value are similar for the undoped NPLs (Figure 5.3), suggesting that source of magnetism on the surface is similar. The specific type of defect is still under debate, but PM in CdS nanoparticles have been associated with surface defects [111]. In the case of ZnS, Zn or S vacancies can exist in ZnS NCs [99, 112, 113], potentially giving rise to unpaired surface spins states. For ZnS, a S vacancy, V_S, will typically yield a green flourescence emission and a Zn vacancy, V_{Zn} will result in an orange emission [99]. For our NPLs we observe a strong defect emission for the undoped CdS system (Figure 5.4a) centered around 500 nm. After shelling or coating the core with ZnS layers, the CdS defect emission appears red-shifted and centered around 580 nm. Generally, when forming core/shell structures, the shell removes surface defects [6, 110] which is likely the case after coating with ZnS. Then instead of a redshift, it is more likely that the small emission around 580 nm is associated with Zn vacancies in the ZnS shell. The relatively low intensity of the defect emission peak is consistent with good ligand coverage on the ZnS surface, leaving a low concentration of defect states. Unfortunately, after doping, with Mn, a Mn based emission (5.4b) occurs around the same energy as the V_{Zn} emission peak which makes differentiating emissions from V_{Zn} defects from the Mn peaks difficult in the shelled emission spectrum.

After doping the NPLs, we observe changes in the M(H) curves (Figure 5.2) in the form of increasing M_s values (Figure 5.3) for both core and core/shell structures. The increase in magnetization is expected with increasing dopant concentration as seen similarly in a ZnO NCs [114]. Interestingly, the shelled structures exhibit significantly larger M_s values, approximately $\sim 3\times$ compared with similarly doped core NPLs. The Mn dopants are suggested to reside in the CdS core, even after shelling [6]. To explain the similarities in

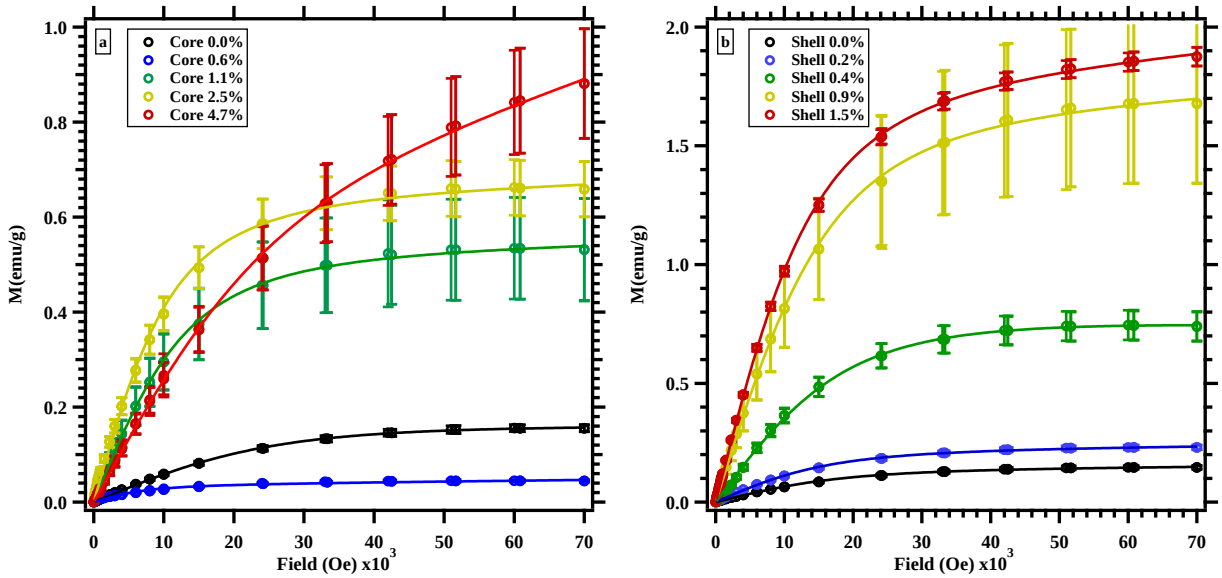

Figure 5.2: Isothermal magnetization data at 2 K for CdS NPLs (a) and CdS/ZnS core/shell NPLs (b). Only the first "leg" or magnetization results as H = 0 T → H = 7 T → H = 0 T

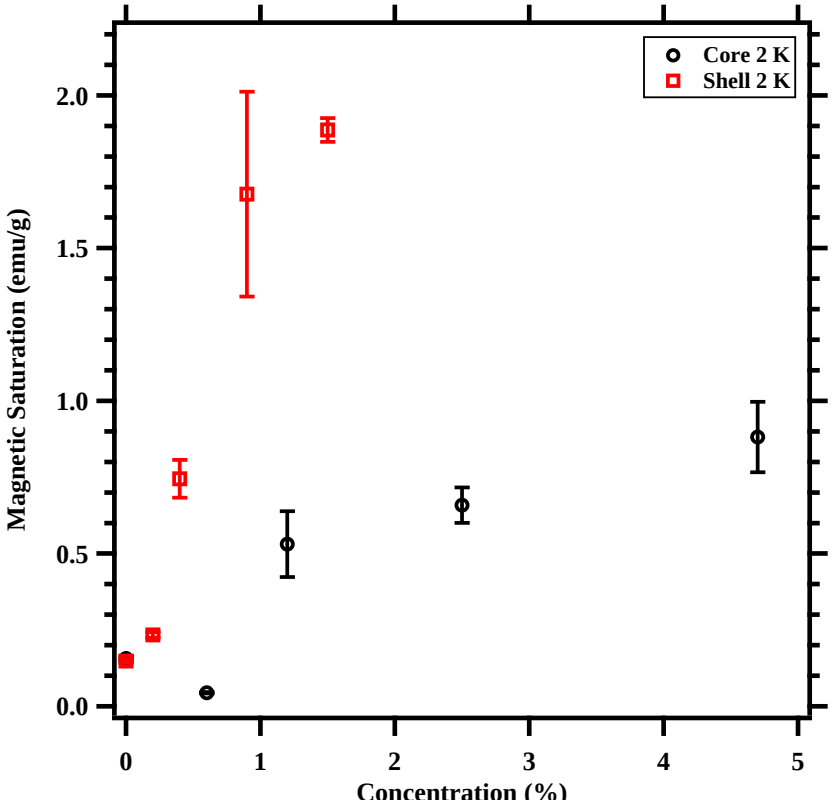

Figure 5.3: Isothermal magnetic saturation, M_s, values for CdS (black) and CdS/ZnS (red) NPLs as a function of molar Mn% concentration.

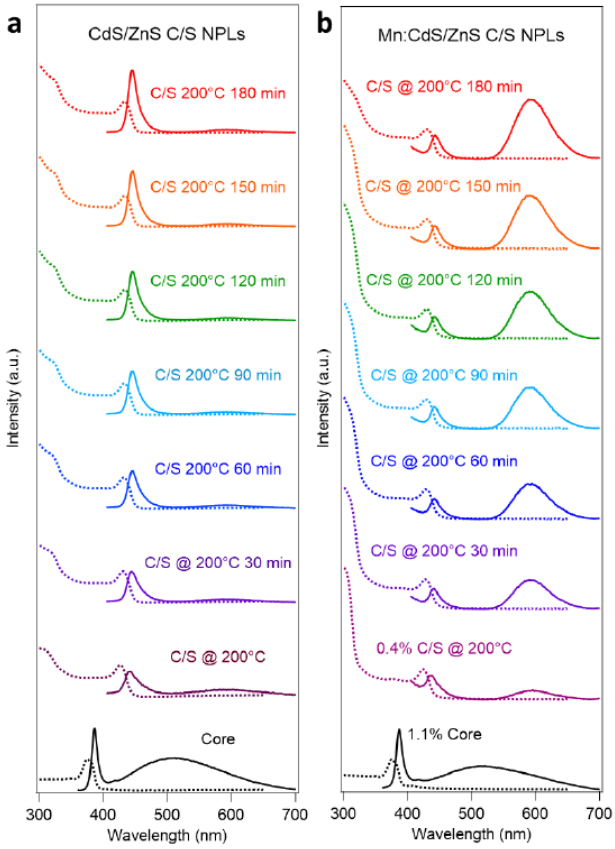

Figure 5.4: Photoluminescence (solid line) and absorption (dotted line) spectroscopy on CdS and CdS/ZnS NPL undoped (a) and doped (b). The spectroscopy exhibits how the optical properties change post shelling (forming core/shell) and at various annealing temperatures.

M_s values for the core only and core/shell materials, I propose a model where the doped Mn atoms interact with surface defects as shown in Figure 5.5. This model suggests that the undoped NPLs exhibit surface defects which would result in PM behavior. For the core only material, the introduction of Mn atoms can introduce PM impurities that can couple with surface defects resulting in increases in M(H). After increasing the doping concentration, the Mn dopants begin to align antiferromagnetically as suggested for Mn doped ZnO nanoparticles [114, 115]. This is evident in the 4.7% core NPL (Figure 5.2), where the M(H) does not formally saturate as observed for the other magnetization results. The lack of magnetic saturation or continual increase in M(H) can be interpreted as an antiferromagnetic ordering of Mn [6].

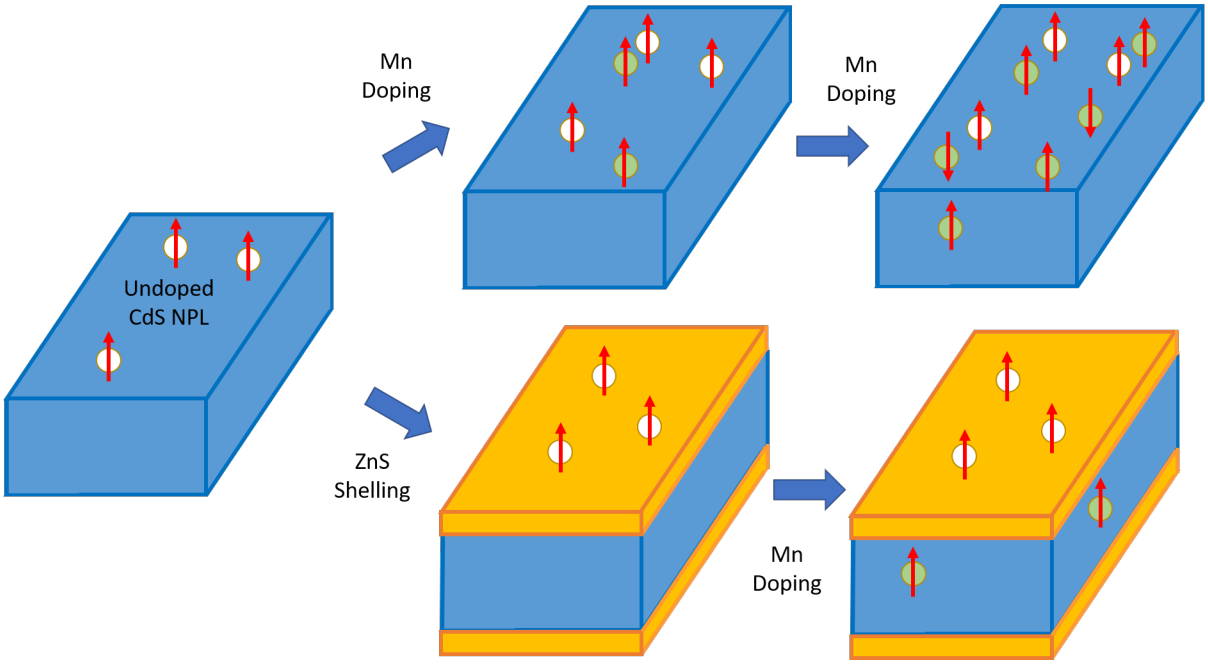

Figure 5.5: Schematic of pure CdS NPLs (top) before doping and after low Mn doping Mn align paramagnetically and after heavy doping NPLs align antiferromagnetically. Shelling of CdS NPLs (bottom) exhibit surface defects and after Mn doping PM coupling emerge

After shelling, the ZnS covers the native CdS defects, as suggested from the PL results (Figure 5.4), but reintroduces defects in the shell layer likely as V_{Zn}, since the defect emission is ~600 nm [113]. Upon Mn doping, the low concentration of Mn atoms behave as PM centers similar to the core model. The PM centers couple with the V_{Zn} increasing the saturation magnetization. To explain the larger M_s values for shelled NPLs compared to just the core, I speculate that the large M_s values are associated with Mn coupling with surface V_{Zn} which can have spin $S = 1$ [99]. This can be explained a couple of ways with the first explanation implying that the surface defects for CdS NPLs are different than ZnS. The likely defect for CdS (as of now anyways) is a result of unpassivated surface atoms with a spin states $S = 1/2$ or 1. Another explanation for the increase in M_s could be due to a variation in surface defect density, however, NPLs are known for their lack of surface defects, so the variation in defect density is unlikely the reason for the variation, thus the difference in spin states is more reasonable for explaining the larger M_s in the shelled NPLs.

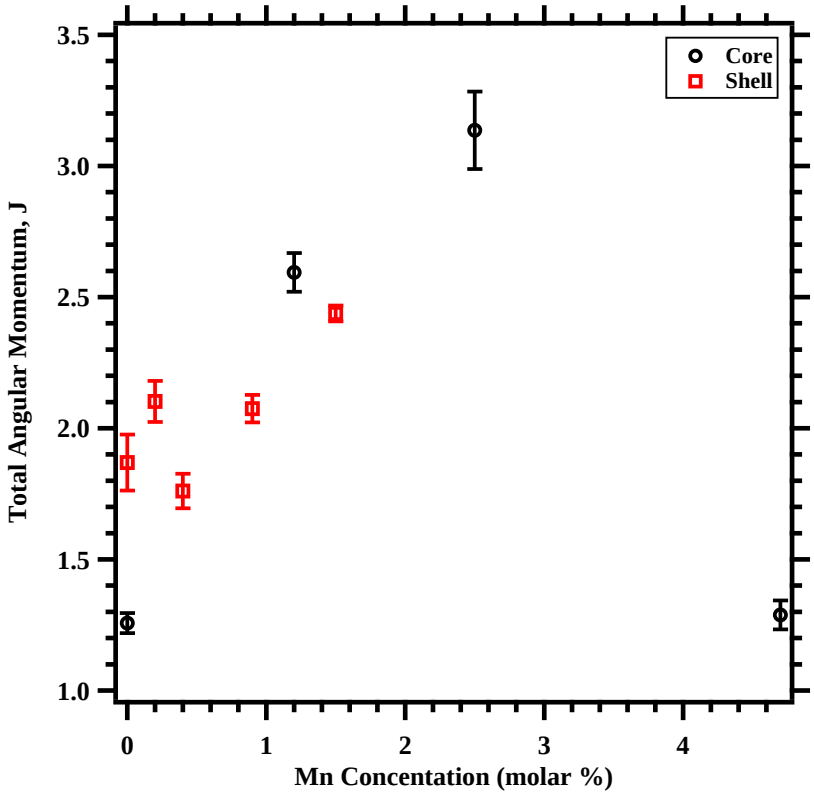

Figure 5.6: Total angular momentum values, J, for CdS NPLs (black) and CdS/ZnS core/shell NPLs (red) as a function of Mn concentration.

To see the difference in spin states, we can extract the total angular momentum, J, value from the M(H) curve, by fitting to the Brillouin function (Equation 2.5). From Figure 5.6, the core exhibits a $J = \sim 1.5$ and the shell exhibits a $J = \sim 2$. Though the difference in J is only ~ 0.5, this difference is enough to suggest different spin states for each system. Typically a $J = 1$ is associated to unpaired spins with $S = 1/2$ and $J = 3/2$ is associated with a $S = 1$. Since the fits are an average of the whole NC sample, an associated $J = 2$ is likely an average of unpaired spins and V_{Zn} spin states, which is consistent with the proposed model for NPLs and a $J = 1.5$ is also a combination of spin states, but predominately $S = 1/2$ systems. After doping we see a general trend of increasing J to $J = 3$. This is consistent with a Mn^{2+} spin system suggesting that as doping concentration increases the NPLs take on the Mn^{2+} spin state. At large

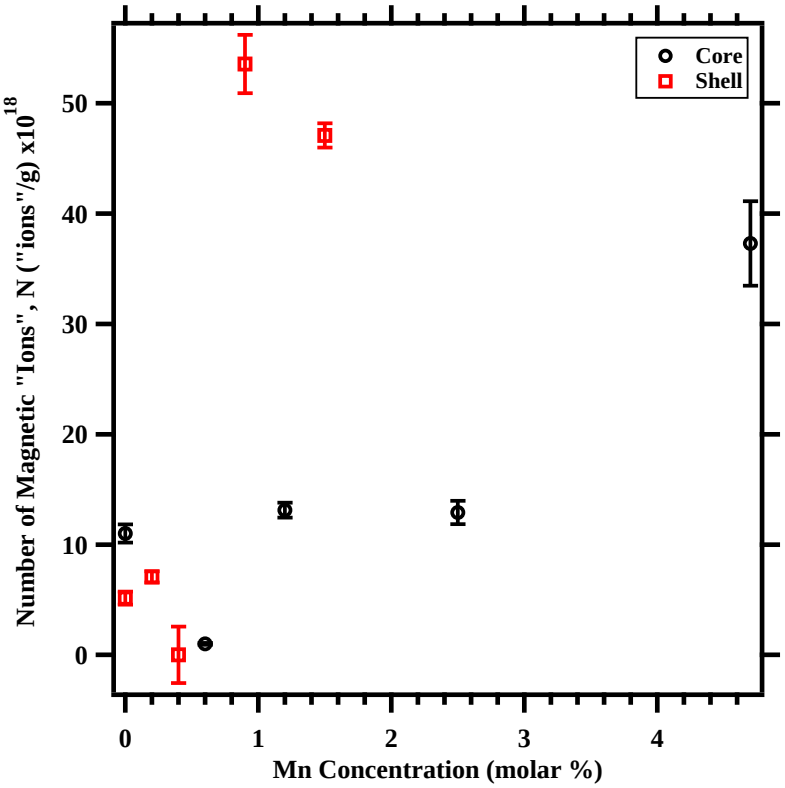

Figure 5.7: Number of magnetic "ions", N, from the Brillouin fit (Equation 2.5) for core (red) and shell (black) NPLs.

concentration (4.7%) the total angular momentum decreases to $J = \sim 1.5$ which is likely a result of antiferromagnetic coupling at larger concentrations.

After examining the temperature dependent susceptibility, χ, (Figure 5.8) the NPLs exhibit strong temperature susceptibility at low temperatures (T $<$ 5 K) as a drastic increase in χ. The strong increase or Curie-tail is typically associated with surface defects [6]. From the temperature susceptibility FC and ZFC curves, no evidence for Fe or other magnetic impurities are present as the χ curves resemble Pauli paramagnetism. Fitting the temperature suceptibility to the modified Curie Weiss law (Equation 5.1) we see that the Weiss temperature trends negatively (Figure 5.9) with increasing negative values suggesting antiferromagnetic interactions with increasing Mn concentrations. This is consisent with the absence of magnetic saturation in the 4.7% Mn:CdS NPLs.

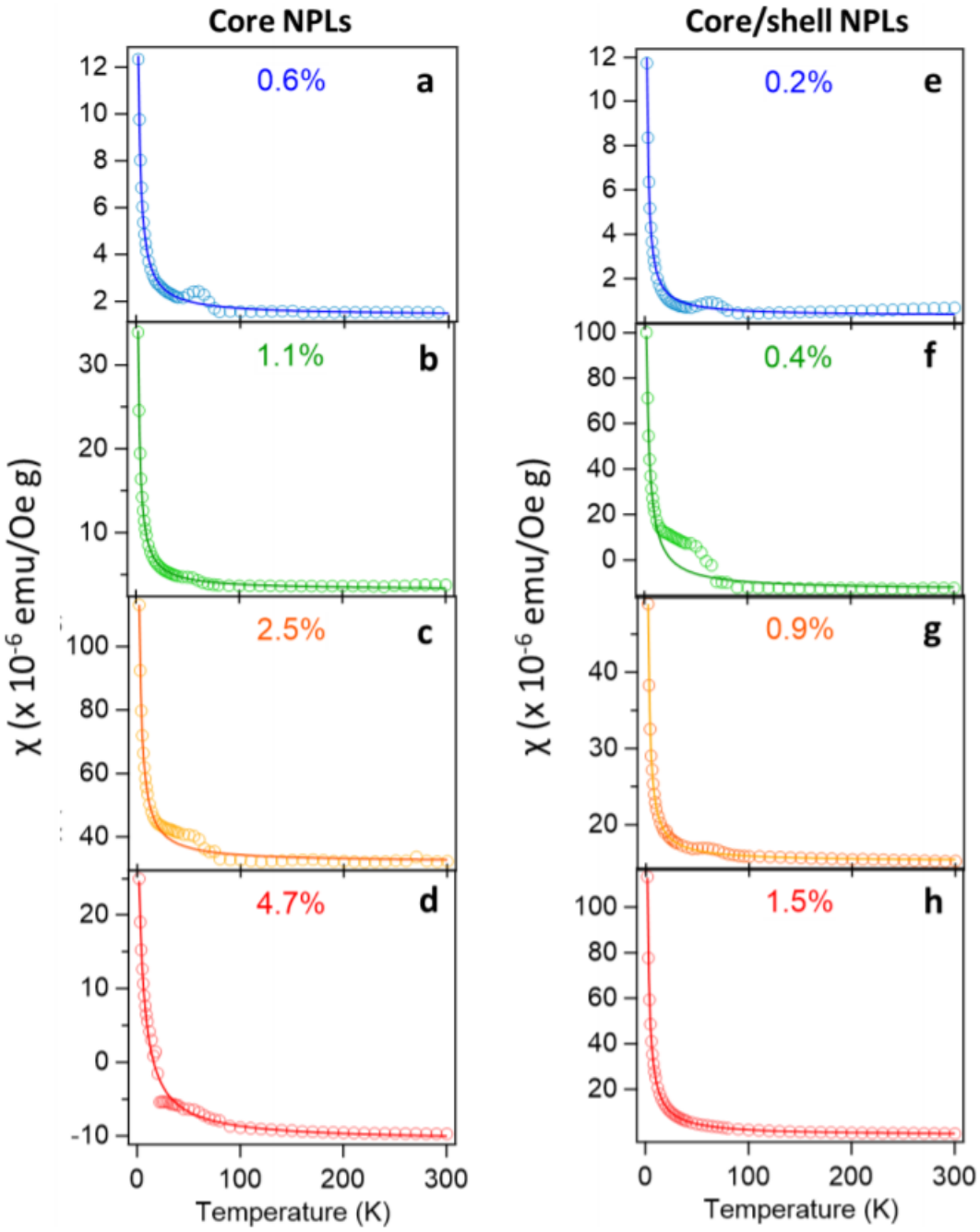

Figure 5.8: Field cool FC magnetic susceptibility curves for (a) 0.6%, (b) 1.1%, (c) 2.5%, and (d) 4.7% Mn:CdS core and (e) 0.2%, (f) 0.4%, (g) 0.9%, and (h)1.5% CdS/ZnS core/shell NPLs. The solid lines are the fitted curves using the modified Curie-Weiss Law. (Equation5.1). The bumps ∼50 K are a result of oxygen present in the sample resulting in a weak paramagnetic signal [6]

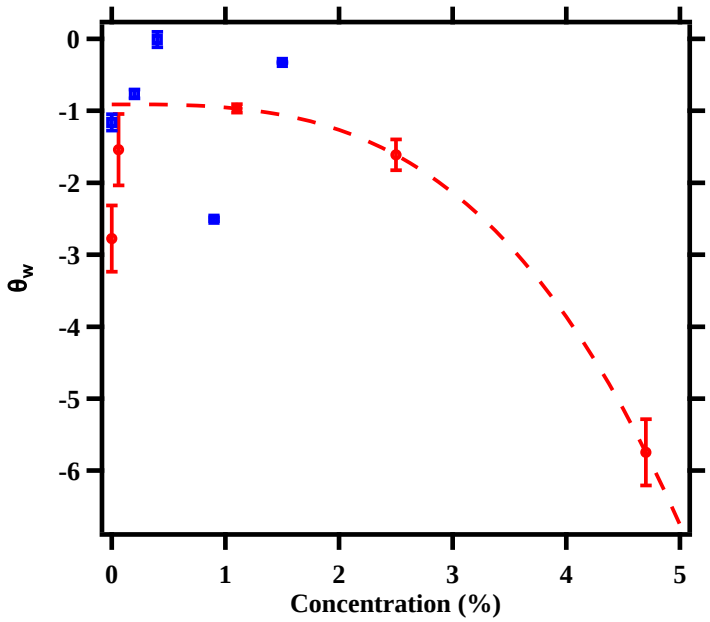

Figure 5.9: Fitted Weiss temperature after fitting the temperature suceptibility field cooled curves to the modified Curie Weiss law (Equation 5.1). CdS NPL values are shown in red and CdS/ZnS NPL are shown in blue and a the red dashed line is to guide the trend in Weiss temperature.

5.5 Conclusion

Potentially, CdS and CdS/ZnS NPL can combine their inherently strong optical properties coupled with enhanced magnetic properties can engineer improved optoelectronic and energy harvesting devices. Undoped NPLs exhibit paramagnetic properties at 2 K and upon doping the M_s values increase. The addition of Mn imparts PM properties at low concentrations and we show that the highest doped NPL system begin to couple antiferromagneticly. The PM Mn centers show evidence for coupling with the native NPL defects present on the surface, thus enhancing the magnetization.

CHAPTER 6

FINAL REMARKS

6.1 Final conclusions

The surface chemistry of CdSe and ZnO nanocrystals (NCs) along with CdS and CdS/ZnS core/shell nanoplatelets (NPLs) was shown to have an impact on the magnetic response of these nanomaterials. This thesis described how post purification of colloidal CdSe and ZnO nanocrystals can modify the surface chemistry and influence the magnetism in inherently weak paramagnetic or ferromagnetic NCs. For the CdSe case, post purification resulted in changes in the magnetization which were deduced to be a combination of unpaired electrons, oxidation effects, and surface reconstruction. CdSe NCs prepared in air showed a gradual convergence of magnetic mechanisms towards an oxidized surface while CdSe NCs prepared under inert conditions showed evidence for the formation of a triplet Se-Se bonds. In either scenario, it is was found that there is no one mechanism behind the magnetic properties of CdSe NCs. This can be seen from the complex total angular momentum, J, values from the Brillouin fittings, where large J values can suggest a complex mechanism and lower J can correspond with atomic states.

From the ZnO results, it was concluded that there is a strong correlation with the number of purification steps and the magnetization response. The magnetic mechanism is likely a result of forming surface oxygen vacancies, V_O. This was evident in the constant J values that are consistent with a spin S = 1 V_O. The model for the titration based method suggests that during the purification procedure, the removal of surface ligands can lead to the formation of oxygen vacancies. The surface V_O are capable of being passivated with the solvent, ethanol, leading to a decrease in the magnetic saturation values. Even for a ferromagnetic material like ZnO, the surface properties can have a profound impact on the inherent magnetism.

Lastly, colloidal CdS and CdS/ZnS core/shell NPLs, exhibited paramagnetic magnetic response and increased in magnetization with increased doping concentration. The inherent magnetism stems from the surface of these NPLs, where the surface of CdS nanoplatelets likely possess surface vacancies as seen through the emission spectrum. After shelling, it was observed that the magnetization was and can be attributed vacancies on the ZnS shell. After doping, the magnetic impurity can promote spin alignment resulting in further increases in magnetization saturation. The results from the doped NPLs reveal a complex magnetic mechanism with surface vacancies coupling with magnetic impurities to enhance the native paramagnetism.

The work presented in this thesis has shown that II-VI semiconductor materials, at the nanoscale, exhibit weak, but modifiable magnetic properties due their unique surface properties. The mechanisms explored included a purification process for colloidally stable CdSe and ZnO NCs and the incorporation of Mn dopants in CdS and CdS/ZnS core/shell materials. It is clear that even a standard post-processing technique can modify the magnetic properties, which could potentially explain discrepancies reported in the literature on these NC systems. Regardless, this work suggests that the surface of these NCs combined with traditional magnetic doping have the potential engineer stronger semiconductor materials.

6.2 Future works and prospects

The work presented in this thesis is heavily dependent upon magnetization results, which is only one component of the whole story for understanding the complex physics and chemistry for CdSe, ZnO, CdS, and CdS/ZnS core/shell nanomaterials. More work is still needed to be done, such as a more in-depth elemental analysis, for instance via x-ray photoelectron spectroscopy (XPS). We've suggested that the driving mechanism behind the occurrence of weakly paramagnetic (PM) and ferromagnetic (FM) properties in these systems is due a competition between surface oxidation and reconstruction. For the case of

CdSe nanocrystals (NCs), we observed a strong SeO_2 XPS peak for samples dried in air, while NCs dried under N_2 show very little to no emergence of SeO_2. This was expected after exposing NCs to air, as seen by Alivisatos' group [116]. Due to time constraints, we were unable to pursue detailed XPS studies for all samples, as an obvious way to observe changes in oxygen concentrations is through analyzing the O 1s XPS spectra. This can also be applied to the case of CdS and CdS/ZnS core/shell nanoplatelets (NPLs). For instance, to probe surface vacancies, [99, 112, 113] we could be examine changes in the Cd 3d, Zn 2p, or S 2p XPS spectra.

The next component that would complement our results would be the quantification of ligand coverage. We know that there appears to be a limit on the maximum number of ligands that can be removed due to electrostatic effects [57], but quantification of the ligand density could be performed via stanard methods such as thermal gravimetic analysis (TGA). Again, due to time constraints this was not possible, but TGA would be a good way of quantifying how the surface ligand density is changing after each successive purification step. An issue that arises when working with colloidal NCs is the difficulty in reproducing the exact same NC over multiple syntheses, as employing if identical molar ratios can still lead to batch to batch variations in the NCs, specially terms of ligand coverage. A potential drawback in how we present our data is that NCs of similar size and number of purification steps may not be similar, at least without adequate ligand density characterization.

The motivation for this work was to develop an understanding of how an optically active, but typically nonmagnetic material, could be utilized for applications such as spintronics and biomedicine. Obviously the work presented in this thesis sets up the framework for PM or FM devices that can operate at room temperature, but in our current discussion we only elaborate on magnetization results at 2 K. Our results, however, do show that post processing of these materials will introduce new spin states that can participate in exchange interactions, like in the CdS and CdS/ZnS NPL systems.

Unfortunately the thermal dynamics at room temperature are enough to disrupt any exchange correlation between magnetic spin states. Moving forward, with the given results, we can examine doped NCs systems to try and develop a multifunctional NC that possess both optical and magnetic behavior. Furthermore this information is also potentially useful for superpatamagnetic Fe_3O_4 systems by incorporating a number of simple purification steps coupled with the preexisting spin states, we can improve the magnetic performance in those systems.

REFERENCES

[1] D. Panda and T.-Y. Tseng, "One-dimensional ZnO nanostructures: fabrication, optoelectronic properties, and device applications," *Journal of Materials Science*, vol. 48, pp. 6849–6877, oct 2013.

[2] Q. Peng, Y. Dong, Z. Deng, and Y. Li, "Selective Synthesis and Characterization of CdSe Nanorods and Fractal Nanocrystals," *Inorganic Chemistry*, vol. 41, pp. 5249–5254, oct 2002.

[3] N. Sahu, N. Brahme, and R. Sharma, "Effect of capping agent on the particle size of CdSe nanoparticles," *Luminescence*, vol. 31, pp. 1400–1406, nov 2016.

[4] F. Abbas, T. Jan, J. Iqbal, I. Ahmad, M. S. H. Naqvi, and M. Malik, "Facile synthesis of ferromagnetic Ni doped CeO2 nanoparticles with enhanced anticancer activity," *Applied Surface Science*, vol. 357, pp. 931–936, 2015.

[5] J. Singh, J. Im, J. E. Whitten, J. W. Soares, and D. M. Steeves, "Chemisorption of a thiol-functionalized ruthenium dye on zinc oxide nanoparticles: Implications for dye-sensitized solar cells," *Chemical Physics Letters*, vol. 497, no. 4-6, pp. 196–199, 2010.

[6] A. H. Davis, E. Hofman, K. Chen, Z. J. Li, A. Khammang, H. Zamani, J. M. Franck, M. M. Maye, R. W. Meulenberg, and W. Zheng, "Exciton Energy Shifts and Tunable Dopant Emission in Manganese-Doped Two-Dimensional CdS/ZnS Core/Shell Nanoplatelets," *Chemistry of Materials*, vol. 31, no. 7, pp. 2516–2523, 2019.

[7] T. Andelman, Y. Gong, M. Polking, M. Yin, I. Kuskovsky, G. Neumark, and S. O 'brien, "Morphological Control and Photoluminescence of Zinc Oxide Nanocrystals,"

[8] Z. A. Peng and X. Peng, "Mechanisms of the shape evolution of CdSe nanocrystals," *Journal of the American Chemical Society*, vol. 123, no. 7, pp. 1389–1395, 2001.

[9] X. Peng, L. Manna, W. Yang, J. Wickham, E. Scher, A. Kadavanich, and A. P. Alivisatos, "Shape control of {CdSe} nanocrystals," *Nature*, vol. 404, no. 6773, pp. 59–61, 2000.

[10] M. L. Kahn, M. Monge, V. Collière, F. Senocq, A. Maisonnat, and B. Chaudret, "Size- and shape-control of crystalline zinc oxide nanoparticles: A new organometallic synthetic method," *Advanced Functional Materials*, vol. 15, no. 3, pp. 458–468, 2005.

[11] L. Manna, E. C. Scher, and A. P. Alivisatos, "Synthesis of soluble and processable rod-, arrow-, teardrop-, and tetrapod-shaped CdSe nanocrystals," *Journal of the American Chemical Society*, vol. 122, no. 51, pp. 12700–12706, 2000.

[12] J. Gao and B. Xu, "Applications of nanomaterials inside cells," *Nano Today*, vol. 4, no. 1, pp. 37–51, 2009.

[13] M. L. Landry, T. E. Morrell, T. K. Karagounis, C. H. Hsia, and C. Y. Wang, "Simple syntheses of CdSe quantum dots," *Journal of Chemical Education*, vol. 91, no. 2, pp. 274–279, 2014.

[14] A. Sundaresan, R. Bhargavi, N. Rangarajan, U. Siddesh, and C. N. R. Rao, "Ferromagnetism as a universal feature of nanoparticles of the otherwise nonmagnetic oxides," *Physical Review B - Condensed Matter and Materials Physics*, vol. 74, no. 16, pp. 1–4, 2006.

[15] Y. Q. Chang, D. B. Wang, X. H. Luo, X. Y. Xu, X. H. Chen, L. Li, C. P. Chen, R. M. Wang, J. Xu, and D. P. Yu, "Synthesis, optical, and magnetic properties of diluted magnetic semiconductor Zn1-xMnxO nanowires via vapor phase growth," *Applied Physics Letters*, vol. 83, no. 19, pp. 4020–4022, 2003.

[16] P. I. Archer, S. A. Santangelo, and D. R. Gamelin, "Direct observation of sp-d exchange interactions in colloidal Mn 2+ - And Co2+ -doped CdSe quantum dots," *Nano Letters*, vol. 7, no. 4, pp. 1037–1043, 2007.

[17] R. Beaulac, P. I. Archer, X. Liu, S. Lee, G. M. Salley, M. Dobrowolska, J. K. Furdyna, and D. R. Gamelin, "Spin-Polarizable Excitonic Luminescence in Colloidal Mn 2+ -Doped CdSe Quantum Dots," *Nano Letters*, vol. 8, no. 4, pp. 1197–1201, 2008.

[18] D. Gao, Z. Zhang, Y. Li, B. Xia, S. Shi, D. Xue, H. Y. Hwang, L. Li, Z. Salman, N. Pavlenko, S. Baneriee, J. S. Lee, B. Kalisky, C. He, J. Garcia-Barriocanal, V. F. J. Manuel, M. Gibert, M. Bibes, J. E. Villegas, A. Barthelemy, J. Mannhart, D. G. Schlom, F. T. Nerio, M. A. Garcia, G. Kopnov, M. A. Garcia, G. Z. Xing, D. Q. Gao, S. B. Singh, D. Q. Gao, J. X. Zhu, A. Durán, T. S. Herng, and Z. X. Guo, "Abnormal room temperature ferromagnetism in CuO–ZnO heterostructures: interface related or not?," *Chem. Commun.*, vol. 51, no. 6, pp. 1151–1153, 2015.

[19] S. Das, S. Banerjee, and T. P. Sinha, "Magnetic study of Fe-doped CdSe nanomaterials," vol. 020105, p. 020105, 2016.

[20] V. A. L. Roy, A. B. Djuri, H. Liu, X. X. Zhang, Y. H. Leung, M. H. Xie, J. Gao, H. F. Lui, and C. Surya, "Magnetic properties of Mn doped ZnO tetrapod structures," *Applied Physics Letters*, vol. 84, no. 5, pp. 756–758, 2004.

[21] Q. A. Pankhurst, J. Connolly, S. K. Jones, J. Dobson,, "Applications of magnetic nanoparticles in biomedicine," *Journal of Physics D: Applied Physics*, vol. 167, no. 36, pp. R167–R181, 2003.

[22] Y.-B. Lu, Z. Ling, W.-Y. Cong, P. Zhang, and Y. Dai, "Carbon induced magnetism of SnO2 surfaces," *Journal of Magnetism and Magnetic Materials*, vol. 394, pp. 280–286, 2015.

[23] R. Murugan, G. Vijayaprasath, T. Mahalingam, and G. Ravi, "Room temperature ferromagnetism of Ni doped cerium oxide single crystalline thin Films deposited by using rf magnetron sputtering," *Materials Letters*, vol. 162, pp. 71–74, 2016.

[24] B. Panigrahy, M. Aslam, D. S. Misra, M. Ghosh, and D. Bahadur, "Defect-related emissions and magnetization properties of ZnO Nanorods," *Advanced Functional Materials*, vol. 20, no. 7, pp. 1161–1165, 2010.

[25] M. A. Boles, D. Ling, T. Hyeon, and D. V. Talapin, "Erratum: The surface science of nanocrystals.," *Nature materials*, vol. 15, no. 3, p. 364, 2016.

[26] N. Kameyama, M. Suda, and Y. Einaga, "Optical tuning of molecule-induced magnetism at non-magnetic semiconductor nanoparticles," *Physica Status Solidi (A) Applications and Materials Science*, vol. 206, no. 12, pp. 2851–2856, 2009.

[27] E. Hao, H. Sun, Z. Zhou, and J. Liu, "Synthesis and optical properties of CdSe and CdSe/CdS nanoparticles," *Chemistry of ...*, no. 9, pp. 3096–3102, 1999.

[28] D. Snigurenko, R. Jakiela, E. Guziewicz, E. Przezdziecka, M. Stachowicz, K. Kopalko, A. Barcz, W. Lisowski, J. W. Sobczak, M. Krawczyk, and A. Jablonski, "XPS study of arsenic doped ZnO grown by Atomic Layer Deposition," *Journal of Alloys and Compounds*, vol. 582, pp. 594–597, 2014.

[29] M. Coey, K. Ackland, M. Venkatesan, and S. Sen, "Collective magnetic response of CeO2 nanoparticles," *Nature Physics*, vol. 12, no. 7, pp. 694–699, 2016.

[30] N. Kirkwood, J. O. V. Monchen, R. W. Crisp, G. Grimaldi, H. A. C. Bergstein, I. du Fosse, W. van der Stam, I. Infante, and A. J. Houtepen, "Finding and fixing traps in ii–vi and iii–v colloidal quantum dots: The importance of z-type ligand passivation," *Journal of the American Chemical Society*, vol. 140, no. 46, pp. 15712–15723, 2018.

[31] W. C. Chan, D. J. Maxwell, X. Gao, R. E. Bailey, M. Han, and S. Nie, "Luminescent quantum dots for multiplexed biological detection and imaging," 2002.

[32] C. Bullen and P. Mulvaney, "The effects of chemisorption on the luminescence of CdSe quantum dots," *Langmuir*, vol. 22, no. 7, pp. 3007–3013, 2006.

[33] Q. Yang, K. Tang, C. Wang, Y. Qian, and S. Zhang, "PVA-Assisted Synthesis and Characterization of CdSe and CdTe Nanowires," *The Journal of Physical Chemistry B*, vol. 106, pp. 9227–9230, sep 2002.

[34] P. Schapotschnikow, B. Hommersom, and T. J. H. Vlugt, "Adsorption and Binding of Ligands to CdSe Nanocrystals," pp. 12690–12698, 2009.

[35] T. Morris and T. Zubkov, "Steric effects of carboxylic capping ligands on the growth of the CdSe quantum dots," *Colloids and Surfaces A: Physicochemical and Engineering Aspects*, vol. 443, pp. 439–449, 2014.

[36] R. A. Sperling and W. J. Parak, "Surface modification, functionalization and bioconjugation of colloidal Inorganic nanoparticles," *Philosophical Transactions of the Royal Society A: Mathematical, Physical and Engineering Sciences*, vol. 368, no. 1915, pp. 1333–1383, 2010.

[37] D. A. Hines, M. A. Becker, and P. V. Kamat, "Photoinduced surface oxidation and its effect on the exciton dynamics of CdSe quantum dots," *Journal of Physical Chemistry C*, vol. 116, no. 24, pp. 13452–13457, 2012.

[38] L. Biadala, E. V. Shornikova, A. V. Rodina, D. R. Yakovlev, B. Siebers, T. Aubert, M. Nasilowski, Z. Hens, B. Dubertret, A. L. Efros, and M. Bayer, "Magnetic polaron on dangling-bond spins in CdSe colloidal nanocrystals," *Nature Nanotechnology*, vol. 12, no. 6, pp. 569–574, 2017.

[39] J. Coey, *Magnetism and magnetic materials*, vol. 12. 2010.

[40] D. Gao, G. Yang, J. Li, J. Zhang, J. Zhang, and D. Xue, "Room-temperature ferromagnetism of flowerlike CuO nanostructures," *Journal of Physical Chemistry C*, vol. 114, no. 43, pp. 18347–18351, 2010.

[41] X. Hou, H. Liu, H. Sun, L. Liu, and X. Jia, "Significant room-temperature ferromagnetism in porous ZnO films: The role of oxygen vacancies," *Materials Science and Engineering: B*, vol. 200, pp. 22–27, oct 2015.

[42] A. Rodina and A. L. Efros, "Magnetic Properties of Nonmagnetic Nanostructures: Dangling Bond Magnetic Polaron in CdSe Nanocrystals," *Nano Letters*, vol. 15, no. 6, pp. 4214–4222, 2015.

[43] S. B. Singh, Y.-F. Wang, Y.-C. Shao, H.-Y. Lai, S.-H. Hsieh, M. V. Limaye, C.-H. Chuang, H.-C. Hsueh, H. Wang, J.-W. Chiou, H.-M. Tsai, C.-W. Pao, C.-H. Chen, H.-J. Lin, J.-F. Lee, C.-T. Wu, J.-J. Wu, W.-F. Pong, T. Ohigashi, N. Kosugi, J. Wang, J. Zhou, T. Regier, and T.-K. Sham, "Observation of the origin of d0 magnetism in ZnO nanostructures using X-ray-based microscopic and spectroscopic techniques.," *Nanoscale*, vol. 6, no. 15, pp. 9166–76, 2014.

[44] B. Qi, S. Ólafsson, and H. P. Gíslason, "Vacancy defect-induced d0 ferromagnetism in undoped ZnO nanostructures: Controversial origin and challenges," *Progress in Materials Science*, vol. 90, pp. 45–74, 2017.

[45] Z. Zhang, U. Schwingenschlögl, and I. S. Roqan, "Possible mechanism for d0 ferromagnetism mediated by intrinsic defects," *RSC Advances*, vol. 4, no. 92, pp. 50759–50764, 2014.

[46] J. M. Coey, P. Stamenov, R. D. Gunning, M. Venkatesan, and K. Paul, "Ferromagnetism in defect-ridden oxides and related materials," *New Journal of Physics*, vol. 12, 2010.

[47] S. Kumar, S. Kumar, N. K. Verma, and S. K. Chakravarti, "Room temperature ferromagnetism in solvothermally synthesized pure CdSe and CdSe:Ni nanorods," *Journal of Materials Science: Materials in Electronics*, vol. 22, no. 9, pp. 1456–1459, 2011.

[48] D. Y. Inamdar, A. D. Lad, A. K. Pathak, I. Dubenko, N. Ali, and S. Mahamuni, "Ferromagnetism in ZnO nanocrystals: Doping and surface chemistry," *Journal of Physical Chemistry C*, vol. 114, no. 3, pp. 1451–1459, 2010.

[49] G. Jayalakshmi and T. Balasubramanian, "Enhancing mechanism for room temperature ferromagnetism in ZnO films on amine functionalization," *Journal of Materials Science: Materials in Electronics*, vol. 24, no. 8, pp. 2928–2933, 2013.

[50] M. D. Regulacio, S. Kar, E. Zuniga, G. Wang, N. R. Dollahon, G. T. Yee, and S. L. Stoll, "Size-Dependent Magnetism of EuS Nanoparticles," *Chemistry of Materials*, vol. 20, pp. 3368–3376, may 2008.

[51] R. Krithiga, S. Sankar, and V. Arunkumar, "F-Center-Mediated Ferromagnetic Ordering in K-Doped ZnO," *Journal of Superconductivity and Novel Magnetism*, vol. 29, no. 1, pp. 245–251, 2016.

[52] X. Xu, C. Xu, J. Dai, J. Hu, F. Li, and S. Zhang, "Size dependence of defect-induced room temperature ferromagnetism in undoped ZnO nanoparticles," *Journal of Physical Chemistry C*, vol. 116, no. 15, pp. 8813–8818, 2012.

[53] A. A. El-Gendy, M. Qian, Z. J. Huba, S. N. Khanna, and E. E. Carpenter, "Enhanced magnetic anisotropy in cobalt-carbide nanoparticles," *Applied Physics Letters*, vol. 104, p. 023111, jan 2014.

[54] M. A. Garcia, J. M. Merino, E. F. Pinel, A. Quesada, J. De La Venta, M. L. González, G. R. Castro, P. Crespo, J. Llopis, J. M. González-Calbet, and A. Hernando, "Magnetic properties of ZnO nanoparticles," *Nano Letters*, vol. 7, no. 6, pp. 1489–1494, 2007.

[55] R. W. Meulenberg, J. R. Lee, S. K. McCall, K. M. Hanif, D. Haskel, J. C. Lang, L. J. Terminello, and T. Van Buuren, "Evidence for ligand-induced paramagnetism in CdSe quantum dots," *Journal of the American Chemical Society*, vol. 131, no. 20, pp. 6888–6889, 2009.

[56] X. G. Zhao, J. H. Chu, and Z. Tang, "Magnetic Properties, Heisenberg Exchange Interaction, and Curie Temperature of CdS Nanoclusters," *Journal of Physical Chemistry C*, vol. 119, no. 52, pp. 29071–29075, 2015.

[57] B. Shakeri and R. W. Meulenberg, "A Closer Look into the Traditional Purification Process of CdSe Semiconductor Quantum Dots," *Langmuir*, vol. 31, no. 49, pp. 13433–13440, 2015.

[58] D. H. Webber and R. L. Brutchey, "Ligand exchange on colloidal CdSe nanocrystals using thermally labile tert -butylthiol for improved photocurrent in nanocrystal films," *Journal of the American Chemical Society*, vol. 134, no. 2, pp. 1085–1092, 2012.

[59] W. W. Yu, L. Qu, W. Guo, and X. Peng, "Experimental determination of the extinction coefficient of CdTe, CdSe, and CdS nanocrystals," *Chemistry of Materials*, vol. 15, no. 14, pp. 2854–2860, 2003.

[60] J. T. Siy, E. M. Brauser, and M. H. Bartl, "Low-temperature synthesis of CdSe nanocrystal quantum dots," *Chemical Communications*, vol. 47, no. 1, pp. 364–366, 2011.

[61] C. K. Brozek, K. H. Hartstein, and D. R. Gamelin, "Potentiometric Titrations for Measuring the Capacitance of Colloidal Photodoped ZnO Nanocrystals," *Journal of the American Chemical Society*, vol. 138, no. 33, pp. 10605–10610, 2016.

[62] M. Yin, Y. Gu, I. L. Kuskovsky, T. Andelman, Y. Zhu, G. F. Neumark, and S. O'Brien, "Zinc oxide quantum rods," *Journal of the American Chemical Society*, 2004.

[63] A. J. Morris-Cohen, M. D. Donakowski, K. E. Knowles, and E. A. Weiss, "The effect of a common purification procedure on the chemical composition of the surfaces of cdse quantum dots synthesized with trioctylphosphine oxide," *Journal of Physical Chemistry C*, vol. 114, no. 2, pp. 897–906, 2010.

[64] S. Choubey, A. Kaushik, and K. Tiwary, "Structural and optical properties of pure and Mg doped CdSe nanoparticles synthesised by microwave assisted method," *Chalcogenide Letters*, vol. 15, no. 3, pp. 125–131, 2018.

[65] S. Gates Rector and T. Blanton, "The powder diffraction file: a quality materials characterization database," *Powder Diffraction*, vol. 34, p. 352–360, 2019.

[66] A. P. Alivisatos, "Perspectives on the physical chemistry of semiconductor nanocrystals," *Journal of Physical Chemistry*, vol. 100, no. 31, pp. 13226–13239, 1996.

[67] D. Briggs, "X-ray photoelectron spectroscopy (XPS)," *Handbook of Adhesion: Second Edition*, pp. 621–622, 2005.

[68] L. Liu, Q. Peng, and Y. Li, "An Effective Oxidation Route to Blue Emission CdSe Quantum Dots," vol. 47, no. 8, pp. 3182–3187, 2008.

[69] J. E. B. Katari, V. L. Colvin, and A. P. Alivisatos, "X-ray photoelectron spectroscopy of cdse nanocrystals with applications to studies of the nanocrystal surface," *The Journal of Physical Chemistry*, vol. 98, no. 15, pp. 4109–4117, 1994.

[70] E. Busby, N. C. Anderson, J. S. Owen, and M. Y. Sfeir, "Effect of Surface Stoichiometry on Blinking and Hole Trapping Dynamics in CdSe Nanocrystals," *Journal of Physical Chemistry C*, vol. 119, no. 49, pp. 27797–27803, 2015.

[71] A. Dutta, R. Bera, A. Ghosh, and A. Patra, "Ultrafast Carrier Dynamics of Photo-Induced Cu-Doped CdSe Nanocrystals," *Journal of Physical Chemistry C*, vol. 122, no. 29, pp. 16992–17000, 2018.

[72] E. M. Boatman, G. C. Lisensky, and K. J. Nordell, "A safer, easier, faster synthesis for CdSe quantum dot nanocrystals," *Journal of Chemical Education*, vol. 82, no. 11, pp. 1697–1699, 2005.

[73] V. Proshchenko, S. Horoz, J. Tang, and Y. Dahnovsky, "Room temperature d0 ferromagnetism in ZnS nanocrystals," *Journal of Applied Physics*, vol. 119, no. 22, p. 223901, 2016.

[74] C. B. Murray, D. Norris, and M. G. Bawendi, "Synthesis and characterization of nearly monodisperse CdE (E= S, Se, Te) semiconductor nanocrystallites," *Journal of the American Chemical Society*, vol. 115, no. 4, pp. 8706–8715, 1993.

[75] H. M. Xiong, "ZnO nanoparticles applied to bioimaging and drug delivery," *Advanced Materials*, vol. 25, no. 37, pp. 5329–5335, 2013.

[76] N. T. Thanh and L. A. Green, "Functionalisation of nanoparticles for biomedical applications," *Nano Today*, vol. 5, no. 3, pp. 213–230, 2010.

[77] V. K. Verma, Y. Singh, R. N. Chauhan, R. S. Anand, and J. Kumar, "Characterization of CdSe nanocrystals for hybrid solar cells," *Integrated Ferroelectrics*, vol. 120, no. 1, pp. 1–5, 2010.

[78] M. L. Green, "A new approach to the formal classification of covalent compounds of the elements," *Journal of Organometallic Chemistry*, vol. 500, no. 1-2, pp. 127–148, 1995.

[79] A. J. Houtepen, Z. Hens, J. S. Owen, and I. Infante, "On the Origin of Surface Traps in Colloidal II-VI Semiconductor Nanocrystals," *Chemistry of Materials*, vol. 29, no. 2, pp. 752–761, 2017.

[80] C. Giansante and I. Infante, "Surface Traps in Colloidal Quantum Dots: A Combined Experimental and Theoretical Perspective," *The Journal of Physical Chemistry Letters*, pp. 5209–5215, 2017.

[81] C. Kittel, *Introduction to Solid State Physics*. New Jersey: John Wiley & Sons, Inc, 8 ed., 2005.

[82] J. E. B. Katari, V. L. Colvin, and A. P. Alivisatos, "X-ray photoelectron spectroscopy of cdse nanocrystals with applications to studies of the nanocrystal surface," *The Journal of Physical Chemistry*, vol. 98, no. 15, pp. 4109–4117, 1994.

[83] S. Neeleshwar, C. L. Chen, C. B. Tsai, Y. Y. Chen, C. C. Chen, S. G. Shyu, and M. S. Seehra, "Size-dependent properties of CdSe quantum dots," *Physical Review B - Condensed Matter and Materials Physics*, vol. 71, no. 20, pp. 6–9, 2005.

[84] D. Jiles and D. Jiles, "Magnetization and Magnetic Moment," *Introduction to Magnetism and Magnetic Materials*, pp. 27–45, 1991.

[85] A. Saha, M. Makkar, A. Shetty, K. Gahlot, A. R. Pavan, and R. Viswanatha, "Diffusion doping in quantum dots: Bond strength and diffusivity," *Nanoscale*, vol. 9, no. 8, pp. 2806–2813, 2017.

[86] M. V. Limaye, S. B. Singh, R. Das, P. Poddar, and S. K. Kulkarni, "Room temperature ferromagnetism in undoped and Fe doped ZnO nanorods: Microwave-assisted synthesis," *Journal of Solid State Chemistry*, vol. 184, no. 2, pp. 391–400, 2011.

[87] S. Deka, A. Falqui, G. Bertoni, C. Sangregorio, G. Poneti, G. Morello, M. De Giorgi, C. Giannini, R. Cingolani, L. Manna, and P. D. Cozzoli, "Fluorescent asymmetrically cobalt-tipped CdSe@CdS core@shell nanorod heterostructures exhibiting room-temperature ferromagnetic behavior," *Journal of the American Chemical Society*, vol. 131, no. 35, pp. 12817–12828, 2009.

[88] A. B. Djurišić and Y. H. Leung, "Optical properties of ZnO nanostructures," *Small*, vol. 2, no. 8-9, pp. 944–961, 2006.

[89] M. Willander, O. Nur, Z. Q. X., Y. L. L., M. Lorenz, B. Q. Cao, J. Z. Pérez, C. Czekalla, G. Zimmermann, M. Grundmann, A. Bakin, A. Behrends, M. Al-Suleiman, A. El-Shaer, A. C. Mofor, B. Postels, A. Waag, N. Boukos, A. Travlos, H. S. Kwack, J. Guinard, and D. D. L., "Zinc oxide nanorod based photonic devices: recent progress in growth, light emitting diodes and lasers," *Nanotechnology*, vol. 20, pp. 1–40, 07 2009.

[90] X. Liu and M. T. Swihart, "A general single-pot heating method for morphology, size and luminescence-controllable synthesis of colloidal ZnO nanocrystals," *Nanoscale*, vol. 5, no. 17, pp. 8029–8036, 2013.

[91] E. Petryayeva, W. R. Algar, and I. L. Medintz, "Quantum dots in bioanalysis: A review of applications across various platforms for fluorescence spectroscopy and imaging," *Applied Spectroscopy*, vol. 67, no. 3, pp. 215–252, 2013.

[92] F. Muhammad, M. Guo, Y. Guo, W. Qi, F. Qu, F. Sun, H. Zhao, and G. Zhu, "Acid degradable ZnO quantum dots as a platform for targeted delivery of an anticancer drug," *Journal of Materials Chemistry*, vol. 21, no. 35, pp. 13406–13412, 2011.

[93] M. Y. Ge, H. P. Wu, L. Niu, J. F. Liu, S. Y. Chen, P. Y. Shen, Y. W. Zeng, Y. W. Wang, G. Q. Zhang, and J. Z. Jiang, "Nanostructured ZnO: From monodisperse nanoparticles to nanorods," *Journal of Crystal Growth*, vol. 305, no. 1, pp. 162–166, 2007.

[94] D. A. Schwartz, N. S. Norberg, Q. P. Nguyen, J. M. Parker, and D. R. Gamelin, "Magnetic Quantum Dots: Synthesis, Spectroscopy, and Magnetism of Co2+- and Ni2+-Doped ZnO Nanocrystals," *Journal of the American Chemical Society*, vol. 125, no. 43, pp. 13205–13218, 2003.

[95] X. G. Zhao and Z. Tang, "Magnetic properties of ZnO nanoclusters," *Journal of Applied Physics*, vol. 111, no. 8, 2012.

[96] D. Sun, M. Wong, L. Sun, Y. Li, N. Miyatake, and H. J. Sue, "Purification and stabilization of colloidal ZnO nanoparticles in methanol," *Journal of Sol-Gel Science and Technology*, vol. 43, no. 2, pp. 237–243, 2007.

[97] E. M. Wong, P. G. Hoertz, C. J. Liang, B. M. Shi, G. J. Meyer, and P. C. Searson, "Influence of organic capping ligands on the growth kinetics of ZnO nanoparticles," *Langmuir*, vol. 17, no. 26, pp. 8362–8367, 2001.

[98] L. E. Greene, B. D. Yuhas, M. Law, D. Zitoun, and P. Yang, "Solution-grown zinc oxide nanowires," *Inorganic Chemistry*, vol. 45, no. 19, pp. 7535–7543, 2006.

[99] X. Wang, J. Shi, Z. Feng, M. Li, and C. Li, "Visible emission characteristics from different defects of ZnS nanocrystals," *Physical Chemistry Chemical Physics*, vol. 13, no. 10, pp. 4715–4723, 2011.

[100] M. Claros, M. Setka, Y. P. Jimenez, and S. Vallejos, "Aacvd synthesis and characterization of iron and copper oxides modified zno structured films," *Nanomaterials*, vol. 10, no. 3, pp. 1–16, 2020.

[101] I. G. Morozov, O. V. Belousova, D. Ortega, M. K. Mafina, and M. V. Kuznetcov, "Structural, optical, XPS and magnetic properties of Zn particles capped by ZnO nanoparticles," *Journal of Alloys and Compounds*, vol. 633, pp. 237–245, 2015.

[102] A. Kathalingam and J. K. Rhee, "Hysteretic I-V nature of ethanol adsorbed ZnO nanorods," *Materials Letters*, vol. 106, pp. 122–124, 2013.

[103] L. G. Verga, A. E. Russell, and C. K. Skylaris, "Ethanol, O, and CO adsorption on Pt nanoparticles: Effects of nanoparticle size and graphene support," *Physical Chemistry Chemical Physics*, vol. 20, no. 40, pp. 25918–25930, 2018.

[104] J. Mooney, M. M. Krause, J. I. Saari, and P. Kambhampati, "A microscopic picture of surface charge trapping in semiconductor nanocrystals," *Journal of Chemical Physics*, vol. 138, no. 20, 2013.

[105] F. Wang, Y. Wang, Y. H. Liu, P. J. Morrison, R. A. Loomis, and W. E. Buhro, "Two-dimensional semiconductor nanocrystals: Properties, templated formation, and magic-size nanocluster intermediates," *Accounts of Chemical Research*, vol. 48, no. 1, pp. 13–21, 2015.

[106] A. Brumberg, S. M. Harvey, J. P. Philbin, B. T. Diroll, B. Lee, S. A. Crooker, M. R. Wasielewski, E. Rabani, and R. D. Schaller, " Determination of the In-Plane Exciton Radius in 2D CdSe Nanoplatelets via Magneto-optical Spectroscopy ," *ACS Nano*, vol. 13, no. 8, pp. 8589–8596, 2019.

[107] P. Xiao, J. Huang, D. Yan, D. Luo, J. Yuan, B. Liu, and D. Liang, "Emergence of nanoplatelet light-emitting diodes," *Materials*, vol. 11, no. 8, pp. 1–22, 2018.

[108] L. T. Kunneman, J. M. Schins, S. Pedetti, H. Heuclin, F. C. Grozema, A. J. Houtepen, B. Dubertret, and L. D. Siebbeles, "Nature and decay pathways of photoexcited states in CdSe and CdSe/CdS nanoplatelets," *Nano Letters*, vol. 14, no. 12, pp. 7039–7045, 2014.

[109] B. T. Diroll, W. Cho, I. Coropceanu, S. M. Harvey, A. Brumberg, N. Holtgrewe, S. A. Crooker, M. R. Wasielewski, V. B. Prakapenka, D. V. Talapin, and R. D. Schaller, "Semiconductor Nanoplatelet Excimers," *Nano Letters*, vol. 18, no. 11, pp. 6948–6953, 2018.

[110] B. P. Rakgalakane and M. J. Moloto, "Aqueous Synthesis and Characterization of CdSe/ZnO Core-Shell Nanoparticles," *Journal of Nanomaterials*, vol. 2011, pp. 1–6, 2011.

[111] C. Madhu, A. Sundaresan, and C. N. Rao, "Room-temperature ferromagnetism in undoped GaN and CdS semiconductor nanoparticles," *Physical Review B - Condensed Matter and Materials Physics*, vol. 77, no. 20, pp. 3–6, 2008.

[112] A. Shan, W. Liu, R. Wang, and C. Chen, "Magnetism in undoped ZnS nanotetrapods," *Physical Chemistry Chemical Physics*, vol. 15, no. 7, pp. 2405–2410, 2013.

[113] W. Z. Xiao, L. L. Wang, Q. Y. Rong, G. Xiao, and B. Meng, "Magnetism in undoped ZnS studied from density functional theory," *Journal of Applied Physics*, vol. 115, no. 21, 2014.

[114] S. Banerjee, K. Rajendran, N. Gayathri, M. Sardar, S. Senthilkumar, and V. Sengodan, "Change in the room temperature magnetic property of ZnO upon Mn doping," *Journal of Applied Physics*, vol. 104, no. 4, 2008.

[115] Y. Zhang, F. Han, Q. Dai, and J. Tang, "Magnetic properties and photovoltaic applications of ZnO:Mn nanocrystals," *Journal of Colloid and Interface Science*, vol. 517, pp. 194–203, 2018.

[116] A. P. Alivisatos, "Perspectives on the physical chemistry of semiconductor nanocrystals," *Journal of Physical Chemistry*, vol. 100, no. 31, pp. 13226–13239, 1996.

[117] N. Ashcroft and N. Mermin, *Solid State Physics*. Cengage Learning, 2011.

[118] P. Van der Heide, *X-ray photoelectron spectroscopy: an introduction to principles and practices*. John Wiley & Sons, 2011.

Appendices

CHAPTER A
X-RAY DIFFRACTION AND PHOTOELECTRON SPECTROSCOPY

A.0.1 XRD and XPS

X-ray characterization techniques such as x-ray diffraction (XRD) and x-ray photoelectron spectroscopy (XPS) are both excellent tools to help identify crystallographic and elemental information respectively. Described in this section is a brief overview of these x-ray techniques.

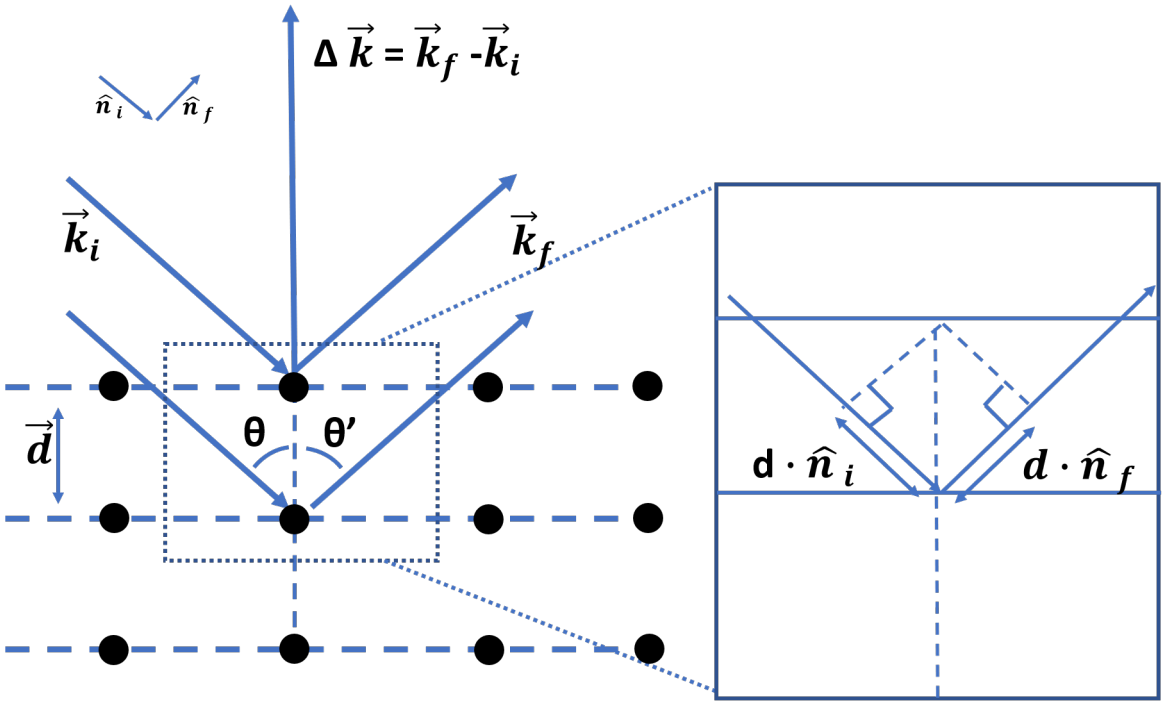

Figure A.1: Diagram of Bragg Diffraction where incident x-rays diffract off crystal planes. Close up illustrates the path difference from two points separated by a distance, $\overrightarrow{d}$.

To begin, XRD can be described as a scattering event, where for example the condition for constructive interference between two scatters [117] is given as ,

$$d \cdot (\hat{n}_i - \hat{n}_f) = m\lambda \tag{A.1}$$

or in terms of the scattered wave vectors multiply equation A.1 multiply equation A.1 by $2\pi/\lambda$ [117] as follows ,

$$d \cdot (\overrightarrow{k_i} - \overrightarrow{k_f}) = 2\pi m \tag{A.2}$$

For an array of scatters at the sites of a Bravais lattice separated by the lattice vector $\overrightarrow{R}$, the scattering condition [117] becomes ,

$$R \cdot (\overrightarrow{k_i} - \overrightarrow{k_f}) = 2\pi m \tag{A.3}$$

The Laue condition for constructive interference occurs if the change in the wave vector, $\Delta k = (k_i - k_f)$ is a vector of the reciprocal lattice. Where the reciprocal lattice can be characterized as a set of wave vectors $\overrightarrow{k}$ satisfying the condition $e^{i\delta \vec{k} \cdot \vec{R}} = 1$.

The X-ray photoelectron spectroscopy experiments were performed using a SPECS hemispherical analyzer with an Al K-α or Mg K-α anode as the excitation source. For CdSe, difficulties can arise when using the Al anode for XPS as it is difficult to distinguish between the Se $3d$ and Se Auger peaks. The Mg-anode alleviates the overlap between the Se Auger and $3d$ peaks by shifting the Auger peaks to lower binding energies. Typical XPS survey scans are performed from binding energies 1300 eV to 0 eV with a pass energy of 100 eV and step size of 0.5 eV. Fine scans on particular elements of interest use a pass energy of 20 eV and a step size of 0.2 eV. Samples were prepared from colloidal solutions by adding the solution dropwise to a Si wafer or a glass slide.

The photo-electrons have kinetic energies given by,

$$KE = hv - BE - \phi \tag{A.4}$$

where hv is the energy of the photon, BE is the binding energy of the photo-electron, and ϕ is the work function of the spectrometer. To gain a more thorough understanding of XPS review the following references [67, 118]

CHAPTER B
GENERAL ERROR PROPAGATION

B.0.1 Error Analysis

The error propagation used for this thesis follows algebra covered by Taylor [69], for products and quotients (i.e. $a \times b \times c$ and $\frac{a}{b \times c}$) have error propagation formula as follows:

$$\delta M = M \times \left[\left(\frac{\delta a}{a} \right)^2 + \left(\frac{\delta b}{b} \right)^2 + \left(\frac{\delta c}{c} \right)^2 + ... \right]^{\frac{1}{2}} \tag{B.1}$$

where M, a, b, and c are measured values and the prefix of δM, δa, δb, δc indicate the error or uncertainty in those values. The isothermal magnetization values were calculated as follows

$$\delta M = M \times \left[\left(\frac{\delta emu}{emu} \right)^2 + \left(\frac{\delta m}{m} \right)^2 \right]^{\frac{1}{2}} \tag{B.2}$$

Typically the factor that contribute the most to uncertanity in the magnetometry experiments is the error in measuring the mass of the sample.

For example, if a sample has a magnetization, $M = 9.17 \times 10^{-6}$ emu/g with initial magnetization of $M = 5.6 \times 10^{-8} \pm 6.8 \times 10^{-9}$ emu with recorded mass $m = 0.010 \pm 0.0003$ g the error propagation expression would proceed as follows,

$$\delta M = (9.2 \times 10^{-6} emu/g) \times \left[\left(\frac{6.8 \times 10^{-9} emu}{5.6 \times 10^{-8} emu} \right)^2 + \left(\frac{0.0003 g}{0.01 g} \right)^2 \right]^{\frac{1}{2}} \tag{B.3}$$

From equation B.3 δ M $= 1.6 \times 10^{-6}$ emu/g.

CHAPTER 7
BIOGRAPHY OF THE AUTHOR

Alex Khammang was born and raised near Richmond, Virginia where he would eventually attend Virginia Commonwealth University (VCU) in 2008. He pursued a B.S. in physics which began his research career performing molecular dynamics simulations on the elastic properties of metallic nanowires. The project spurred his interests in theory to pursue a Master's thesis to understand how twinning planes affect the dislocation propagation through metallic nanowires under the supervision of Dr. Dennis Demchenko.

In 2014, he entered the PhD program at the University of Maine in Orono, where he transitioned from performing theoretical calculations to the experimental investigation of colloidal semiconductor nanocrystals under the guidance of Dr. Robert W. Meulenberg. Throughout the program he developed a wide array of experimental skills including magnetometry, x-ray spectroscopies, x-ray diffraction, UV-vis spectroscopy, wet chemical synthesis, physical vapor deposition, and thermal gravimetic analysis. His first talk was at the Physical Electronics Conference (2018), where he competed for the covenanted Nottingham prize for advancements in surface science. Following this presentation he presented posts at the Gordon Research Society for Colloidal Nanocrystals (2018) and Materials Research Society meeting (2018). The following year he earned a spot give at the MRS fall meeting (2019) to give talk on his work with colloidal nanocrystals

Though not part of his thesis, he split his time balancing multiple projects at Argonne and Berkeley National Laboratories to perform x-ray absorption spectroscopy experiments. The project investigated, for the first time, CdSe Cu cation exchange experiments in the liquid phase using hard x-rays. In conjunction with his university studies he also attended the National Neutron and X-ray Scattering school at both Argonne and Oak Ridge National Laboratories, to help further develop a broader understanding of synchrotron and neutron science. Alex is a candidate for the Doctor of Philosophy degree in Physics from the University of Maine in August 2020.